REALIZING SELECTIVE ELECTROCHEMICAL CO_2 AND N_2 REDUCTION BY INTERFACIAL ENGINEERING AND RATIONAL CATALYST DESIGN

by

Xu Han

A dissertation submitted to Johns Hopkins University in conformity with the requirements for the degree of Doctor of Philosophy

Baltimore, Maryland

October 2020

Abstract

Global demand for renewable energy is growing as the excessive burning of fossil fuels causes severe environmental consequences and crisis of energy shortage. Popular technologies for renewable energy conversion include transformation of solar or wind energy to electricity. Therefore, new requirement has arisen for storage and utilization of the electricity. Electrochemical reduction of CO_2 and N_2 are promising routes for this demand because of the fuels and value-added chemicals generated in the process.

However, due to the inert nature of CO_2 and N_2, current attempts under aqueous conditions result in low activity and selectivity. The poor electrocatalytic performance is mainly attributed to underexposed active sites of catalysts and competing hydrogen evolution reaction (HER). An additional challenge for CO_2 reduction reaction (CO_2RR) on Cu, the only metal with the ability to catalyze formation of hydrocarbon and alcohol, is the selective generation of certain product, especially C_{2-3} molecules.

In order to suppress HER, catalyst morphologies that lead to elevated local pH have been developed. In the first study, we discovered the importance of carbon porosity on Cu-catalyzed CO_2RR using carbon aerogels, a class of high surface area carbon foams with tunable structural properties. Systematically adjusting the porosity of the carbon aerogels leads to significant differences in catalytic selectivity and activity.

Selectivity for C-C coupling products remains a major challenge for CO_2RR. Continuing the study on the effect of carbon in this reaction, we developed a facile method by modifying the Cu foil surface with a layer of porous carbon. Compared to a carbon black modifier, the carbon aerogel one contributes to a major boost of C_{2-3} selectivity. Our findings illustrate that carbon, long-time regarded as an innocent player in catalysis, can have an outsized role in directing product formation.

To tackle the challenges of low yield rate and selectivity with nitrogen reduction reaction (NRR), we presented a catalyst comprised of MoO_2 with highly active surface sites dispersed over conductive carbon nanowires. This uniquely engineered catalyst exhibits exceptional performance under ambient aqueous conditions, which demonstrates rational design of active sites and adequate use of carbon support can overcome challenging obstacles within NRR.

Primary Reader and Advisor: Professor V. Sara Thoi

Secondary Readers: Professor D. Howard Fairbrother

Acknowledgements

First and foremost, I would like to express my gratitude to my advisor, Professor Sara Thoi. Through her guidance in the past five years, I was able to develop the rigorous attitude toward science and enhance critical thinking. I was allowed and encouraged to study the projects that I'm most interested in, during which I had the opportunity to do research and solve problems relatively independently. This experience has shaped me into a better scientist and will have long-lasting impact on my career. I'm very grateful that she also encouraged me to take on opportunities that would benefit me to grow as a person.

I would like to thank Professor Thomas Kempa and Professor Howard Fairbrother for being my committee members, and providing support and advices throughout my graduate study. I also express thankfulness to all my research collaborators, Carter Gerke, Dr. Elisa Miller, Dr. Nick Bedford, Mei Wang, Dr. Taylor Woehl and My Linh Le, who all helped me successfully transform research ideas into impactful results.

I'm thankful for many friends within and outside of the Chemistry Department, who have supported me throughout the journey and enriched my life when not in lab. Thank you all for leaving me great memories through the trips, parties, and other get-togethers.

Finally, I especially thank my mom, dad, Jin, Hao, Jingrui, Lucy (feline) and Shaochen. Their unconditional love has always been the foundation of my fearless exploration.

Contents

List of Tables

List of Figures

List of Schemes

Chapter 1: Introduction to New Catalytic Designs to Solve the Challenges of Electrochemical CO_2 and N_2 Reduction Reaction

1.1 Growing Need for Renewable Energy

There is a growing global demand for renewable energy as the excessive burning of fossil fuels causes severe environmental consequences and crisis of energy shortage.[1] Renewable energy, usually with a carbon-neutral scope, involves harnessing the power of nature like wind and sun as well as developing new technologies to facilize sustainable energy conversion. Popular technologies for renewable energy conversion include transformation of solar or wind energy to electricity. Traditional way to utilize electricity has been focused on developing electricity storage technique, like various generations of batteries. However, safety and toxicity are the issues associated with battery usage in addition to the consumption of natural resources in the production process of batteries.[2,3]

Novel ways of electricity storage and utilization have been a hot topic in recent decades. These methods usually involve further conversion of electricity into other forms of fuels that are easy to store and utilize. One common approach is electricity-powered production of hydrogen, which is a clean fuel with only water and heat as by-products upon combustion.[4] In recent years, electrochemical reduction of CO_2 into CO or hydrocarbons has emerged to be a popular research area.[5] This reaction enables utilization of the excessive and abundant CO_2 as the carbon source for generating carbon-neutral fuels. Nitrogen reduction is also an important process in this regard.[6,7] It facilitates ammonia synthesis which is not only essential to the global agriculture industry but also an energy-rich carbon-free fuel.

1.2 Electrochemical Reduction of CO_2 and Nitrogen

Electrochemical CO_2 reduction reaction (CO_2RR) is the conversion of CO_2 into more reduced chemicals by electrical energy. In recent years, it has been of great research interest as a promising approach for carbon capture and utilization. The process overall is made possible by conducting electrocatalysis with CO_2 feed gas in a H-type cell (**Scheme 1.1**).

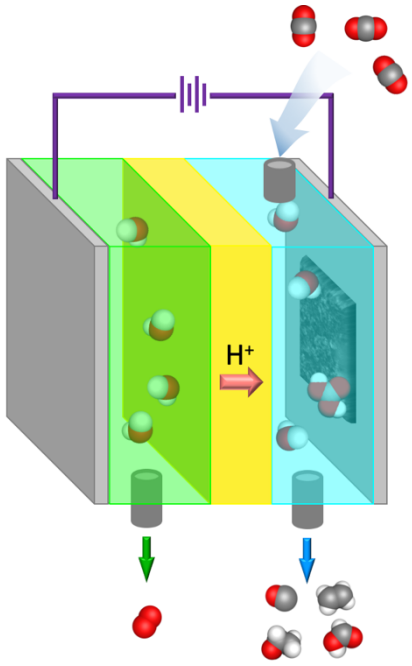

Scheme 1.1. Illustration of CO_2RR conducted in a H-type cell.

Electrocatalysis utilizes the electrode to donate or accept electrons while being a catalyst. It happens at the electrode-electrolyte interface and can be defined as the heterogeneous catalysis of electrochemical reactions.[8] It also happens at much milder conditions than traditional industrial reactions. By using electricity generated from renewable energy, the reaction can be environmentally friendly.

Various transition metal electrocatalysts have been investigated for CO_2RR.[9,10] On a specific metal, the reaction rate is determined by binding strength of the adsorbed species to the metal surface. More specifically, the binding strength needs to be just "right"—too weak adsorption of CO_2 on the surface results in no reactions on the electrocatalyst surface; too strong interaction leads to poisoning the surface as the products fail to dissociate.[9] As for the multi-step reduction nature of CO_2RR, different binding strength of CO_2 and intermediates on metal surfaces also contributes to variations on product selectivity. For example, in aqueous reaction conditions, CO is the favored product on Au, Ag and Zn surface, while HCO_2H is selectively produced on Sn, In and Pb. Cu, however, is the only metal known to convert CO_2 into hydrocarbons and alcohols (**Figure 1.1**).[11,12] Because of the value-added products it is able to produce, Cu has been the center of research for CO_2RR for selectively generating products at an efficient rate.

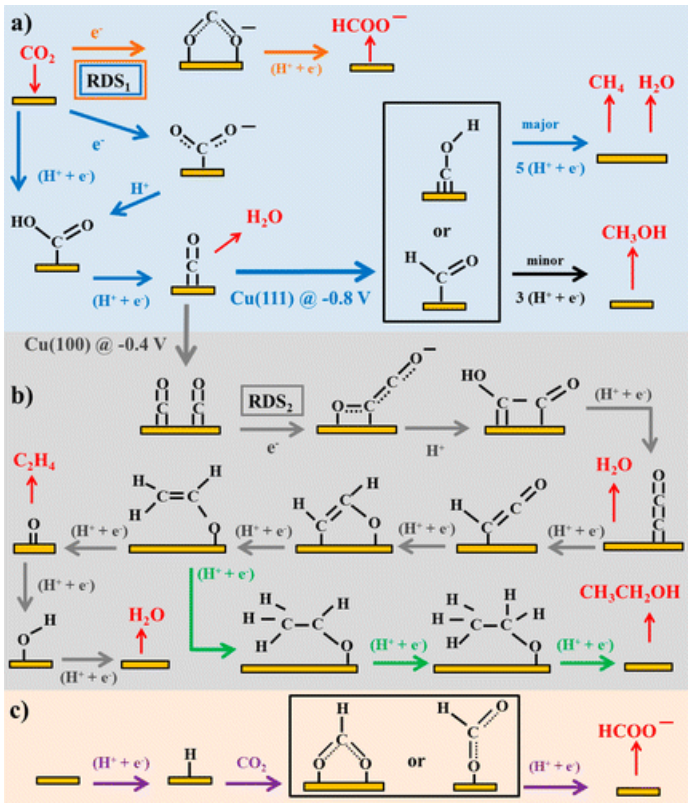

Figure 1.1. Possible reaction pathways for CO_2RR on Cu to produce various products. Reproduced with permission from reference 12. Copyright 2015 ACS Publications.

Similar to CO_2RR, nitrogen reduction reaction (NRR) when powered by sustainable sources of energy is the renewable conversion of nitrogen into ammonia, a highly useful compound that feeds the earth and is widely used in a variety of industries. Ammonia production in industry is dominated by the Haber-Bosch process, where large amount of energy is consumed to maintain the high temperature in addition to the need of fossil fuel products to produce the hydrogen feedstock. During this process, approximately 1.87 tons of carbon dioxide is released for each ton of NH_3.[13] The process operates on such a grand scale that it consumes more than 1% of the global annual energy generation.[14] Thus,

electrochemical NRR is of significant importance as it is conducted under mild conditions with electron as the reducing agent and water as hydrogen source.

The study of electrocatalysts for NRR has been focused on noble metals, Fe-group metals and Mo.[7] Unlike CO_2RR, the electrochemical NRR though occurring from multiple possible pathways generally produces ammonia as the only product (**Figure 1.2**).[15]

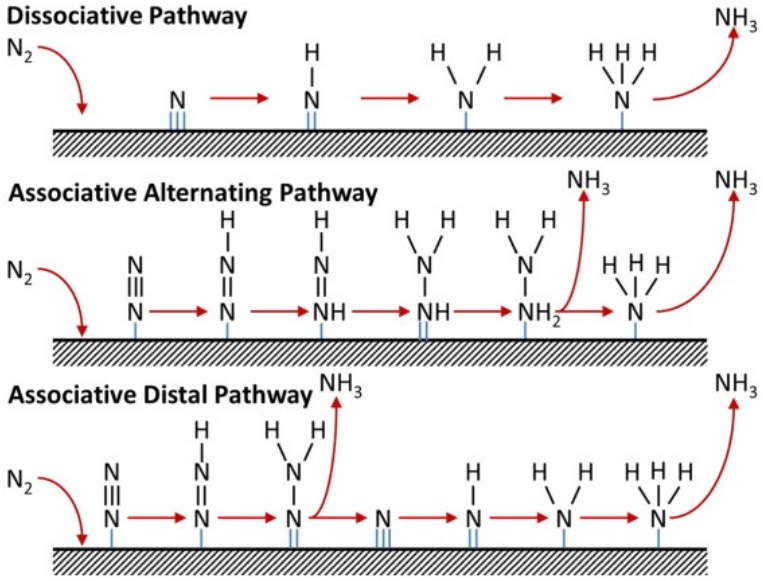

Figure 1.2. Typical mechanisms for NRR on heterogeneous catalysts. Reproduced with permission from reference 14. Copyright 2017 Elsevier.

1.3 Challenges with CO_2RR and NRR

Electrocatalysis focuses on how to mitigate the energy barrier by electrode/catalyst design. Like all the electrocatalytic reaction, the major challenge for CO_2RR and NRR is to develop efficient electrocatalysts to increase the reaction rate. CO_2 and nitrogen are extremely stable molecules. The formation of initial intermediate $CO_2^{\bullet-}$ requires large energy uptake, which is the origin that CO_2RR usually requires high potentials applied to the system.[16] The reduction of nitrogen

to ammonia is a multi-step process that is kinetically and energetically challenging. Current studies focus on how to improve the yield rate of ammonia during NRR.

Other challenges come from the specific system. For example, aqueous system is the most favorable condition due to low cost and environmental friendliness. In this case, hydrogen evolution reaction (HER) as a result of reducing water becomes the major side reaction for both CO_2RR and NRR. It remains a challenge to suppress the HER and promote the CO_2RR and NRR products (**Table 1.1**). Cu is one of the most studied metals for CO_2RR due to its ability to catalyze formation of hydrocarbon and alcohol. The diverse reaction pathways on Cu in the meantime also contribute to the difficulties of product selectivity. In addition, stability issue of catalytic materials during CO_2RR and NRR also poses a challenge on ensuring long-term activity and selectivity.

Table 1.1. Standard potentials (E^0) associated with the electrochemical CO_2RR. Data source: reference 16.

Reaction	E^0 (V vs. RHE)
$CO_2 + 2H^+ + 2e^- \rightarrow CO + H_2O$	–0.106
$CO_2 + 2H^+ + 2e^- \rightarrow HCOOH$	–0.250
$CO_2 + 4H^+ + 4e^- \rightarrow HCHO + H_2O$	–0.070
$CO_2 + 6H^+ + 6e^- \rightarrow CH_3OH + H_2O$	0.016
$CO_2 + 8H^+ + 8e^- \rightarrow CH_4 + 2H_2O$	0.169
$2CO_2 + 12H^+ + 12e^- \rightarrow C_2H_4 + 4H_2O$	0.064
$2H^+ + 2e^- \rightarrow H_2$	0.000

1.4 New Designs for Solving the Challenges

To tackle the high energy barriers and low reaction rate of CO_2RR and NRR, catalyst designs have been focused on exploring and exposing active sites for the reaction. The efforts include developing active metal compounds and controlling electrocatalyst morphology. For example, O impurity in Cu has been proven to enhance the activity towards CO_2RR.[17–19] Nano-structured Cu compounds expose more grain boundaries and high-index surface, which is shown to increase the CO_2RR efficiency.[20–22] As for NRR, several Mo compounds have been reported as promising catalysts.[23–25] Nanostructured catalysts can also improve the catalytic activity.

In order to suppress the parasitic HER, catalysts with morphologies that lead to elevated local pH have been developed. This type of catalyst design has in common a roughened 3-D structure that restricts the diffusion of buffer ions to the reaction site to compensate for the local pH increase due to the catalytic reaction. (**Scheme 1.2**) Some examples include mesoporous Au[26], and nanofoam/nanowire Cu[27,28] for CO_2RR.

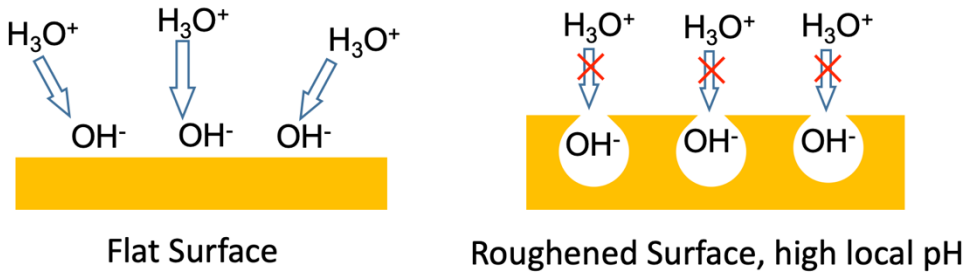

Scheme 1.2. Illustration of the effect of catalyst structure on local pH.

In recent years, a new strategy to enhance the product selectivity by modifying the electrode surface emerges. More specifically, the use of polymers[29], organic compounds[30,31], or surfactants[32] as surface modifiers on Cu surface can suppress HER and promote selectivity of C-C coupling, which benefit the generation of value-added C_{2-3} products.

1.5 Implications for the Thesis Research

Carbon has a long history to be used as catalyst support due to its great conductivity, chemical stability as well as high surface area to bind reaction intermediates. It has been regarded as an inert support with no effect on the catalytic reaction. This note has been challenged recently when Cu supported by different types of carbon was found to have varied activity towards CO_2RR.[33] Moreover, carbon support was also shown to affect the structure evolution of Cu nanoparticles during CO_2RR.[34] The following chapters will discuss the utilization of porous carbon as support and surface modifier for Cu catalyst to tune the selectivity during CO_2RR and carbon nanowire as conductive support for surface defected MoO_2 nanoparticles for NRR. To begin the efforts, carbon aerogels with controlled pore sizes were synthesized and used as support for Cu particles toward CO_2RR. An optimized pore size at 30-50 nm was shown to best suppress HER and promote C_2 products generation (**Chapter 2**). To further probe the effect of porous carbon in a broader scope, direct modification of Cu surface by the carbon aerogel (CA-Cu) was studied with carbon black modified Cu as comparison. Significant enhancement of C_{2-3}—45% Faradaic efficiency at potential of -0.98 V

vs. RHE—was demonstrated on CA-Cu, which was attributed to the dual effect of carbon modifier: as diffusion layer and surface restructuring inducer (**Chapter 3**). NRR was then investigated with highly dispersed surface defected MoO2 nanoparticles supported on carbon nanowires. This material showed unprecedented activity and selectivity to produce ammonia in aqueous solution. Surface defect on the MoO_2 nanoparticles as well as the carbon nanowire support which contributes to the high nanoparticle dispersion was believed to have contributed to the promising catalytic performance (**Chapter 4**).

1.6 Reference

(1) Turner, J. A. A Realizable Renewable Energy Future. *Science* **1999**, *285* (5428), 687-689. https://doi.org/10.1126/science.285.5428.687.

(2) Kwade, A.; Haselrieder, W.; Leithoff, R.; Modlinger, A.; Dietrich, F.; Droeder, K. Current Status and Challenges for Automotive Battery Production Technologies. *Nature Energy* **2018**, *3*, 290-300. https://doi.org/10.1038/s41560-018-0130-3.

(3) Liu, Y.; Zhu, Y.; Cui, Y. Challenges and Opportunities towards Fast-Charging Battery Materials. *Nature Energy*. **2019**, *4*, 540-550. https://doi.org/10.1038/s41560-019-0405-3.

(4) Dubouis, N.; Grimaud, A. The Hydrogen Evolution Reaction: From Material to Interfacial Descriptors. *Chem. Sci.* **2019**, *10*, 9165-9181. https://doi.org/10.1039/c9sc03831k.

(5) Nitopi, S.; Bertheussen, E.; Scott, S. B.; Liu, X.; Engstfeld, A. K.; Horch, S.;

Seger, B.; Stephens, I. E. L.; Chan, K.; Hahn, C.; et al. Progress and Perspectives of Electrochemical CO_2 Reduction on Copper in Aqueous Electrolyte. *Chem. Rev.* **2019**, *119* (12), 7610-7672. https://doi.org/10.1021/acs.chemrev.8b00705.

(6) Cui, X.; Tang, C.; Zhang, Q. A Review of Electrocatalytic Reduction of Dinitrogen to Ammonia under Ambient Conditions. *Adv. Energy Mater.* **2018**, *8* (22), 1–25. https://doi.org/10.1002/aenm.201800369.

(7) Guo, X.; Du, H.; Qu, F.; Li, J. Recent Progress in Electrocatalytic Nitrogen Reduction. *J. Mater. Chem. A*. **2019**, *7*, 3531-3543. https://doi.org/10.1039/c8ta11201k.

(8) Sun, S. G.; Christensen, P. A.; Wieckowski, A. In-Situ Spectroscopic Studies of Adsorption at the Electrode and Electrocatalysis, **2007**, Chapter 3. https://doi.org/10.1016/B978-0-444-51870-5.X5000-3.

(9) Kuhl, K. P.; Hatsukade, T.; Cave, E. R.; Abram, D. N.; Kibsgaard, J.; Jaramillo, T. F. Electrocatalytic Conversion of Carbon Dioxide to Methane and Methanol on Transition Metal Surfaces. *J. Am. Chem. Soc.* **2014**, *136* (40), 14107–14113. https://doi.org/10.1021/ja505791r.

(10) Franco, F.; Rettenmaier, C.; Jeon, H. S.; Roldan Cuenya, B. Transition Metal-Based Catalysts for the Electrochemical CO_2 Reduction: From Atoms and Molecules to Nanostructured Materials . *Chem. Soc. Rev.* **2020**, *49*, 6884-6946. https://doi.org/10.1039/d0cs00835d.

(11) Hori, Y.; Murata, A.; Takahashi, R. Formation of Hydrocarbons in the

Electrochemical Reduction of Carbon Dioxide at a Copper Electrode in Aqueous Solution. *J. Chem. Soc. Faraday Trans. 1 Phys. Chem. Condens. Phases* **1989**, *85*, 2309-2326. https://doi.org/10.1039/F19898502309.

(12) Kortlever, R.; Shen, J.; Schouten, K. J. P.; Calle-Vallejo, F.; Koper, M. T. M. Catalysts and Reaction Pathways for the Electrochemical Reduction of Carbon Dioxide. *J. Phys. Chem. Lett.* **2015**, *6* (20), 4073–4082. https://doi.org/10.1021/acs.jpclett.5b01559.

(13) Appl, M. Ammonia, 2. Production Processes. In *Ullmann's Encyclopedia of Industrial Chemistry*; **2011**. https://doi.org/10.1002/14356007.o02_o11.

(14) Erisman, J. W.; Sutton, M. A.; Galloway, J.; Klimont, Z.; Winiwarter, W. How a Century of Ammonia Synthesis Changed the World. *Nat. Geosci.* **2008**, *1*, 636-639. https://doi.org/10.1038/ngeo325.

(15) Shipman, M. A.; Symes, M. D. Recent Progress towards the Electrosynthesis of Ammonia from Sustainable Resources. *Catal. Today* **2017**, *286*, 57-68. https://doi.org/10.1016/j.cattod.2016.05.008.

(16) Kauffman, D. R.; Thakkar, J.; Siva, R.; Matranga, C.; Ohodnicki, P. R.; Zeng, C.; Jin, R. Efficient Electrochemical CO_2 Conversion Powered by Renewable Energy. *ACS Appl. Mater. Interfaces* **2015**, *7* (28). https://doi.org/10.1021/acsami.5b04393.

(17) Li, C. W.; Kanan, M. W. CO_2 Reduction at Low Overpotential on Cu Electrodes Resulting from the Reduction of Thick Cu 2O Films. *J. Am. Chem. Soc.* **2012**,*134* (17), 7231–7234. https://doi.org/10.1021/ja3010978.

(18) Chou, T. C.; Chang, C. C.; Yu, H. L.; Yu, W. Y.; Dong, C. L.; Velasco-Vélez, J. J.; Chuang, C. H.; Chen, L. C.; Lee, J. F.; Chen, J. M.; et al. Controlling the Oxidation State of the Cu Electrode and Reaction Intermediates for Electrochemical CO_2 Reduction to Ethylene. *J. Am. Chem. Soc.* **2020**, *142* (6), 2857-2867. https://doi.org/10.1021/jacs.9b11126.

(19) Favaro, M.; Xiao, H.; Cheng, T.; Goddard, W. A.; Crumlin, E. J. Subsurface Oxide Plays a Critical Role in CO_2 Activation by Cu(111) Surfaces to Form Chemisorbed CO_2, the First Step in Reduction of CO2. *Proc. Natl. Acad. Sci. U. S. A.* **2017**, *114* (26), 6706-6711. https://doi.org/10.1073/pnas.1701405114.

(20) Kim, J.; Choi, W.; Park, J. W.; Kim, C.; Kim, M.; Song, H. Branched Copper Oxide Nanoparticles Induce Highly Selective Ethylene Production by Electrochemical Carbon Dioxide Reduction. *J. Am. Chem. Soc.* **2019**, *141* (17), 6986-6994. https://doi.org/10.1021/jacs.9b00911.

(21) Reske, R.; Mistry, H.; Behafarid, F.; Roldan Cuenya, B.; Strasser, P. Particle Size Effects in the Catalytic Electroreduction of CO_2 on Cu Nanoparticles. *J. Am. Chem. Soc.* **2014**, *136* (19), 6978–6986. https://doi.org/10.1021/ja500328k.

(22) Chen, Z.; Wang, T.; Liu, B.; Cheng, D.; Hu, C.; Zhang, G.; Zhu, W.; Wang, H.; Zhao, Z. J.; Gong, J. Grain-Boundary-Rich Copper for Efficient Solar-Driven Electrochemical CO_2 Reduction to Ethylene and Ethanol. *J. Am.*

Chem. Soc. **2020**, *142* (15) 6878-6883. https://doi.org/10.1021/jacs.0c00971.

(23) Zhao, J.; Chen, Z. Single Mo Atom Supported on Defective Boron Nitride Monolayer as an Efficient Electrocatalyst for Nitrogen Fixation: A Computational Study. *J. Am. Chem. Soc.* **2017**, *139* (36) 12480-12487. https://doi.org/10.1021/jacs.7b05213.

(24) Liu, Y.; Zhu, X.; Zhang, Q.; Tang, T.; Zhang, Y.; Gu, L.; Li, Y.; Bao, J.; Dai, Z.; Hu, J. S. Engineering Mo/Mo_2C/MoC Hetero-Interfaces for Enhanced Electrocatalytic Nitrogen Reduction. *J. Mater. Chem. A* **2020**, *8*, 8920-8926. https://doi.org/10.1039/d0ta03290e.

(25) Zhang, L.; Ji, X.; Ren, X.; Ma, Y.; Shi, X.; Tian, Z.; Asiri, A. M.; Chen, L.; Tang, B.; Sun, X. Electrochemical Ammonia Synthesis via Nitrogen Reduction Reaction on a MoS_2 Catalyst: Theoretical and Experimental Studies. *Adv. Mater.* **2018**, *30* (28), 2–7. https://doi.org/10.1002/adma.201800191.

(26) Hall, A. S.; Yoon, Y.; Wuttig, A.; Surendranath, Y. Mesostructure-Induced Selectivity in CO_2 Reduction Catalysis. *J. Am. Chem. Soc.* **2015**, *137* (47), 14834–14837. https://doi.org/10.1021/jacs.5b08259.

(27) Sen, S.; Liu, D.; Palmore, G. T. R. Electrochemical Reduction of CO_2 at Copper Nanofoams. *ACS Catal.* **2014**, *4* (9), 3091–3095. https://doi.org/10.1021/cs500522g.

(28) Raciti, D.; Livi, K. J.; Wang, C. Highly Dense Cu Nanowires for Low-

Overpotential CO_2 Reduction. *Nano Lett.* **2015**, *15*, 6829–6835. https://doi.org/10.1021/acs.nanolett.5b03298.

(29) Ahn, S.; Klyukin, K.; Wakeham, R. J.; Rudd, J. A.; Lewis, A. R.; Alexander, S.; Carla, F.; Alexandrov, V.; Andreoli, E. Poly-Amide Modified Copper Foam Electrodes for Enhanced Electrochemical Reduction of Carbon Dioxide. *ACS Catal.* **2018**, *8* (5), 4132–4142. https://doi.org/10.1021/acscatal.7b04347.

(30) Han, Z.; Kortlever, R.; Chen, H. Y.; Peters, J. C.; Agapie, T. CO_2 Reduction Selective for C≥2 Products on Polycrystalline Copper with N-Substituted Pyridinium Additives. *ACS Cent. Sci.* **2017**, *3* (8), 853–859. https://doi.org/10.1021/acscentsci.7b00180.

(31) Xie, M. S.; Xia, B. Y.; Li, Y.; Yan, Y.; Yang, Y.; Sun, Q.; Chan, S. H.; Fisher, A.; Wang, X. Amino Acid Modified Copper Electrodes for the Enhanced Selective Electroreduction of Carbon Dioxide towards Hydrocarbons. *Energy Environ. Sci.* **2016**, *9* (5), 1687–1695. https://doi.org/10.1039/C5EE03694A.

(32) Banerjee, S.; Han, X.; Thoi, V. S. Modulating the Electrode-Electrolyte Interface with Cationic Surfactants in Carbon Dioxide Reduction. *ACS Catal.* **2019**, *9* (6), 5631–5637. https://doi.org/10.1021/acscatal.9b00449.

(33) Baturina, O. A.; Lu, Q.; Padilla, M. A.; Xin, L.; Li, W.; Serov, A.; Artyushkova, K.; Atanassov, P.; Xu, F.; Epshteyn, A.; et al. CO_2 Electroreduction to Hydrocarbons on Carbon-Supported Cu Nanoparticles.

ACS Catal. **2014**, *4* (10), 3682–3695. https://doi.org/10.1021/cs500537y.

(34) Kim, D.; Kley, C. S.; Li, Y.; Yang, P. Copper Nanoparticle Ensembles for Selective Electroreduction of CO_2 to C_2–C_3 Products. *Proc. Natl. Acad. Sci. U. S. A.* **2017**, *114* (40), 10560–10565. https://doi.org/10.1073/pnas.1711493114.

Chapter 2: Effects of Substrate Porosity in Carbon Aerogel Supported Copper for Electrocatalytic Carbon Dioxide Reduction

The work encompassed in this chapter has been published with the following citation and listed authors:

Electrochim. Acta **2019**, *297*, 545–552.

Xu Han,[a] Mei Wang,[b] My Linh Le,[a] Nicholas M. Bedford,[c] Taylor J. Woehl,[b] V. Sara Thoi[a*]

[a]Department of Chemistry, Johns Hopkins University, Baltimore, Maryland 21218, USA. Email: sarathoi@jhu.edu

[b]Department of Chemical and Biomolecular Engineering, University of Maryland, College Park, Maryland, 20740, USA.

[c]Faculty of Engineering, University of South New Wales, Sydney, AU.

Additional spectroscopic, microscopic, and electrochemical data are provided in Appendix A.

2.1 Introduction

Owing to the rise in greenhouse gas emissions and global climate change, conversion of unconventional carbon feedstock to sustainable fuels has become an urgent area of need. Electrochemical reduction of carbon dioxide, an abundant byproduct of fossil fuel combustion, is a promising route for the storage of electricity generated from renewable resources in the form of carbon fuels.[1–4] However, the energetic requirements of the CO_2 reduction reaction (CO_2RR) are high due to a kinetically uphill one-electron reduction of linear CO_2 to form the bent radical anion, $CO_2^{\bullet-}$. Moreover, efficient catalysts must be selective for CO_2RR over the more facile hydrogen evolution reaction (HER).

Among the different strategies for activating CO_2 and stabilizing the high-energy intermediates, metallic surfaces have emerged as a promising route for selective carbon dioxide activation.[5–7] Copper is one of the most active non-precious metal catalysts for CO_2RR with the capability to yield high-order hydrocarbon products, such as methane, ethylene, and alcohols.[8–11] However, HER is often the dominant reaction pathway and the carbon product selectivity of Cu is typically poor. Large research efforts have thus been focused on the development of Cu catalysts to control relative ratios of reduced carbon products.[12–18]

Beyond the catalytic active sites, other catalytic conditions—such as mesostructuring, diffusional concentration gradients, and chemical environment—can have an influential role on CO_2RR. For instance, surface roughness of an oxide-derived Cu catalyst has been shown to be important for selective product formation and HER inhibition.[19] The thickness of a porous catalyst film can also impact the local pH and the diffusion of reactive species.[20–22] Cu_2O and Cu_2O/ZnO catalysts have been shown to enhance

CH_3OH formation.[23] Copper-based metal-organic frameworks and aerogels have also been shown to improve product selectivity towards methanol and ethanol.[24] In addition, several studies have reported that experimental design parameters such as CO_2 flow rate and bubble size may have a drastic influence on the catalytic performance.[25] *These findings clearly illustrate that the mesostructure of the catalyst and solution dynamics are as significant on selective CO_2RR as the identity and morphology of the catalyst itself.*

An interesting approach to control these factors is in metal particles deposited on porous carbon. [26–29] It has been observed that *in situ* Cu nanoparticles electrodeposited on carbon nanotubes (CNTs), graphene oxide (GO), high purity graphite, and glassy carbon are active for CO_2RR, with methane as a significant product albeit at a relatively high potential of −1.3 V vs the reversible hydrogen electrode (RHE).[28] Others have reported high selectivity for C_2H_4 production using Cu nanoparticles (particle size < 100 nm) deposited on various forms of commercial carbons.[29] However, while the catalytic performances of the Cu/C catalysts varied significantly, the lack of systematic control over the carbon substrate properties impeded the elucidation of any trends. To date, there are no reports that provide insights on how the porosity and structure of carbon specifically affect CO_2RR. Understanding the synergistic effects of carbon for catalysis thus remains a major challenge.

To tackle this challenge, we embark on a search for a tunable carbon substrate that has high surface area, porosity, and electrical conductivity. We elect to use carbon aerogels, a unique class of porous carbon that possesses a 3D network of nanographitic sheets and amorphous carbon.[30,31] The aerogel structure is achieved via a sol-gel process and is composed of interconnected primary particles with diameters in the

nanometer range, giving the structure its unique low mass density, continuous porosities, and high surface area. Carbon aerogel can be doped with various metals and was found to enhance the unit activity per metal towards CO_2 reduction. [32] Metal loading and particle size effects have been further studied in the case of cobalt-doped and iron doped carbon aerogel, respectively. [33,34] Moreover, SnO_2 supported on carbon aerogel has been studied for selectively reducing CO_2 to formate. [35] Another advantage of carbon aerogels is the ability to tune their morphology and porosity using a facile sol-gel process. However, there are limited studies that have focused on the systematic control of carbon aerogel pore size to evaluate the impact of substrate porosity on electrocatalysis.

Herein, we report an in-depth study on the effects of carbon porosity on the catalytic performance for CO_2RR. We take advantage of the synthetic versatility of carbon aerogels to control composition and porosity for the deposition of catalytically active Cu particles. While other reports have shown that Cu supported on carbon substrates are competent catalysts for CO_2RR,[14,28,29] carbon structure-activity relationships have not been established. Using low-loading Cu on carbon aerogels, we demonstrate a pore size-selectivity relationship for CO_2RR, particularly for C_2H_4 and CO production. We propose that confinement of reactants and intermediates in the mesopores of the catalytically inactive carbon aerogel play a significant role in total CO_2RR activity and product selectivity. Our results emphasize the importance of substrate properties and encourage further studies on tunable carbon platforms for CO_2RR catalysis and beyond.

2.2 Experimental Procedures

2.2.1 Synthesis of Cu/CA

Carbon aerogels were synthesized by using resorcinol and formaldehyde as precursors. Based on the well-known sol-gel method,[30,36,37] resorcinol was stirred with formaldehyde by a 1:2 molar ratio to form a 5 wt % aqueous solution followed by the addition of varying concentrations of Na_2CO_3 as a base catalyst. The solution was left undisturbed for 48 hours at 30 °C, during which primary particles were formed and an orange solution was generated. The temperature was then increased to 60 °C for another 2 days. To vary the morphology of the aerogel, the molar ratio of resorcinol (R) to the base catalyst (C) was varied at R/C = 180, 300, 400, and 650.

After the gelation process, the wet gels were carefully removed from the container and soaked in reagent alcohol for 12 hours. This process was repeated with a fresh stock of reagent alcohol for another 12 hours. The wet gels were then soaked in dry ethanol for 6 hours on a gently shaking plate to facilitate the removal of residual water, which is necessary for critical point drying. This process was repeated 4 times. Copper was loaded by soaking the wet gel in an ethanol solution containing 15 mg mL^{-1} $Cu(NO_3)_2$ for 12 hours twice. Finally, the wet gel was dried on a Tousimis 795 Critical Point Dryer. The copper-loaded RF aerogel was pyrolyzed at 1050 °C for 5 hours under N_2. The heating rate was 2.5 °C/minute.

2.2.2 Electrode Preparation

Cu/CA was ground to powders by shaking in a plastic vial with stainless steel balls. An ink slurry was prepared by dispersing 3 mg of Cu/CA powder in 1 mL 1:4 (v/v) ethanol water solution. 100 μL 5 wt % Nafion in water and 1-propanol were added as a binder. A 3 mm glassy carbon

electrode and a glassy carbon plate were used as the working electrode for cyclic voltammetry and bulk electrolysis, respectively. The glassy carbon electrode was first cleaned by sonicating in ethanol and DI water. Then it was polished by using alumina particles on a polishing cloth. The electrode for electrolysis was prepared by drop-casting 200 μL catalytic ink on a 1 cm × 2 cm area of glassy carbon plate electrode and allowed to dry under an infrared lamp, which facilitated the formation of a uniform thin film with good surface adhesion. Silicone polyimide tape was used to control the surface area. For controlled experiments, Cu foil and Cu wire electrodes were prepared by mechanical polishing using a 220-grit sand paper.

2.2.3 Controlled-Potential Electrolysis

The experiments were performed in a gas-tight two-compartment electrochemical cell (H-cell) separated by a glass frit with a working electrode and an Ag/AgCl reference electrode on one side and a Pt coil or graphite rod courter electrode. Each compartment was filled with 40 mL 0.1 M $NaHCO_3$ electrolyte with a headspace volume of 30 mL. CO_2 gas was purged through both compartments for at least 15 min before electrolysis. Electrolysis were conducted for 2.5 h between -0.8 V to -1.2 V vs. RHE. The working compartment was directly connected to an Agilent 490 MicroGC to analyze gas products and gas injections were initiated every 1 h. At least three freshly prepared electrodes were independently measured at each potential. The ohmic drop was measured by electrochemical impedance spectroscopy (EIS). The real resistance at 1 x 10^4 Hz on Nyquist plot was taken as the ohmic drop for the system and all potentials reported are IR compensated. The potential was converted to V vs. Reversible Hydrogen Electrode (RHE) by the following equation:

$$E\ (vs\ RHE) = E\ \left(vs\frac{Ag}{AgCl}\right) + 0.209\ V + 0.0591\ pH + R\ I$$

where the *pH* was 6.8, *R* is the solution resistance measured by EIS, and *I* is the average current during the electrolysis. Gas products were analyzed by an Agilent 490 Micro GC equipped with a thermal conductivity detector (TCD), a Molsieve 5Å column and a PoraPlot U (PPU) column. The Molsieve column was used to separate H_2, CO, and CH_4, while the PPU column was used to separate C_2H_4 and other hydrocarbons. Isotopic labeling experiments demonstrate carbon products are derived from CO_2 and additional control experiments are available in the ESI.

2.3 Synthesis and Characterization of Cu/CA

Copper-deposited carbon aerogels are synthesized by the Pekala's method.[30] In contrast to commercial carbons, this facile synthesis of carbon aerogels does not use metal catalysts and allows for careful control of trace impurities. The carbon framework is formed from the condensation of resorcinol (R) and formaldehyde (F) in the presence of catalytic amounts of Na_2CO_3 (**Figure A1**).[36,37] Upon heating the sol, the condensation products of resorcinol and formaldehyde can undergo a number of etherification and Michael Addition reactions to yield polymeric microspheres called primary particles. When the concentration of these particles reaches a threshold, crosslinking of individual microspheres leads to the formation of a 3-dimensional interconnected porous network. The organic gel subsequently undergoes several solvent exchanges with dry ethanol to remove excess precursors and water. Copper ions are loaded by soaking the wet gel, which contains –OH functional groups, in a dry ethanolic solution of a copper salt. The liquid solvent is gently removed with critical point CO_2 drying method to retain the porous structure of the RF gel. Pyrolysis of the sample results in a

simultaneous carbonation of the organic aerogel as well as the formation of Cu particles.

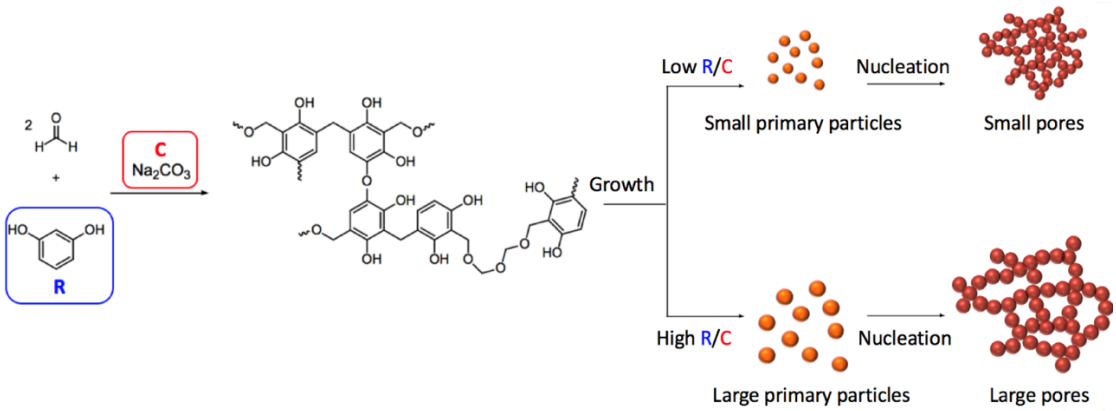

Scheme 2.2. Impact of resorcinol to catalyst ratio (R/C) on the growth of primary carbon particles and aerogel porosity.

To vary the porosity and morphology of carbon aerogels, the molar ratio of resorcinol to Na_2CO_3 (R/C) is adjusted. (**Scheme 2.1**). A low catalyst concentration favors the growth of polymeric spheres, while a high catalyst concentration leads to enhanced crosslinking of microspheres. Thus, a high R/C ratio will generate a gel structure with large particles and fewer cross linkages. Correspondingly, pyrolysis of this material will yield a carbon aerogel with large mesopores (2-50 nm).[38,39] In this manner, we synthesize four Cu-deposited carbon aerogels with varying carbon structures using R/C ratios of 180 (Cu/CA-180), 300 (Cu/CA-300), 400 (Cu/CA-400), and 650 (Cu/CA-650) as well as the respective metal-free carbon aerogels.

A combination of spectroscopic and imaging techniques is used to characterize the Cu-loaded carbon support. First, Atomic Absorption Spectroscopy (AAS) is utilized to determine the total Cu concentration per sample mass of Cu/CA. All four samples contain similar Cu content ranging between 8 and 13% (**Table A1**). In addition, the powder X-ray diffraction (PXRD) measurements indicate the presence of metallic Cu and Cu_2O

(**Figure A2**). The Cu_2O component is due to a slow oxidization of the Cu particle under ambient conditions. The peak intensity ratio of Cu_2O (200) to Cu(200) are similar across all four samples, suggesting that Cu/CAs have similar levels of oxidation.

X-ray Photoelectron Spectroscopy (XPS) is used to examine Cu/CA-180 as a representative sample. Interestingly, no Cu is detected on the surface of the sample by XPS. XPS depth profiling reveals that Cu is evenly distributed throughout the 3D carbon network. At the depth of ~300 nm, Cu constitutes about 5 wt% of the material (**Figure A3**) as corroborated by Energy Dispersive X-ray Spectroscopy (EDS) compositional analysis (**Table A1**). Likewise, Scanning Electron Microscopy (SEM) shows uniform deposition of Cu particles on the highly porous carbon 3D framework (**Figure A4**).

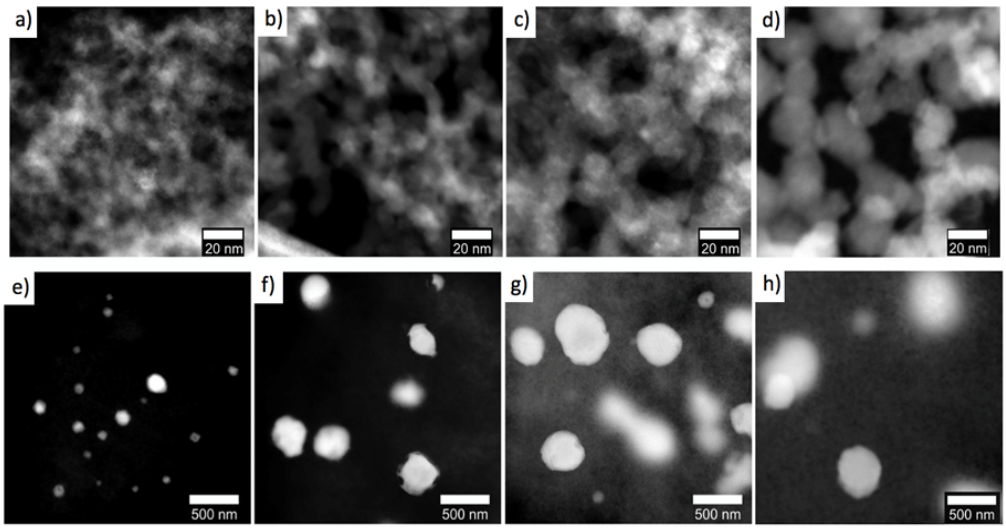

Figure 2.4. Annular dark field STEM images of (a-d) carbon aerogel supports and (e-h) Cu particles for Cu/CA-180, Cu/CA-300, Cu/CA-400, and Cu/CA-650 (left to right).

Transmission electron microscopy (TEM) and scanning TEM (STEM) are used to characterize the Cu particles and the structure of the carbon

support. Annular Dark Field (ADF) STEM images of each sample reveal the Cu particle sizes of Cu/CA-300, Cu/CA-400, and Cu/CA-650 are similar, ranging in average particle size of 315-335 nm, while Cu/CA-180 exhibits an average particle size of 75 nm (**Figure 2.1** and **Figure A5**). The STEM-EDS measurements (**Figure A6**) are consistent with XRD that the Cu particles undergo surface oxidation to form Cu_2O shells. For the carbon structure, ADF-STEM images support that high R/C ratios lead to the generation of large primary carbon particles during the aerogel synthesis (**Figure 1a-d**). The thickness of the carbon framework and the porosity are increasing in the order of Cu/CA-180 < Cu/CA-300 ~ Cu/CA-400 < Cu/CA-650.

High Resolution TEM (HRTEM) images of the carbon substrate reveal both graphitic and amorphous carbon (**Figure A7a,b**). In Raman Spectroscopy, amorphous carbon typically displays a disorder-induced D-band at 1348 cm^{-1}, while graphite exhibits a first-order allowed G band at 1591 cm^{-1}.[40,41] The Raman spectra in **Figure A7c** illustrate that the Cu/CAs have similar intensity ratios of D to G bands, implicating that they consist of similar fractions of amorphous carbon and graphitic domains.

The porosity of the carbon aerogel is further characterized using isothermal nitrogen adsorption methods (**Figure A8**). All four samples exhibit high BET surface areas:[39] Cu/CA-180 (1236 $m^2 g^{-1}$), Cu/CA-300 (832 $m^2 g^{-1}$), Cu/CA-400 (940 $m^2 g^{-1}$), and Cu/CA-650 (940 $m^2 g^{-1}$). The desorption branches of the nitrogen isotherms are modeled by the Barrett-Joyner-Halenda (BJH) method, which is commonly used for examining mesoporosity (2-50 nm) of carbon materials. Consistent with ADF STEM images (**Figure 2.1**), the pore size distributions (PSD) clearly show the Cu/CA samples exhibit drastically different pore sizes (**Figure 2.2**) with the peak and average mesopore diameters increasing in the order of Cu/CA-

180 < Cu/CA-300 < Cu/CA-400 < Cu/CA-650. This trend is also corroborated by Hg porosimetry (**Figure A9**). Density functional theory (DFT) modeling of the nitrogen isotherms shows all four Cu/CA samples have similar microporosity (< 2 nm) (**Figure A10**).

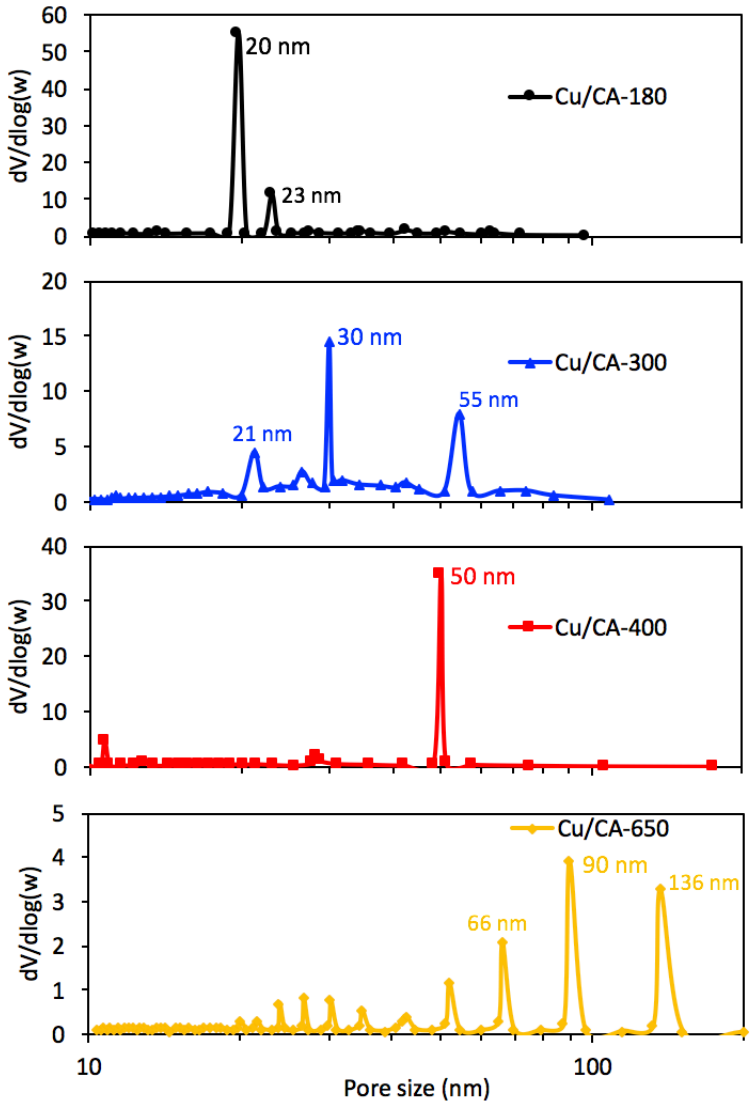

Figure 2.5. BJH pore size distribution showing varying of pore widths at different R/C ratios.

2.4 Electrocatalytic CO_2 Reduction

To examine the overall electrochemical behavior of Cu/CA, linear sweep voltammetry (LSV) experiments are performed in a pH 6.8 solution of

0.1 M $NaHCO_3$ saturated with CO_2. All four Cu/CA electrodes show a large current enhancement indicative of catalytic activity with an onset potential of –0.7 V vs. RHE (**Figure A11**). Beyond the potential –1.05 V vs. RHE, Cu/CA-300 and Cu/CA-400 have higher current densities compared to Cu/CA-180 and Cu/CA-650.

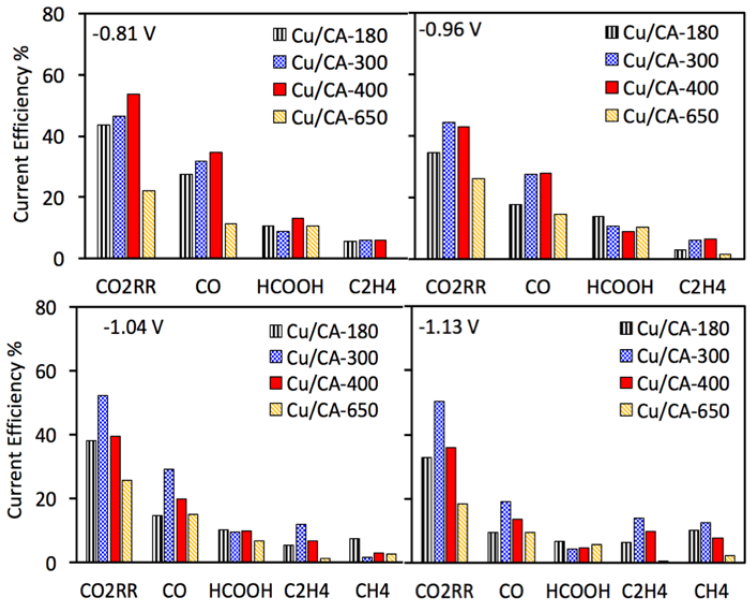

Figure 2.6. Comparison of CO_2RR product selectivity at 4 potentials. At lower potentials, Cu/CA-300 and Cu/CA-400 have higher selectivity for reduced CO_2 products than Cu/CA-180 and Cu/CA-650.

Controlled potential electrolysis correlate with the performance seen in LSV. In general, CO_2RR current efficiencies are the highest in Cu/CA-300 and Cu/CA-400, reaching up to 50% (**Figure 2.3**). We note that the Cu loading in Cu/CAs is only 8-13 wt% (**Table A1**), yet the catalysts exhibit enhanced CO_2RR current efficiency as 50 wt% Cu/carbon catalyst reported previously at this potential.[29] Other carbon-supported Cu catalysts with similar low loadings also show significant HER current efficiency.[14,28] Moreover, bulk Cu foil have a drastically different product distribution with higher HER Faradaic efficiencies compared to Cu/CAs (**Figures A12**).

Interestingly, CO_2RR current efficiency is correlated with the carbon porosity. **Figure 2.4** shows the largest selectivity occurs at the carbon peak pore size between 30 and 50 nm (i.e. Cu/CA-300 and Cu/CA-400). As the pore size increases from 20 nm, CO_2 is able to diffuse more easily to the Cu active site, resulting in the notable enhancement in CO_2RR current efficiency (**Figure 2.4a**). However, a precipitous drop in current efficiency is observed after 50 nm. We postulate that at larger pore sizes, CO_2RR efficiency is influenced by the confinement of reactive intermediates near the active site.[15,20] This phenomenon has been observed in ordered nanoporous Cu electrocatalysts, where it is reported that increasing the pore size leads to a less stable ion concentration at the Cu surface and consequently poorer CO_2RR selectivity.[15] Likewise, the larger peak pore sizes in the nanoporous carbon aerogel of Cu/CA-650 may perturb the reaction environment and result in a decreased CO_2RR current efficiency.

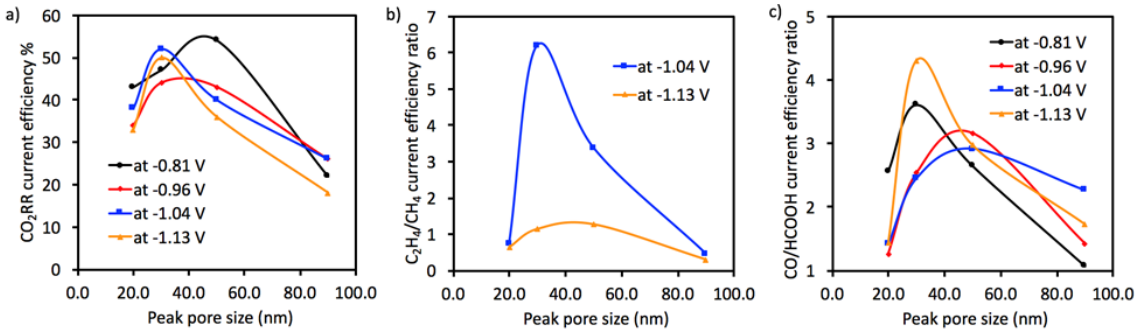

Figure 2.4. (a) Plot of total CO_2RR current as a function of pore size at various potentials. The pore size is determined by the peak position in the PSD. Comparison of product selectivity ratios of (b) CO to HCO_2H and (c) C_2H_4 to CH_4 at 4 potentials. In general, Cu/CA-300 and Cu/CA-400 have higher selectivity for reduced CO_2 products, illustrating an optimal pore size distribution.

Supporting our observations, the selectivities for C_2H_4 and CO display a similar inverted parabola trend as a function of pore size. It has been reported that confinement of reactive intermediates promote the formation of higher order species such as ethylene.[20] In **Figure 2.4b**, the current

efficiency ratios of C_2H_4 to CH_4 are the highest for the 30-50 nm pore size range of Cu/CA-300 and Cu/CA-400, particularly at the potential of -1.04 V vs. RHE. At the extremes, Cu/CA-180 and Cu/CA-650 exhibit a C_2H_4/CH_4 ratio of less than 1, suggesting the balance of CO_2 diffusion and ion confinement is not optimal. The current efficiency ratio of CO/HCO_2H can also elucidate fundamental changes in the microenvironment of the active Cu sites. The CO/HCO_2H ratio of Cu/CA-300 and Cu/CA-400 are higher than the extreme Cu/CA cases (**Figure 2.4c**). In all cases, both C_2H_4/CH_4 and CO/HCO_2H product ratios of Cu/CA are significantly greater than that of a bulk Cu foil under our experimental parameters (**Figure 2.4**, **Figure A12**).

As the Cu particles are embedded in the carbon aerogel, the electrochemically active surface area (EASA) of Cu/CAs may vary. To determine if surface area accounts for the differences in catalytic activity, an Cu/CA nafion ink of each catalyst is deposited on a 3 mm glassy carbon electrode and the cyclic voltammograms of an aqueous solution of $K_3Fe(CN)_5$. As shown in Figure A13, the reversible Fe^{2+}/Fe^{3+} redox feature at 0.23 V vs Ag/AgCl has a similar shape and intensity for all four catalysts. Using the Randles-Sevcik equation, the EASA values for Cu/CA-180, Cu/CA-300, Cu/CA-400, and Cu/CA-650 are comparable (14.0 ± 1.5 cm^2 mg^{-1} Cu, **Table A2**). This result suggests that variations in Cu surface area are not the primary reason for the observed catalytic trends.

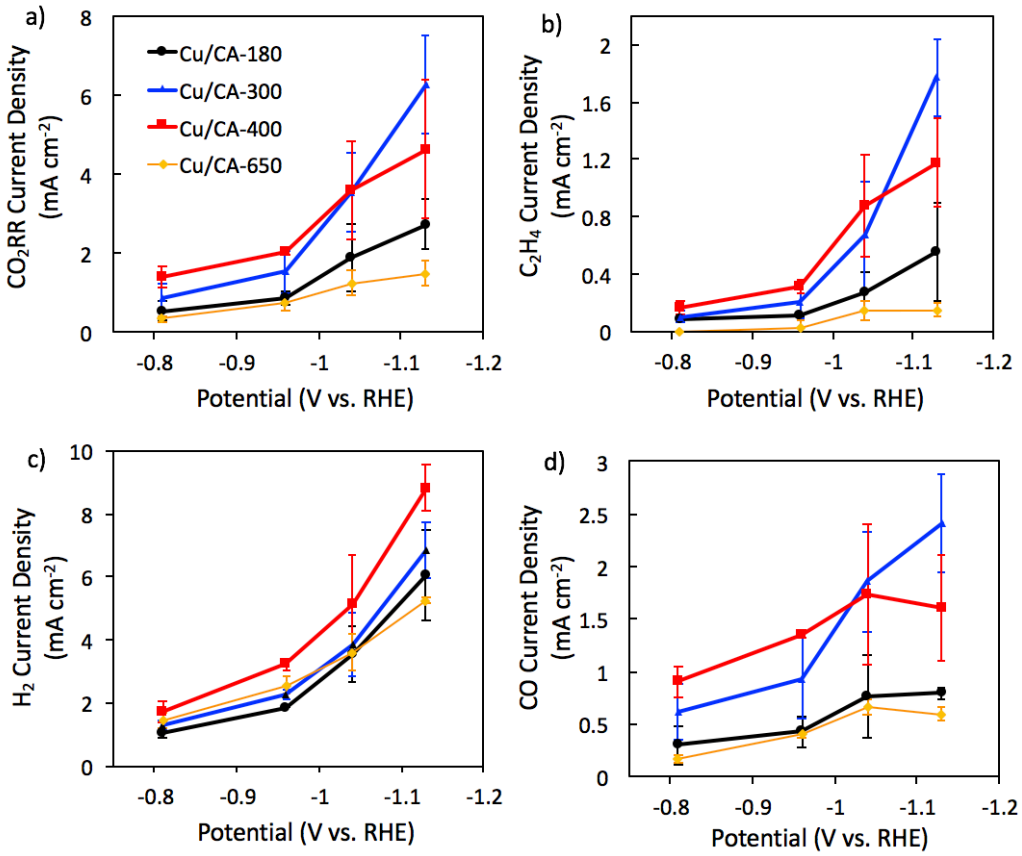

Figure 2.5. Comparison of CO_2RR current density as a function of potential. Cu/CA-300 and Cu/CA-400 are more active catalysts than Cu/CA-180 and Cu/CA-650, demonstrating the impact of carbon structure on CO_2RR.

To study the influence of carbon structure on the catalytic activity, the specific current density and formation rate of HER and CO_2RR for the Cu/CA catalysts are examined (**Figure 2.5**, **Figure A14**). At all potentials tested, Cu/CA-300 and Cu/CA-400 exhibit the higher total current density towards CO_2RR compared to Cu/CA-180 and Cu/CA-650 (**Figure 2.5a**). This enhancement is mainly due to the improved C_2H_4 and CO current densities (Figure 5b,d) since the specific current densities for HCO_2H and CH_4 are invariant across the tested potential range (**Figure A15**). Furthermore, the HER current density is comparable among the samples except for the slightly higher activity for Cu/CA-400. (**Figure 2.5c**). This outcome stands in contrast with previous reports on mesoporous Cu and Au electrodes, where

an increase in CO_2RR selectivity is attributed to the suppression of HER due to increasing local pH.[20,21] The similar HER current densities imply that the local pH is comparable for the four catalysts despite their differences in mesoporosity. In addition, LSV experiments of metal-free carbon aerogels in CO_2 saturated 0.1 M $NaHCO_3$ solutions show similar HER current densities at all potentials (**Figure A16**) and validate that porosity of the aerogels does not impact HER activity.

X-ray absorption spectroscopy (XAS) experiments are performed to evaluate if the differences in product selectivity are related to compositional variance of the Cu particles. In the X-ray absorption near-edge structure (XANES) portion of the spectra (**Figure A17**), the tested Cu/CA samples contain features in the absorption edge that are similar to those of a bulk Cu_2O powder.[42] This result is consistent with XRD and TEM analysis that the metallic Cu particles in the carbon aerogels are partially oxidized to Cu_2O. We further use the extended X-ray absorption fine structure (EXAFS) region to examine the extent of oxidation and the local Cu environment. EXAFS modeling (**Figure A17**, **Figure A18**) provides quantitative structure metrics, such as coordination numbers (CNs) and nearest neighbor distances (NNDs), which are provided in **Table A3** and **A4**. Despite the large particle sizes observed in TEM, all modeled metal oxide CNs are reduced from the bulk value of 4.0 for Cu-O and 8.0 for Cu-Cu. Correspondingly, the model NNDs are slightly expanded from the known NNDs in Cu_2O (1.84 Å and 3.01 Å for Cu-O and Cu-Cu NNDs respectively). This outcome signifies nanoscale ordering of the Cu_2O shell within the aerogels, which are not uncommon as surface strain and interfacial interactions can lead to differences between bulk and nanoscale properties.[43–45] More importantly, the reduced CNs and expanded NNDs reveal that the nanoscale domains in

the Cu/CA samples are similar. Although the complexity of the Cu/CA structure precludes *in-situ* characterization of the Cu particles during electrolysis, the XAS data suggests that all four catalysts will generate comparable Cu sites upon reductive conditions.[19] Compositional differences of the active sites thus are unlikely to fully account for the varied CO_2RR product selectivity.

Taken together, our extensive spectroscopic and microscopic characterization suggest that the surfaces of the Cu particles are comparable in the Cu/CA series. Moreover, differences in catalytic performances are not likely due to nano-sized effects previously observed in 1-10 nm Cu nanoparticles given the large Cu particle sizes (~300 nm) in this study.[46,47] Our careful characterization of the carbon aerogel signifies that while Cu/CA are compositionally similar, the mesoporous structure plays an important role in the overall CO_2RR selectivity (**Table 2.1**).

Table 2.1. Comparison of Cu/CA material properties and catalytic activity.

		Cu/CA-180	Cu/CA-300	Cu/CA-400	Cu/CA-650	
Cu Particle	Cu weight % by EDS	8.5 ± 0.5	7.7 ± 0.4	6.9 ± 0.6	7.7 ± 0.9	→
	Cu weight % by AA	9.7 ± 0.6	11 ± 0.6	7.8 ± 0.5	12 ± 0.7	~
	Average size	75 nm	315 nm	330 nm	335 nm	⌐→
	$Cu_2O(200)$/ Cu(200)*	2.8	2.5	2.6	2.6	→
Carbon Aerogel	Peak pore size	20 nm	30 nm	50 nm	90 nm	↗
	Average pore size (>10 nm)	32 nm	40 nm	43 nm	64 nm	↗
CO_2RR Efficiency	at -0.81 V	43 %	46 %	54 %	22 %	∩
	at -0.96 V	34 %	44 %	43 %	26 %	∩
	at -1.04 V	38 %	52 %	39 %	26 %	∩
	at -1.13 V	33 %	50 %	36 %	18 %	∩

* Peak intensity ratio from powder XRD measurements

2.5 Conclusions

In summary, carbon aerogel supported copper is a novel platform for studying electrocatalytic reduction of CO_2. The tunability of the carbon substrate allows direct comparisons of catalytic performance as a function of porosity. We demonstrate that Cu/CAs possessing intermediate pore sizes lead to increased selectivity for CO_2RR and notable product selectivity of CO over HCO_2H and C_2H_4 over CH_4. While adjusting the carbon porosity can lead to a 2-fold enhancement in CO_2RR, the morphology of the carbon aerogel plays a less significant role in HER. To our knowledge, this is the first systematic study on the influence of the porous carbon support on the selectivity and activity of electrocatalytic CO_2RR. Future studies are focused on templated mesoporosity in carbon materials to provide greater control over the PSD and further elucidate structure-activity relationships. Our findings have implications on the design and development of supported catalysts in carbon dioxide conversion and other industrially relevant catalytic processes.

2.6 References

(1) Khezri, B.; Fisher, A. C.; Pumera, M.; Murata, A.; Koga, O.; Sakurai, H.; Oguma, K.; Watanabe, M.; Yan, F.; Zheng, W.; et al. CO_2 Reduction: The Quest for Electrocatalytic Materials. *J. Mater. Chem. A* **2017**, *5* (18), 8230–8246. https://doi.org/10.1039/C6TA09875D.

(2) Kortlever, R.; Shen, J.; Schouten, K. J. P.; Calle-Vallejo, F.; Koper, M. T. M. Catalysts and Reaction Pathways for the Electrochemical Reduction of Carbon Dioxide. *J. Phys. Chem. Lett.* **2015**, *6* (20), 4073–4082. https://doi.org/10.1021/acs.jpclett.5b01559.

(3) Benson, E. E.; Kubiak, C. P.; Sathrum, A. J.; Smieja, J. M. Electrocatalytic and Homogeneous Approaches to Conversion of CO_2 to Liquid Fuels. *Chem. Soc. Rev.* **2009**, *38* (1), 89–99. https://doi.org/10.1039/b804323j.

(4) Li, Y.; Chan, S. H.; Sun, Q. Heterogeneous Catalytic Conversion of CO_2 : A Comprehensive Theoretical Review. *Nanoscale* **2015**, *7* (19), 8663–8683. https://doi.org/10.1039/C5NR00092K.

(5) Hori, Y.; Takahashi, I.; Koga, O.; Hoshi, N. Selective Formation of C2 Compounds from Electrochemical Reduction of CO_2 at a Series of Copper Single Crystal Electrodes. *J. Phys. Chem. B* **2002**, *106* (1), 15–17. https://doi.org/10.1021/jp013478d.

(6) Hori, Y.; Murata, A.; Yoshinami, Y. Adsorption of CO, Intermediately Formed in Electrochemical Reduction of CO_2, at a Copper Electrode. *J. Chem. Soc. Faraday Trans.* **1991**, *87* (1), 125. https://doi.org/10.1039/ft9918700125.

(7) Hori, Y.; Wakebe, H.; Tsukamoto, T.; Koga, O. Electrocatalytic Process of CO Selectivity in Electrochemical Reduction of CO_2 at Metal Electrodes in Aqueous Media. *Electrochim. Acta* **1994**, *39* (11–12), 1833–1839. https://doi.org/http://dx.doi.org/10.1016/0013-4686(94)85172-7.

(8) Kuhl, K. P.; Cave, E. R.; Abram, D. N.; Jaramillo, T. F. New Insights into the Electrochemical Reduction of Carbon Dioxide on Metallic Copper Surfaces. *Energy Environ. Sci.* **2012**, *5* (5), 7050–7059. https://doi.org/10.1039/c2ee21234j.

(9) Whipple, D. T.; Kenis, P. J. A. Prospects of CO_2 Utilization via Direct Heterogeneous Electrochemical Reduction. *J. Phys. Chem. Lett.* **2010**, *1* (24), 3451–3458. https://doi.org/10.1021/jz1012627.

(10) Gattrell, M.; Gupta, N.; Co, A. A Review of the Aqueous Electrochemical Reduction of CO_2 to Hydrocarbons at Copper. *J. Electroanal. Chem.* **2006**, *594* (1), 1–19. https://doi.org/10.1016/j.jelechem.2006.05.013.

(11) Merino-Garcia, I.; Albo, J.; Irabien, A. Productivity and Selectivity of Gas-Phase CO_2 Electroreduction to Methane at Copper Nanoparticle-Based Electrodes. *Energy Technol.* **2017**, *5* (6), 922–928. https://doi.org/10.1002/ente.201600616.

(12) Durand, W. J.; Peterson, A. A.; Studt, F.; Abild-Pedersen, F.; Nørskov, J. K. Structure Effects on the Energetics of the Electrochemical Reduction of CO_2 by Copper Surfaces. *Surf. Sci.* **2011**, *605* (15–16), 1354–1359. https://doi.org/10.1016/j.susc.2011.04.028.

(13) Raciti, D.; Livi, K. J.; Wang, C. Highly Dense Cu Nanowires for Low-Overpotential CO_2 Reduction. *Nano Lett.* **2015**, *15*, 6829–6835. https://doi.org/10.1021/acs.nanolett.5b03298.

(14) Kim, D.; Kley, C. S.; Li, Y.; Yang, P. Copper Nanoparticle Ensembles for Selective Electroreduction of CO_2 to C_2–C_3 Products. *Proc. Natl. Acad. Sci. U. S. A.* **2017**, *114* (40), 10560–10565. https://doi.org/10.1073/pnas.1711493114.

(15) Yang, K. D.; Ko, W. R.; Lee, J. H.; Kim, S. J.; Lee, H.; Lee, M. H.; Nam, K.

T. Morphology-Directed Selective Production of Ethylene or Ethane from CO_2 on a Cu Mesopore Electrode. *Angew. Chemie Int. Ed.* **2017**, *56* (3), 796–800. https://doi.org/10.1002/anie.201610432.

(16) Kas, R.; Hummadi, K. K.; Kortlever, R.; De Wit, P.; Milbrat, A.; Luiten-Olieman, M. W. J.; Benes, N. E.; Koper, M. T. M.; Mul, G. Three-Dimensional Porous Hollow Fibre Copper Electrodes for Efficient and High-Rate Electrochemical Carbon Dioxide Reduction. *Nat. Commun.* **2016**, *7*, 1–7. https://doi.org/10.1038/ncomms10748.

(17) Zhu, X.; Gupta, K.; Bersani, M.; Darr, J. A.; Shearing, P. R.; Brett, D. J. L. Electrochemical Reduction of Carbon Dioxide on Copper-Based Nanocatalysts Using the Rotating Ring-Disc Electrode. *Electrochim. Acta* **2018**, *283*, 1037–1044. https://doi.org/10.1016/j.electacta.2018.07.025.

(18) Jiwanti, P. K.; Natsui, K.; Nakata, K.; Einaga, Y. The Electrochemical Production of C_2/C_3 Species from Carbon Dioxide on Copper-Modified Boron-Doped Diamond Electrodes. *Electrochim. Acta* **2018**, *266*, 414–419. https://doi.org/10.1016/j.electacta.2018.02.041.

(19) Li, C. W.; Kanan, M. W. CO 2 Reduction at Low Overpotential on Cu Electrodes Resulting from the Reduction of Thick Cu_2O Films. *J. Am. Chem. Soc.* **2012**, *134* (17), 7231–7234. https://doi.org/10.1021/ja3010978.

(20) Sen, S.; Liu, D.; Palmore, G. T. R. Electrochemical Reduction of CO_2 at Copper Nanofoams. *ACS Catal.* **2014**, *4* (9), 3091–3095. https://doi.org/10.1021/cs500522g.

(21) Hall, A. S.; Yoon, Y.; Wuttig, A.; Surendranath, Y. Mesostructure-Induced Selectivity in CO_2 Reduction Catalysis. *J. Am. Chem. Soc.* **2015**, *137* (47), 14834–14837. https://doi.org/10.1021/jacs.5b08259.

(22) Chen, C.; Zhang, B.; Zhong, J.; Cheng, Z. Selective Electrochemical CO2 Reduction over Highly Porous Gold Films. *J. Mater. Chem. A* **2017**, *5*, 21955–21964. https://doi.org/10.1039/C7TA04983H.

(23) Albo, J.; Sáez, A.; Solla-Gullón, J.; Montiel, V.; Irabien, A. Production of Methanol from CO_2 Electroreduction at Cu_2O and Cu_2O/ZnO-Based Electrodes in Aqueous Solution. *Appl. Catal. B Environ.* **2015**, *176–177*, 709–717. https://doi.org/10.1016/j.apcatb.2015.04.055.

(24) Albo, J.; Vallejo, D.; Beobide, G.; Castillo, O.; Castaño, P.; Irabien, A. Copper-Based Metal–Organic Porous Materials for CO_2 Electrocatalytic Reduction to Alcohols. *ChemSusChem* **2017**, *10* (6), 1100–1109. https://doi.org/10.1002/cssc.201600693.

(25) Billy, J. T.; Co, A. C. Experimental Parameters Influencing the Hydrocarbon Selectivity During the Electrochemical Conversion of CO_2. *ACS Catal.* **2017**, *7*, 8467–8479. https://doi.org/10.1021/acscatal.7b02373.

(26) Geioushy, R. A.; Khaled, M. M.; Alhooshani, K.; Hakeem, A. S.; Rinaldi, A. Graphene/ZnO/Cu2O Electrocatalyst for Selective Conversion of CO_2 into n-Propanol. *Electrochim. Acta* **2017**, *245*, 456–462. https://doi.org/10.1016/j.electacta.2017.05.185.

(27) Pan, F.; Zhao, H.; Deng, W.; Feng, X.; Li, Y. A Novel N,Fe-Decorated

Carbon Nanotube/Carbon Nanosheet Architecture for Efficient CO2reduction. *Electrochim. Acta* **2018**, *273*, 154–161. https://doi.org/10.1016/j.electacta.2018.04.047.

(28) Lum, Y.; Kwon, Y.; Lobaccaro, P.; Chen, L.; Clark, E. L.; Bell, A. T.; Ager, J. W. Trace Levels of Copper in Carbon Materials Show Significant Electrochemical CO_2 Reduction Activity. *ACS Catal.* **2016**, *6* (1), 202–209. https://doi.org/10.1021/acscatal.5b02399.

(29) Baturina, O. A.; Lu, Q.; Padilla, M. A.; Xin, L.; Li, W.; Serov, A.; Artyushkova, K.; Atanassov, P.; Xu, F.; Epshteyn, A.; et al. CO_2 Electroreduction to Hydrocarbons on Carbon-Supported Cu Nanoparticles. *ACS Catal.* **2014**, *4* (10), 3682–3695. https://doi.org/10.1021/cs500537y.

(30) Pekala, R. W.; Schaefer, D. W. Structure of Organic Aerogels. 1. Morphology and Scaling. *Macromolecules* **1993**, *26* (20), 5487–5493. https://doi.org/10.1021/ma00072a029.

(31) Biener, J.; Stadermann, M.; Suss, M.; Worsley, M. a.; Biener, M. M.; Rose, K. a.; Baumann, T. F. Advanced Carbon Aerogels for Energy Applications. *Energy Environ. Sci.* **2011**, *4* (3), 656–667. https://doi.org/10.1039/c0ee00627k.

(32) Pérez-Cadenas, A. F.; Ros, C. H.; Morales-Torres, S.; Pérez-Cadenas, M.; Kooyman, P. J.; Moreno-Castilla, C.; Kapteijn, F. Metal-Doped Carbon Xerogels for the Electro-Catalytic Conversion of CO_2 to Hydrocarbons. *Carbon N. Y.* **2013**, *56*, 324–331.

https://doi.org/10.1016/j.carbon.2013.01.019.

(33) Abdelwahab, A.; Castelo-Quibén, J.; Pérez-Cadenas, M.; Elmouwahidi, A.; Maldonado-Hódar, F.; Carrasco-Marín, F.; Pérez-Cadenas, A. Cobalt-Doped Carbon Gels as Electro-Catalysts for the Reduction of CO_2 to Hydrocarbons. *Catalysts* **2017**, *7* (1), 25. https://doi.org/10.3390/catal7010025.

(34) Castelo-Quibén, J.; Abdelwahab, A.; Pérez-Cadenas, M.; Morales-Torres, S.; Maldonado-Hódar, F. J.; Carrasco-Marín, F.; Pérez-Cadenas, A. F. Carbon - Iron Electro-Catalysts for CO_2 reduction. The Role of the Iron Particle Size. *J. CO_2 Util.* **2018**, *24*, 240–249. https://doi.org/10.1016/j.jcou.2018.01.007.

(35) Yu, J.; Liu, H.; Song, S.; Wang, Y.; Tsiakaras, P. Electrochemical Reduction of Carbon Dioxide at Nanostructured SnO_2/Carbon Aerogels: The Effect of Tin Oxide Content on the Catalytic Activity and Formate Selectivity. *Appl. Catal. A Gen.* **2017**, *545*, 159–166. https://doi.org/10.1016/j.apcata.2017.07.043.

(36) Kim, S. J.; Hwang, S. W.; Hyun, S. H. Preparation of Carbon Aerogel Electrodes for Supercapacitor and Their Electrochemical Characteristics. *J. Mater. Sci.* **2005**, *40* (3), 725–731. https://doi.org/10.1007/s10853-005-6313-x.

(37) Mulik, S.; Sotiriou-leventis, C.; Leventis, N. Time-Efficient Acid-Catalyzed Synthesis of Resorcinol - Formaldehyde Aerogels. *Chem. Mater.* **2007**, *19*

(19), 6138–6144. https://doi.org/doi:10.1021/cm071572m.

(38) Fonseca-Correa, R. A.; Bastidas-Barranco, M. J.; Giraldo, L.; Moreno-Piraján, J. C. Carbon Aerogels: A Study with Different Models of the Effect Resorcinol/Catalyst at Different Ratios after Pyrolysis and the Effect on Textural Properties. *Eur. J. Chem.* **2017**, *8* (3), 279–287. https://doi.org/10.5155/eurjchem.8.3.279-287.1593.

(39) Elkhatat, A. M.; Al-Muhtaseb, S. A. Advances in Tailoring Resorcinol-Formaldehyde Organic and Carbon Gels. *Adv. Mater.* **2011**, *23* (26), 2887–2903. https://doi.org/10.1002/adma.201100283.

(40) Jorio, A.; Ferreira, E. H. M.; Moutinho, M. V. O.; Stavale, F.; Achete, C. A.; Capaz, R. B. Measuring Disorder in Graphene with the G and D Bands. *Phys. status solidi* **2010**, *247* (11–12), 2980–2982. https://doi.org/10.1002/pssb.201000247.

(41) Ferrari, A. C. Raman Spectroscopy of Graphene and Graphite: Disorder, Electron–Phonon Coupling, Doping and Nonadiabatic Effects. *Solid State Commun.* **2007**, *143*, 47–57. https://doi.org/10.1016/j.ssc.2007.03.052.

(42) Prestipino, C.; Regli, L.; Vitillo, J. G.; Bonino, F.; Damin, A.; Lamberti, C.; Zecchina, A.; Solari, P. L.; Kongshaug, K. O.; Bordiga, S. Local Structure of Framework Cu(II) in HKUST-1 Metallorganic Framework: Spectroscopic Characterization upon Activation and Interaction with Adsorbates. *Chem. Mater.* **2006**, *18* (5), 1337–1346. https://doi.org/10.1021/cm052191g.

(43) Zheng, J.-C.; Frenkel, a. I.; Wu, L.; Hanson, J.; Ku, W.; Božin, E. S.;

Billinge, S. J. L.; Zhu, Y. Nanoscale Disorder and Local Electronic Properties of $CaCu_3Ti_4O_{12}$: An Integrated Study of Electron, Neutron, and x-Ray Diffraction, x-Ray Absorption Fine Structure, and First-Principles Calculations. *Phys. Rev. B* **2010**, *81*, 144203. https://doi.org/10.1103/PhysRevB.81.144203.

(44) Bouchet, R.; Weibel, A.; Knauth, P.; Mountjoy, G.; Chadwick, A. V. EXAFS Study of Dopant Segregation (Zn, Nb) in Nanocrystalline Anatase (TiO_2). *Chem. Mater.* **2003**, *15* (26), 4996–5002. https://doi.org/10.1021/cm034640n.

(45) Bedford, N. M.; Showalter, A. R.; Woehl, T. J.; Hughes, Z. E.; Lee, S.; Reinhart, B.; Ertem, S. P.; Coughlin, E. B.; Ren, Y.; Walsh, T. R.; et al. Peptide-Directed PdAu Nanoscale Surface Segregation: Toward Controlled Bimetallic Architecture for Catalytic Materials. *ACS Nano* **2016**, *10* (9), 8645–8659. https://doi.org/10.1021/acsnano.6b03963.

(46) Reske, R.; Mistry, H.; Behafarid, F.; Roldan Cuenya, B.; Strasser, P. Particle Size Effects in the Catalytic Electroreduction of CO_2 on Cu Nanoparticles. *J. Am. Chem. Soc.* **2014**, *136* (19), 6978–6986. https://doi.org/10.1021/ja500328k.

(47) Gao, D.; Zhou, H.; Wang, J.; Miao, S.; Yang, F.; Wang, G.; Wang, J.; Bao, X. Size-Dependent Electrocatalytic Reduction of CO_2 over Pd Nanoparticles. *J. Am. Chem. Soc.* **2015**, *137*, 4288–4291. https://doi.org/10.1021/jacs.5b00046.

Chapter 3: Non-Innocent Role of Porous Carbon Towards Enhancing C_{2-3} Products in Electroreduction of Carbon Dioxide

The work encompassed in this chapter has been published with the following citation and listed authors:

ACS Appl. Mater. Interfaces **2020**, XXXX, XXX, XXX-XXX

Xu Han, V. Sara Thoi*

Department of Chemistry, Johns Hopkins University, Baltimore, Maryland 21218, USA.

Additional figures and tables on characterizations as well as electrolysis data and comparison to recent reports are provided in Appendix B.

3.1 Introduction

The electrochemical CO_2 reduction reaction (CO_2RR) is a sustainable approach to address the rise in greenhouse gas emissions and utilize CO_2 as an abundant carbon feedstock. Tremendous efforts have been taken to tackle the high kinetic barrier of CO_2 activation and the competition of the hydrogen evolution reaction (HER) in aqueous solutions. Innovative strategies include controlling catalyst morphology and composition,[1–6] manipulating oxidation state and adsorption energies,[7,8] and regulating the local electrode environment.[9–12] Recent studies have utilized surface modification on metal films to dramatically alter product selectivity. Pyridinium-based and polyamide films on Cu were shown to suppress hydrogen production and favor $C_{\geq 2}$ formation.[13–15] More recently, hydrophobicity of the Cu film was demonstrated to be important for carbon product selectivity.[16,17] Although there have been significant improvements in electrocatalytic CO_2RR, directing product formation to valuable high-order carbon species remains a critical challenge.

Morphological evolution of the catalyst during electrolysis significantly affects the catalytic behavior. For instance, Hsieh et al. revealed that the surface morphology of Ag nanocorals changed to a dendrite-like structure after 72 h of electrolysis, resulting in a 29% drop in CO current efficiency and attenuated total current density.[18] Grosse et al. monitored the dynamic morphological and chemical transformations of cube-shaped Cu nanoparticles on carbon substrate by operando electrochemical techniques. Drastic changes in the cubic morphology

were found to take place under CO_2RR conditions and were attributed to a decrease in selectivity for CO_2RR compared to HER.[19] On the other hand, surface restructuring can benefit the selectivity towards desired products. Scholten et al. showed that Cu dendrites supported on metal substrates underwent visible roughening with the formation of small particles. Their combined *in situ* and *operando* electrochemical analysis suggested that the high selectivity of dendritic Cu toward ethylene and ethanol is exclusively due to these dynamic morphological changes.[20] Kim et al. also found that dense Cu particle ensembles supported on carbon paper can lead to the formation of Cu nanocubes, which significantly benefited the selectivity toward C_2 and C_3 products.[21]

Herein, we examine the role of carbon modifier on metal surfaces for CO_2RR. Porous carbon materials are ubiquitously used to support metal particles and are often assumed to be innocent bystanders to the catalytic reactions. Our recent research challenged this notion by showing that the porosity of the carbon support can modulate the selectivity of CO_2RR on Cu particles.[9] It has also been demonstrated by other researchers that different types of carbon have varied effects on the reaction.[21–26] In the present study, we utilize a straightforward approach to examine the influence of carbon types on surface reconstruction of Cu foils under CO_2RR conditions. We demonstrate that a carbon layer can promote advantageous morphological transformations that lead to enhanced C_2 and C_3 product selectivity and activity. The structure of the porous carbon is also attributed

to differences in mass transport of protons and carbon dioxide to and from the electrode, ultimately enabling HER suppression.

3.2 Experimental Procedures

3.2.1 Synthesis of CA

Carbon aerogels were synthesized by the same procedure reported in our recent paper by using resorcinol and formaldehyde as precursors.[9] Reproduced here for clarity, resorcinol was stirred with formaldehyde by a 1:2 molar ratio to form a 5 wt % aqueous solution followed by the addition of varying concentrations of Na_2CO_3 as a base catalyst. The solution was left undisturbed for 48 hours at 30 °C, during which primary particles were formed and an orange solution was generated. The temperature was then increased to 60 °C for another 2 days.

After the gelation process, the wet gels were carefully removed from the container and soaked in reagent alcohol for 12 hours. This process was repeated with a fresh stock of reagent alcohol for another 12 hours. The wet gels were then soaked in dry ethanol for 6 hours on a gently shaking plate to facilitate the removal of residual water, which is necessary for critical point drying. This process was repeated 4 times. Finally, the wet gel was dried on a Tousimis 795 Critical Point Dryer. The copper-loaded RF aerogel was pyrolyzed at 1050 °C for 5 hours under N_2. The heating rate was 2.5 °C/minute.

3.2.2 Electrode Preparation

An ink slurry was prepared by dispersing 1.5 mg of carbon powders of CA or Vulcan XC72R(VXC) in 1 mL 1:4 (v/v) ethanol water solution. 100 μL 5 wt %

Nafion in water and 1-propanol were added as a binder. CA was ground to powders by shaking in a plastic vial with stainless steel balls. The electrode for electrolysis was prepared by drop-casting 200 μL catalytic ink on a 1 cm × 1 cm area of Cu foil electrode masked by Kapton tapes and allowed to dry under an infrared lamp, which facilitated the formation of a uniform thin film with good surface adhesion. Prior to drop-casting the ink, Cu foils were dipped in HCl acid briefly to remove the oxide layer. We tried to prepare CA-Ag and VXC-Ag electrode using the same method. However, upon conducting electrolysis, the carbon layer partially lifts off the surface owing to formation of large gas bubbles.

3.2.3 Controlled-Potential Electrolysis

The following procedures are reproduced from a previous publication for clarity.[1] The experiments were performed in a gas-tight two-compartment electrochemical cell (H-cell) separated by a glass frit with a working electrode and a Ag/AgCl reference electrode on one side and a Pt coil or graphite rod counter electrode. Each compartment was filled with 40 mL 0.1 M $KHCO_3$ electrolyte with a headspace volume of 30 mL. CO_2 gas was purged through both compartments for at least 15 min before electrolysis. Electrolysis were conducted for 2 h between -0.6 V to -1.05 V vs. RHE. The working compartment was directly connected to an Agilent 490 Micro GC to analyze gas products and gas injections were initiated every 30 min after 1 h of electrolysis. At least three freshly prepared electrodes were independently measured at each potential. The ohmic drop was measured by electrochemical impedance spectroscopy (EIS). The real resistance at 1 x 10^4

Hz on Nyquist plot was taken as the ohmic drop for the system and all potentials reported are IR compensated. The potential was converted to V vs. Reversible Hydrogen Electrode (RHE) by the following equation:

$$E\ (vs\ RHE) = E\ \left(vs \frac{Ag}{AgCl}\right) + 0.209\ V + 0.0591\ pH + R\ I$$

where the *pH* was 6.8, *R* is the solution resistance measured by EIS, and *I* is the average current during the electrolysis. Gas products were analyzed by the GC equipped with a thermal conductivity detector (TCD), a Molsieve 5Å column and a PoraPlot U (PPU) column. The Molsieve column was used to separate H_2, CO, and CH_4, while the PPU column was used to separate C_2H_4 and other hydrocarbons. Calibration curve was made for quantification by injecting standard amounts of each gas to the H-cell. Isotopic labeling experiments conducted on a GC-MS demonstrate carbon products are derived from CO_2 and additional control experiments are available. Liquid products were analyzed by a Bruker Advance 400 MHz FT-NMR spectrometer with dimethylsulfoxide (DMSO) as internal standard. Specifically, the sample was prepared by adding 0.5 mL of electrolyte and 0.1 mL D_2O with DMSO concentration 4.70 x 10^{-5} M. Solvent suppression method was used to obtain well-resolved spectra.

3.2.4 Cu Electrode Preparation with Removed Carbon Layer

Carbon layer was gently lifted by a piece of Kapton tape. Then the electrode was rinsed with deionized water. The minimal residue was cleaned gently with a Kimwipe. SEM and EDS were conducted to make sure full removal of carbon layer without changing the Cu surface structure.

3.3 Material Characterization and Electrode Preparation

Carbon aerogels are intriguing platforms to study interfacial processes owing to their tunable porosity, high conductivity, and robust mechanical properties.[27–29] Unlike commercial carbons, the facile synthesis of carbon aerogels does not use metal additives and allows for careful control of metal impurities. In a previous study, we used carbon aerogels as a substrate for Cu particle catalysts.[9] We demonstrated that the carbon porosity, which is tuned by the resorcinol to carbonate (R/C) ratio, has a significant effect on CO_2RR selectivity. In the present report, we utilized an R/C ratio of 180 to synthesize a highly porous and mechanically robust carbon aerogel (CA). As shown in Figure 1, the carbon structure is composed of small primary carbon particles (~9 nm) with interconnected pores (**Figure 3.1a**, **Figure B1a-c**). Nitrogen adsorption and desorption experiments show that the BET surface area of CA is 1409.6 $m^2\ g^{-1}$ (**Figure 3.1b**). Elemental characterization by XPS confirm that the as-synthesized CA is highly carbonized, containing less than 3% oxygen species and showing no detectable signals from other elements (**Table B1**, **Figure B2**).

To probe the effect of carbon hierarchical structure on the electrode-electrolyte interface, Vulcan XC 72R (VXC) is also studied as a carbon modifier. VXC is a widely used commercial carbon support for fuel cells and other catalysts, owing to its low cost, relatively high surface area, and chemical purity. VXC primary particles are large (> 50 nm) and the structure has significantly less void space compared to CA (**Figure 3.1c**, **Figure B1d-f**). The lower gas adsorption and

smaller hysteresis in the nitrogen adsorption and desorption experiments clearly illustrate that VXC is less porous than CA with a BET surface area of 232.7 m^2 g^{-1} (**Figure 3.1b**). BJH modeling of the gas isotherms reveals that the pore size range of VXC is centered at 70 nm, whereas there is a broad distribution of pore sizes centered at 40 nm in CA (**Figure 3.1d**). The higher BET surface area and the wide range of pore diameters of CA result from the presence of interconnected channels in the aerogel structure. XPS characterization show that VXC is more oxygenated compared to CA with an oxygen content of 9.8% (**Table B1**, **Figure B2**).

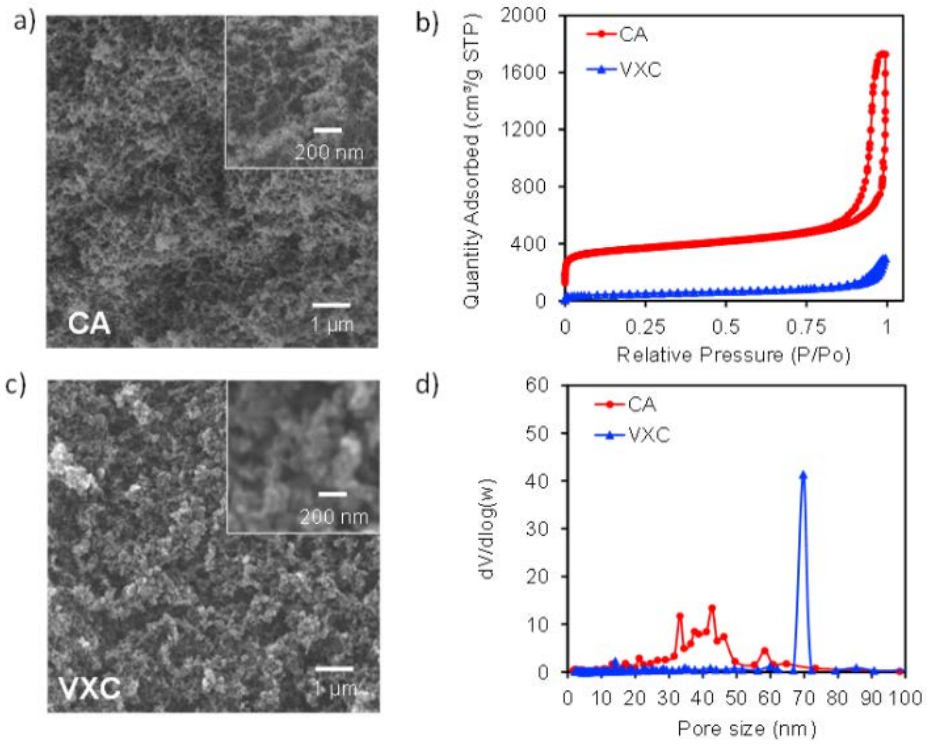

Figure 3.1. SEM images of (a) CA and (c) VXC supports, and (b) nitrogen isotherms and (d) DFT-calculated pore size distribution of CA (red circles) and VXC (blue triangles).

3.4 Electrocatalytic CO_2 Reduction

Electrodes are prepared by dropcasting an ink composed of 1.5 g L^{-1} carbon and 0.5 wt. % Nafion on copper foils. BET analysis of the dried CA ink shows that a high surface area (854 m^2/g) is retained even with the addition of Nafion (**Figure B3**). Linear sweep voltammetry (LSV) is conducted using the carbon-modified Cu electrodes both under Ar and CO_2 (**Figure B4**). There is a decrease in the current density under CO_2 because adsorbed CO can inhibit the HER reaction.[30] Controlled potential electrolysis are conducted at various potentials in CO_2-saturated 0.1 M $KHCO_3$ and the products are quantified by gas chromatography and ^1H nuclear magnetic resonance spectroscopy. Current density is plotted for C_1 and $C_{2,3}$ products separately in **Figure 3.2** to show the distinct trends for product formation. While both CA-modified (CA-Cu) and VXC-modified Cu (VXC-Cu) generate mostly C_1 products at low cathodic potentials, CA-Cu begins to form significant amounts of C_2 and C_3 products at a lower overpotential than VXC-Cu. For instance, ethylene current density of 1.0 mA cm^{-1} is observed at -0.92 vs. RHE for CA-Cu, whereas a more cathodic potential of -0.98 V is needed for the same ethylene current density on VXC-Cu (blue traces, **Figure 3.2a,b**). In addition, the ethanol current density doubles for CA-Cu compared to VXC-Cu at the same potential. However, current density of C_1 product shows an opposite trend at overpotentials more negative than -0.9 V. At these more cathodic potentials, VXC-Cu is better at generating C_1 products, particularly methane, than CA-Cu. Isotopic labeling demonstrates that all carbon products are derived from $^{13}CO_2$ and not from

the degradation of the carbon layer (**Table B2**). As we have previously reported, a controlled potential electrolysis using CA modified glassy carbon electrode yields negligible carbon products.[9]

In contrast, the pristine Cu foil displays dramatically different catalytic behavior.[3,31] C-C coupled products are not detected until -0.92 V (**Figure 3.2c**). The overall CO_2RR current density is significantly attenuated compared to CA-Cu and VXC-Cu, illustrating that the carbon modifiers are not passivating the metallic surface (**Figure 3.2c**). In a control experiment, the nafion-only modified Cu does not show high selectivity for C_{2-3} product formation (Figure B5). Our results suggest that the carbon layers are effective at altering the catalytic activity of the Cu electrode.

The enhanced C_{2-3} product selectivity of carbon-modified Cu electrodes is also confirmed by calculating the Faradaic efficiency. **Figure 3.3a** reveals a clear trend for increasing C_{2-3} product selectivity in the order of CA-Cu > VXC-Cu > Cu foil. Notably, ~45% selectivity for C_{2-3} products is achieved for CA-Cu at -0.98 V with a high efficiency towards ethylene and ethanol production (**Figure 3.3a**). In contrast, both VXC-Cu and Cu foil predominantly form C_1 products at -0.92 and -0.98 V (**Figure 3.3b,c**). The differences in selectivity of CA-Cu and VXC-Cu become less noticeable at the most cathodic potential tested, -1.04 V (**Figure 3.3d**).

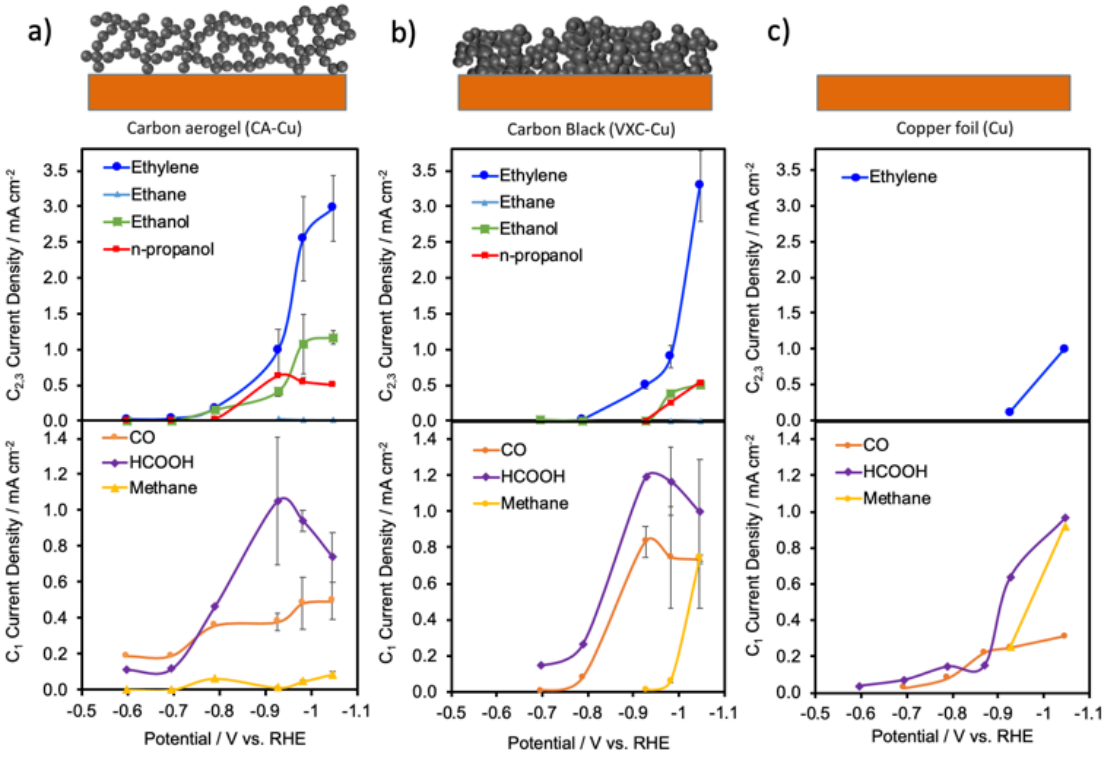

Figure 3.2. Partial current density for (a) CA-Cu, (b) VXC-Cu, and (c) Cu foil. Conditions: CO_2-saturated 0.1 M $KHCO_3$, pH 6.8

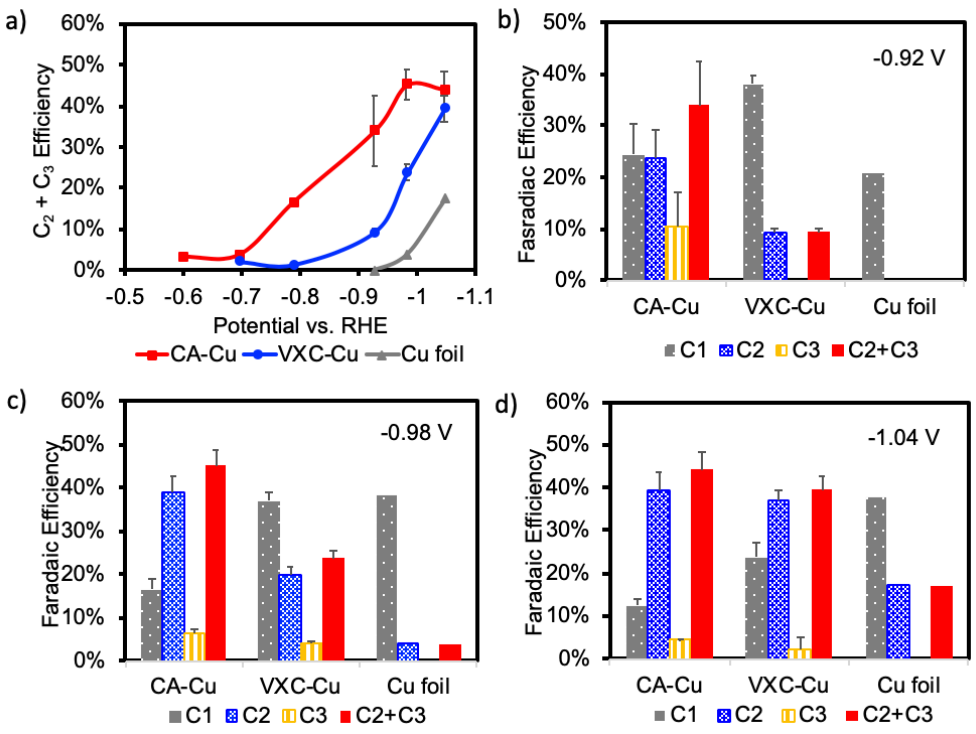

Figure 3.3. (a) Faradaic efficiency C_2 and C_3 products for CA-Cu, VXC-Cu, and Cu foil. Comparison of C_1, C_2, and C_3 product selectivity at (b) -0.92 V, (c) -0.98 V, and (d) -1.04 V vs. RHE. CA-Cu showed the highest selectivity for C_2 and C_3 formation. Conditions: CO_2-saturated 0.1 M $KHCO_3$, pH 6.8

Post-electrolysis characterization of the Cu foil is conducted to understand the enhanced product selectivity of carbon modified Cu foils. SEM images and cross-sectional analysis show that the electrode surface remains covered by the dropcasted carbon modifier with some non-uniformity in thickness (**Figure B6a,d**). The cross-section view of the electrode shows both CA and VXC layers are of similar thickness of ~10 μm. (**Figure B6b,e**). To evaluate the surface morphology, the carbon layer is gently peeled away from the metal foil after electrolysis and both interfaces are imaged by SEM. **Figure 3.4** shows that the Cu surface undergoes dynamic changes during the 8-h time electrolysis. After the first 2 h at a potential of -0.98 V, pitting and particle formation are observed on the metal

surface of CA-Cu (**Figure 3.4**, top). After an 8-h electrolysis, the Cu particles become more faceted and resemble cubic prisms. By comparison, VXC-Cu only shows pitting and very few particles on the metal surface (**Figure 3.4**, bottom), while bare Cu foil essentially shows no morphological change after a 2-h electrolysis (**Figure B7**). Surface roughness quantification of the Cu foil after removing the carbon modifiers is accomplished by capacitance measurement. Consistent with SEM images, the CA-Cu:VXC-Cu:Cu roughness ratio is 22 : 9 : 1 after a 2-h electrolysis at -0.98 V (**Figure B8**).

Accordingly, the CO_2RR activity of CA-Cu and VXC-Cu is monitored during the 8-h electrolysis. For CA-Cu, the total current density decreases over the first 5 h due to HER suppression (**Figure B9a**). The specific current density for ethylene in the first 3 h increases while the generation of CO decreases. A notable increase in ethanol formation occurred during the course of 8 h. Formations of the other major products, namely HCO_2H, methane, ethane, and n-propanol are relatively constant. Similar HER suppression is seen in the case of VXC-Cu, though the specific current densities for CO_2RR products remain relatively unchanged over 8 hours (**Figure B9b**). The increase in C-C product formation in CA-Cu suggests the presence of new active sites on the Cu surface.

The Cu surface morphology is also examined as a function of potential in CA-Cu and VXC-Cu. Roughening of the surface is seen at the onset of C_{2-3} production at -0.79 V for CA-Cu. The density of Cu particles and the surface pitting increase with more cathodic potentials (**Figure B10**) where C_{2-3} formation is

increasingly favored. In the case of VXC-Cu, pitting is observed at -0.92 and -0.98 V with negligible particle formation. However, in addition to pitting, small particles are detected at -1.04 V, which also coincides with high C_2 and C_3 production. These results show that pitting and particle deposition in the presence of VXC and CA lead to higher C_2 and C_3 yields, whereas surface pitting alone in the presence of VXC shows limited enhancement for C_{2-3}. We note that pitting on Cu surfaces has been previously observed in $NaHCO_3$ solutions, but only at potentials anodic to 0.020 V vs. Ag/AgCl.[32] Our observation occurs at much more cathodic potentials (< -0.79 V), which suggests a different mechanism is at play.

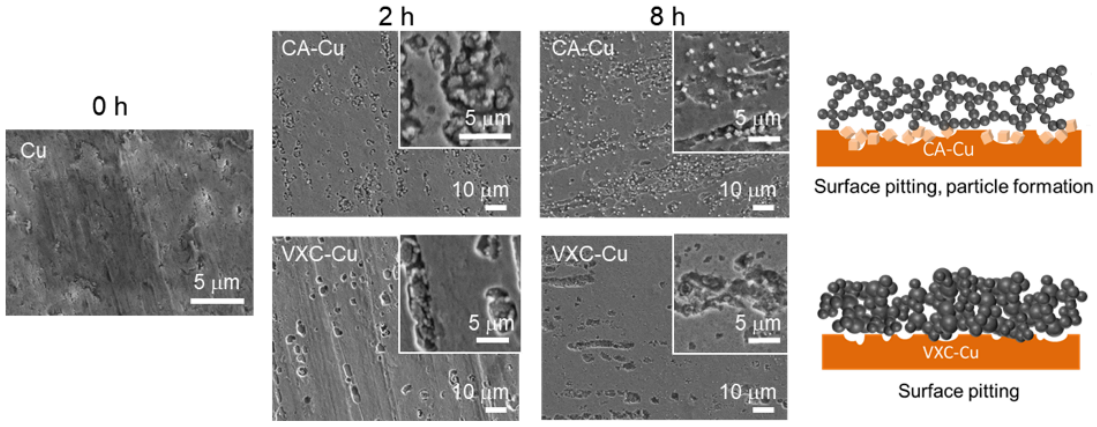

Figure 3.4. SEM images of the Cu foil before electrolysis (left), and the Cu foil upon removing the CA or VXC layer after a 2- (middle) and 8-h (right) electrolysis at -0.98 V vs RHE, showing major surface reconstruction. Conditions: CO_2-saturated 0.1 M $KHCO_3$, pH 6.8

3.5 Post Electrolysis Analysis

The Cu-carbon interface is further studied by imaging the removed carbon layer. Cu particles can only be seen in the area contacted with Cu foil, which suggests Cu redeposition is confined at the interface of carbon layer and Cu. (**Figure B11**) XPS on the same carbon samples correspondingly shows weak Cu signals confirming the presence of a Cu(0) or Cu(I) species (**Figure B12**). Cross-sectional SEM images and EDS linear scans show that the Cu signal diminishes away from the interface, further validating that Cu deposition does not penetrate into the carbon layer (**Figure B6c,f**). This is likely due to that Nafion is a poor conductor of heavy metal cations, so it prevents Cu ions from penetrating the carbon layer and facilitates redeposition of Cu particles at the interface.[33]

Our results imply that C_{2-3} selectivity is highly correlated with surface reconstruction. This observation is consistent with previous reports that increased surface roughness induces local alkalization and suppresses H_2 and CH_4 generation.[20,34,35] Moreover, the higher density of faceted particles in CA-Cu compared to VXC-Cu at all potentials (**Figure B10**) suggests that exposed faces on the particles may play a role in lowering the overpotential for C_2 and C_3 formation.[36–38] The particles may contribute to improved exposure of Cu(100) facets, which is shown to be more active than other facets for C_2 product formation.[37] Higher density of particles also benefit the presence of active edge sites and the restructuring process increases the possibility to involve more oxygen impurities, which both favor C-C coupling reaction.[36,38] It has been shown

previously that an alkaline environment can encourage copper corrosion to Cu_2O,[39–41] which can subsequently lead to Cu redeposition during the reduction of CO_2. In our materials, the high porosity in CA may lead to the local pH increase and promote the roughening effect. Current investigations are focused on understanding why carbon aerogels are more efficient at promoting the formation of Cu particles under electrocatalytic conditions.

To evaluate the role of carbon modifiers on the local pH, a 2-h electrolysis is conducted on the roughened Cu electrodes after gently removing the carbon layer. For both CA-Cu and VXC-Cu, removal of the carbon modifier leads to an increase in H_2 current density and a decreased selectivity for C_2 and C_3 products (**Figure B13**). The losses in CO_2RR selectivity and activity are more dramatic in the case of VXC-Cu, where the absence of the carbon layer results predominantly in H_2 generation. This finding supports that the carbon layer helps maintain a high local pH that in turn suppresses HER and promotes C_{2-3} generation. We have previously reported that there is an optimal carbon porosity for balancing an alkaline pH and rapid CO_2 diffusion to the catalyst surface.[9] In the present study, variations in the structure and porosity of CA and VXC may also contribute to the different catalytic behavior of CA-Cu and VXC-Cu. These results also suggest that surface pitting alone on the Cu foil does not lead to significantly enhanced selectivity for CO_2 reduction, whereas particle redeposition on the Cu foil has a more dramatic impact on carbon product formation.

In addition, efficient CO_2 transport to the surface can lead to higher local concentrations of activated Cu-CO surface species and greater selectivity towards high-order products at lower overpotentials.[42] Recent studies illustrated that hydrophobicity can impact local CO_2 concentrations.[16,17] Wakerley et al. postulated that hydrophobic Cu surface can trap gases to increase the concentration of CO_2 at the interface, thus enhancing CO_2RR selectivity.[17] In order to compare the hydrophobicity of CA-Cu and VXC-Cu, the contact angle is measured on both surfaces. Contact angles of 92.5° and 68.0° are obtained for CA-Cu and VXC-Cu, respectively, clearly demonstrating that CA-Cu has a more hydrophobic surface than VXC-Cu (**Figure B14**). We postulate that the more hydrophobic channels in carbon aerogel may facilitate CO_2 transport to the Cu-carbon interface, further contributing to the enhanced selectivity of C_2 and C_3 products of CA-Cu.

Our work utilizes carbon materials as modifiers to the Cu surface and reaches C_{2-3} Faradaic efficiency of 45% at -0.98 V on CA-Cu. This is superior to most of the recent reports of Cu surface modification to enhance C_{2-3} selectivity for CO_2RR in terms of selectivity at a relatively low overpotential as well as the abundance of carbon materials compared to the noble metals and synthesized organic compounds used in other reports (**Table B3**). Our work is the first study on utilizing carbon to modulate the Cu surface and provides new insights into the role of local environment and surface structure on Cu for CO_2RR.

3.6 Conclusions

In summary, we have demonstrated a strategy to use porous carbons as surface modifiers to tune the electrocatalytic behavior of Cu foils for CO_2RR. Our findings suggest that the improvement of selectivity and activity results from the dual roles of the carbon modifier. On one hand, the carbon modifiers contribute to surface reconstruction of the Cu foil electrode. Significant surface roughening was observed in both CA-Cu and VXC-Cu, but the nature of the morphological changes was different. The CA led to the formation of distinct particles on Cu surface, which were prone to evolve into faceted particles under long-term electrolysis. In contrast, VXC-Cu showed pitting on the Cu surface at similar potentials. These morphological transformations are correlated with more selective CO_2RR. On the other hand, the structure, porosity, and hydrophobicity of the carbon layers on Cu can influence the local pH and CO_2 concentration at the surface of the Cu electrode, further enhancing high-order carbon production. Our results highlight that carbon materials can alter the morphology of the metal surface and play an underexplored role in directing product formation. Importantly, these findings invite a more careful evaluation of carbon-supported metal catalysts, where small surface changes can lead to dramatic differences in catalytic performance.

3.7 References

(1) Reske, R.; Mistry, H.; Behafarid, F.; Roldan Cuenya, B.; Strasser, P. Particle Size Effects in the Catalytic Electroreduction of CO_2 on Cu Nanoparticles. *J. Am. Chem. Soc.* **2014**, *136* (19), 6978–6986.

https://doi.org/10.1021/ja500328k.

(2) Sen, S.; Liu, D.; Palmore, G. T. R. Electrochemical Reduction of CO_2 at Copper Nanofoams. *ACS Catal.* **2014**, *4* (9), 3091–3095. https://doi.org/10.1021/cs500522g.

(3) Raciti, D.; Livi, K. J.; Wang, C. Highly Dense Cu Nanowires for Low-Overpotential CO_2 Reduction. *Nano Lett.* **2015**, *15*, 6829–6835. https://doi.org/10.1021/acs.nanolett.5b03298.

(4) Medina-Ramos, J.; Zhang, W.; Yoon, K.; Bai, P.; Chemburkar, A.; Tang, W.; Atifi, A.; Lee, S. S.; Fister, T. T.; Ingram, B. J.; et al. Cathodic Corrosion at the Bismuth-Ionic Liquid Electrolyte Interface under Conditions for CO_2 Reduction. *Chem. Mater.* **2018**, *30* (7), 2362–2373. https://doi.org/10.1021/acs.chemmater.8b00050.

(5) Shen, S.; Peng, X.; Song, L.; Qiu, Y.; Li, C.; Zhuo, L.; He, J.; Ren, J.; Liu, X.; Luo, J. AuCu Alloy Nanoparticle Embedded Cu Submicrocone Arrays for Selective Conversion of CO_2 to Ethanol. *Small* **2019**, *15* (37), 1902229. https://doi.org/10.1002/smll.201902229.

(6) Mi, Y.; Peng, X.; Liu, X.; Luo, J. Selective Formation of C_2 Products from Electrochemical CO_2 Reduction over $Cu_{1.8}Se$ Nanowires. *ACS Appl. Energy Mater.* **2018**. https://doi.org/10.1021/acsaem.8b00744.

(7) Li, C. W.; Kanan, M. W. CO_2 Reduction at Low Overpotential on Cu Electrodes Resulting from the Reduction of Thick Cu_2O Films. *J. Am. Chem. Soc.* **2012**, *134* (17), 7231–7234. https://doi.org/10.1021/ja3010978.

(8) Billy, J. T.; Co, A. C. Reducing the Onset Potential of CO_2 Electroreduction on CuRu Bimetallic Particles. *Appl. Catal. B Environ.* **2018**, *237*, 911–918. https://doi.org/10.1016/j.apcatb.2018.06.072.

(9) Han, X.; Wang, M.; Le, M. L.; Bedford, N. M.; Woehl, T. J.; Thoi, V. S. Effects of Substrate Porosity in Carbon Aerogel Supported Copper for Electrocatalytic Carbon Dioxide Reduction. *Electrochim. Acta* **2019**, *297*, 545–552. https://doi.org/10.1016/j.electacta.2018.11.203.

(10) Banerjee, S.; Han, X.; Thoi, V. S. Modulating the Electrode-Electrolyte Interface with Cationic Surfactants in Carbon Dioxide Reduction. *ACS Catal.* **2019**, *9* (6), 5631–5637. https://doi.org/10.1021/acscatal.9b00449.

(11) Atifi, A.; Boyce, D. W.; DiMeglio, J. L.; Rosenthal, J. Directing the Outcome of CO_2 Reduction at Bismuth Cathodes Using Varied Ionic Liquid Promoters. *ACS Catal.* **2018**, *8* (4), 2857–2863. https://doi.org/10.1021/acscatal.7b03433.

(12) Huo, Y.; Peng, X.; Liu, X.; Li, H.; Luo, J. High Selectivity Toward C_2H_4 Production over Cu Particles Supported by Butterfly-Wing-Derived Carbon Frameworks. *ACS Appl. Mater. Interfaces* **2018**. https://doi.org/10.1021/acsami.7b19423.

(13) Han, Z.; Kortlever, R.; Chen, H. Y.; Peters, J. C.; Agapie, T. CO_2 Reduction Selective for C≥2 Products on Polycrystalline Copper with N-Substituted Pyridinium Additives. *ACS Cent. Sci.* **2017**, *3* (8), 853–859. https://doi.org/10.1021/acscentsci.7b00180.

(14) Ahn, S.; Klyukin, K.; Wakeham, R. J.; Rudd, J. A.; Lewis, A. R.; Alexander, S.; Carla, F.; Alexandrov, V.; Andreoli, E. Poly-Amide Modified Copper Foam Electrodes for Enhanced Electrochemical Reduction of Carbon Dioxide. *ACS Catal.* **2018**, *8* (5), 4132–4142. https://doi.org/10.1021/acscatal.7b04347.

(15) Xie, M. S.; Xia, B. Y.; Li, Y.; Yan, Y.; Yang, Y.; Sun, Q.; Chan, S. H.; Fisher, A.; Wang, X. Amino Acid Modified Copper Electrodes for the Enhanced Selective Electroreduction of Carbon Dioxide towards Hydrocarbons. *Energy Environ. Sci.* **2016**, *9* (5), 1687–1695. https://doi.org/10.1039/C5EE03694A.

(16) Buckley, A. K.; Lee, M.; Cheng, T.; Kazantsev, R. V.; Larson, D. M.; Goddard, W. A.; Toste, F. D.; Toma, F. M. Electrocatalysis at Organic-Metal Interfaces: Identification of Structure-Reactivity Relationships for CO_2 Reduction at Modified Cu Surfaces. *J. Am. Chem. Soc.* **2019**, *141* (18), 7355–7364. https://doi.org/10.1021/jacs.8b13655.

(17) Wakerley, D.; Lamaison, S.; Ozanam, F.; Menguy, N.; Mercier, D.; Marcus, P.; Fontecave, M.; Mougel, V. Bio-Inspired Hydrophobicity Promotes CO_2 Reduction on a Cu Surface. *Nat. Mater.* **2019**, *18* (11), 1222–1227. https://doi.org/10.1038/s41563-019-0445-x.

(18) Hsieh, Y.-C.; Senanayake, S. D.; Zhang, Y.; Xu, W.; Polyansky, D. E. Effect of Chloride Anions on the Synthesis and Enhanced Catalytic Activity of Silver Nanocoral Electrodes for CO_2 Electroreduction. *ACS Catal.* **2015**,

5, 5349–5356. https://doi.org/10.1021/acscatal.5b01235.

(19) Grosse, P.; Gao, D.; Scholten, F.; Sinev, I.; Mistry, H.; Roldan Cuenya, B. Dynamic Changes in the Structure, Chemical State and Catalytic Selectivity of Cu Nanocubes during CO_2 Electroreduction: Size and Support Effects. *Angew. Chemie - Int. Ed.* **2018**, *57* (21), 6192–6197. https://doi.org/10.1002/anie.201802083.

(20) Scholten, F.; Sinev, I.; Bernal, M.; Cuenya, B. R. Plasma-Modified Dendritic Cu Catalyst for CO_2 Electroreduction. *ACS Catal.* **2019**, *9* (I), 5496–5502. https://doi.org/10.1021/acscatal.9b00483.

(21) Kim, D.; Kley, C. S.; Li, Y.; Yang, P. Copper Nanoparticle Ensembles for Selective Electroreduction of CO_2 to C_2–C_3 Products. *Proc. Natl. Acad. Sci. U. S. A.* **2017**, *114* (40), 10560–10565. https://doi.org/10.1073/pnas.1711493114.

(22) Geioushy, R. A.; Khaled, M. M.; Alhooshani, K.; Hakeem, A. S.; Rinaldi, A. Graphene/ZnO/Cu_2O Electrocatalyst for Selective Conversion of CO_2 into n-Propanol. *Electrochim. Acta* **2017**, *245*, 456–462. https://doi.org/10.1016/j.electacta.2017.05.185.

(23) Pan, F.; Zhao, H.; Deng, W.; Feng, X.; Li, Y. A Novel N,Fe-Decorated Carbon Nanotube/Carbon Nanosheet Architecture for Efficient CO_2 reduction. *Electrochim. Acta* **2018**, *273*, 154–161. https://doi.org/10.1016/j.electacta.2018.04.047.

(24) Lum, Y.; Kwon, Y.; Lobaccaro, P.; Chen, L.; Clark, E. L.; Bell, A. T.; Ager,

J. W. Trace Levels of Copper in Carbon Materials Show Significant Electrochemical CO_2 Reduction Activity SI. *ACS Catal.* **2015**, 202–209. https://doi.org/10.1021/acscatal.5b02399.

(25) Baturina, O. A.; Lu, Q.; Padilla, M. A.; Xin, L.; Li, W.; Serov, A.; Artyushkova, K.; Atanassov, P.; Xu, F.; Epshteyn, A.; et al. CO_2 Electroreduction to Hydrocarbons on Carbon-Supported Cu Nanoparticles. *ACS Catal.* **2014**, *4* (10), 3682–3695. https://doi.org/10.1021/cs500537y.

(26) Dinh, C. T.; Burdyny, T.; Kibria, G.; Seifitokaldani, A.; Gabardo, C. M.; Pelayo García De Arquer, F.; Kiani, A.; Edwards, J. P.; De Luna, P.; Bushuyev, O. S.; et al. CO_2 Electroreduction to Ethylene via Hydroxide-Mediated Copper Catalysis at an Abrupt Interface. *Science* **2018**, *360* (6390), 783–787. https://doi.org/10.1126/science.aas9100.

(27) Pekala, R. W.; Schaefer, D. W. Structure of Organic Aerogels. 1. Morphology and Scaling. *Macromolecules* **1993**, *26* (20), 5487–5493. https://doi.org/10.1021/ma00072a029.

(28) Biener, J.; Stadermann, M.; Suss, M.; Worsley, M. a.; Biener, M. M.; Rose, K. a.; Baumann, T. F. Advanced Carbon Aerogels for Energy Applications. *Energy Environ. Sci.* **2011**, *4* (3), 656–667. https://doi.org/10.1039/c0ee00627k.

(29) Elkhatat, A. M.; Al-Muhtaseb, S. A. Advances in Tailoring Resorcinol-Formaldehyde Organic and Carbon Gels. *Adv. Mater.* **2011**, *23* (26), 2887–2903. https://doi.org/10.1002/adma.201100283.

(30) Lee, S.; Park, G.; Lee, J. Importance of Ag-Cu Biphasic Boundaries for Selective Electrochemical Reduction of CO_2 to Ethanol. *ACS Catal.* **2017**, *7* (12), 8594-8604. https://doi.org/10.1021/acscatal.7b02822.

(31) Peng, Y.; Wu, T.; Sun, L.; Nsanzimana, J. M. V.; Fisher, A. C.; Wang, X. Selective Electrochemical Reduction of CO_2 to Ethylene on Nanopores-Modified Copper Electrodes in Aqueous Solution. *ACS Appl. Mater. Interfaces* **2017**, *9* (38), 32782-32789). https://doi.org/10.1021/acsami.7b10421.

(32) Li, J.; Lampner, D. In-Situ AFM Study of Pitting Corrosion of Cu Thin Films. In *Colloids and Surfaces A: Physicochemical and Engineering Aspects* **1999**, *154*, 227–237. https://doi.org/10.1016/S0927-7757(98)00901-7.

(33) Hongsirikarn, K.; Goodwin, J. G.; Greenway, S.; Creager, S. Effect of Cations (Na^+, Ca^{2+}, Fe^{3+}) on the Conductivity of a Nafion Membrane. *J. Power Sources* **2010**, *195* (21), 7213–7220. https://doi.org/10.1016/j.jpowsour.2010.05.005.

(34) De Luna, P.; Quintero-Bermudez, R.; DInh, C. T.; Ross, M. B.; Bushuyev, O. S.; Todorović, P.; Regier, T.; Kelley, S. O.; Yang, P.; Sargent, E. H. Catalyst Electro-Redeposition Controls Morphology and Oxidation State for Selective Carbon Dioxide Reduction. *Nat. Catal.* **2018**, *1* (2), 103–110. https://doi.org/10.1038/s41929-017-0018-9.

(35) Klingan, K.; Kottakkat, T.; Jovanov, Z. P.; Jiang, S.; Pasquini, C.; Scholten, F.; Kubella, P.; Bergmann, A.; Roldan Cuenya, B.; Roth, C.; et al.

Reactivity Determinants in Electrodeposited Cu Foams for Electrochemical CO_2 Reduction. *ChemSusChem* **2018**, *11* (19), 3449–3459. https://doi.org/10.1002/cssc.201801582.

(36) Loiudice, A.; Lobaccaro, P.; Kamali, E. A.; Thao, T.; Huang, B. H.; Ager, J. W.; Buonsanti, R. Tailoring Copper Nanocrystals towards C_2 Products in Electrochemical CO_2 Reduction. *Angew. Chemie - Int. Ed.* **2016**, *55* (19), 5789–5792. https://doi.org/10.1002/anie.201601582.

(37) Hahn, C.; Hatsukade, T.; Kim, Y.-G.; Vailionis, A.; Baricuatro, J. H.; Higgins, D. C.; Nitopi, S. A.; Soriaga, M. P.; Jaramillo, T. F. Engineering Cu Surfaces for the Electrocatalytic Conversion of CO_2 : Controlling Selectivity toward Oxygenates and Hydrocarbons. *Proc. Natl. Acad. Sci.* **2017**, *114* (23), 5918–5923. https://doi.org/10.1073/pnas.1618935114.

(38) Gao, D.; Zegkinoglou, I.; Divins, N. J.; Scholten, F.; Sinev, I.; Grosse, P.; Roldan Cuenya, B. Plasma-Activated Copper Nanocube Catalysts for Efficient Carbon Dioxide Electroreduction to Hydrocarbons and Alcohols. *ACS Nano* **2017**, *11* (5), 4825–4831. https://doi.org/10.1021/acsnano.7b01257.

(39) Souto, R. M.; Sánchez, M. P.; Barrera, M.; González, S.; Salvarezza, R. C.; Arvia, A. J. The Kinetics of Pitting Corrosion of Copper in Alkaline Solutions Containing Sodium Perchlorate. *Electrochim. Acta* **1992**, *37* (8), 1437–1443. https://doi.org/10.1016/0013-4686(92)87019-V.

(40) Souto, R. M.; González, S.; Salvarezza, R. C.; Arvia, A. J. Kinetics of

Copper Passivation and Pitting Corrosion in Na_2SO_4 Containing Dilute NaOH Aqueous Solution. *Electrochim. Acta* **1994**, *39* (17), 2619–2628. https://doi.org/10.1016/0013-4686(94)00204-5.

(41) Feng, Y.; Siow, K. S.; Teo, W. K.; Tan, K. L.; Hsieh, A. K. Corrosion Mechanisms and Products of Copper in Aqueous Solutions at Various PH Values. *Corrosion* **1997**, *53* (5), 389–398. https://doi.org/10.5006/1.3280482.

(42) Yang, K. D.; Ko, W. R.; Lee, J. H.; Kim, S. J.; Lee, H.; Lee, M. H.; Nam, K. T. Morphology-Directed Selective Production of Ethylene or Ethane from CO_2 on a Cu Mesopore Electrode. *Angew. Chemie Int. Ed.* **2016**, 796–800. https://doi.org/10.1002/anie.201610432.

Chapter 4: Strategic Design of MoO_2 Nanoparticles Supported by Carbon Nanowires for Enhanced Electrocatalytic Nitrogen Reduction

The work encompassed in this chapter has been published with the following citation and listed authors:

ACS Energy Lett. **2020**, 5, XXX, 3237–3243.

Xu Han[1]*, Carter S. Gerke[1]*, Soumyodip Banerjee[1], Muhammad Zubair[3], Junjie Jiang[3], Nicholas M. Bedford[3], Elisa M. Miller[4], V. Sara Thoi[1,2]+

[1]Department of Chemistry, Johns Hopkins University, Baltimore, Maryland 21218, United States

[2]Department of Materials Science and Engineering, Johns Hopkins University, Baltimore, Maryland 21218, United States

[3]School of Chemical Engineering, University of New South Wales, Sydney, New South Wales 2052, Australia

[4]Chemistry and Nanoscience Center, National Renewable Energy Laboratory, Golden, Colorado 80204, United States

* Co-first authors

Additional data on materials characterization, electrolysis results and comparison to recent reports are provided in Appendix C.

4.1 Introduction

Ammonia (NH_3) is one of the most widely synthesized molecules in the chemical industry and plays a key role in the development of medications, fertilizers, and plastics with emerging applications as a carbon-neutral fuel source.[1–4] The traditional route for synthesizing NH_3 at industrial scales is the energy intensive Haber-Bosch (HB) process, which relies on extreme temperatures (~700 K) and pressures (~100 atm) to reduce molecular nitrogen.[5] Additionally, the HB process requires high purity hydrogen produced from the steam reformation of fossil fuels, which results in over 1% of global CO_2 emissions.[6] There exists a palpable need for developing a carbon-neutral synthetic pathway capable of reducing the formidable N-N triple bond with high activity and selectivity. Research in the electrocatalytic nitrogen reduction reaction (NRR) has accelerated in recent years with exploration of noble metals,[7,8] non-noble transition metals,[9,10] and non-metal systems.[11,12] Although impressive results have been found using noble metal catalysts and extreme reaction conditions,[13] the need for developing a catalytic system that is industrially processable at ambient temperatures and pressures is necessary to displace the HB process.

Molybdenum species have been critically examined for NRR owing to its role in the nitrogenase FeMoco active site.[14] Density functional theory (DFT) simulations have been performed for a Mo surface showing that Mo is uniquely suited for NRR because it is capable of enabling the chemisorption of nitrogen,

selective stabilization of the N_2H^* intermediate and destabilization of NH_2^*.[15] Numerous accounts on synthesizing and testing Mo-based electrocatalysts for NRR have surfaced in recent years, including Mo/Mo_xC, MoN, MoS_2, MoO_3, Mo_2N, Mo foil, Mo_2C, and atomically dispersed Mo.[9,16–22] Distinctive trends can be observed in recent literature relating to catalyst design for electrocatalytic nitrogen reduction. Different techniques have been used to suppress hydrogen adsorption to the surface of the catalyst, such as introducing strain induced defects[23–25] or by engineering surface vacancies.[26–32] By exploiting these surface states, the electronic structure of a material can be tuned to lower the energy barrier for binding nitrogen. Furthermore, it has been shown that these defect-rich nanomaterials can be chemically stabilized and energetically coupled to conductive carbon-based supports to further enhance catalytic activity.[33–35] Conductive carbonaceous supports can serve two major roles during electrolysis: 1) enhance the electrical contact to the current collector, effectively improving electron transport to the active sites and 2) prevent agglomeration of the nanoscale materials by providing a scaffold that allows for high particle dispersity.[36]

4.2 Experimental Procedures

4.2.1 Synthesis of Anilinium Molybdate Nanowires

1.24 g of ammonium molybdate tetrahydrate [$(NH_4)_6Mo_7O_{24}\cdot 4H_2O$] was dissolved in 40 mL of Millipore water in a 100 mL round bottom flask. To this solution, 1.6 g of aniline was added dropwise. Subsequently, 1.0 M HCl was added to the resulting mixture dropwise and the pH was monitored. At a pH ~4.0, a white

suspension was observed. The solution was further acidified to pH = 3.0 and heated at 60 ^{o}C for 5 h. The precipitate was collected via vacuum filtration and washed with water (x3) and finally ethanol (x1). The powder was dried in an oven overnight at 60 ^{o}C.

4.2.2 Synthesis of MoO_2/C nanowires

Approximately 1.0 g of the anilinium molybdate nanowires was placed into a ceramic crucible and transferred to a tube furnace. The system was flushed with Ar gas for 30 min and the sample was heated at a ramp rate of 2.5 ^{o}C/min to a final temperature of 650 ^{o}C, which was maintained for 5 h and then allowed to cool back to room temperature under a flow of Ar. The obtained black powder was then washed with 0.1 M HCl to remove adsorbed nitrogen species (x2) followed by Millipore water (x3) and dried in an oven at 60 ^{o}C overnight.

4.2.3 Electrochemistry preparation and analysis

To prepare the working electrode, 5.0 mg of the MoO_2 NW catalyst was suspended in 1.8 mL Millipore water and 0.2 mL Nafion (5.0 % w/w solution in water and 1-propanol) solution. The resulting suspension was sonicated for 30 min to ensure homogeneity. 40.0 µL of the ink solution was drop-casted onto a polyimide masked carbon paper electrode (exposed surface area = 1.0 cm^2) and dried under an IR lamp.

A 25 mL two-compartment H-cell with a glass frit joining was used for all electrochemical measurements. The carbon paper working electrode, an aqueous Ag/AgCl reference electrode and a stirring bar were added to the cathodic

compartment of the H-cell, containing 10 mL of electrolyte (0.1 M HCl, pH = 1.0). To the anode compartment was added 10 mL of electrolyte and a graphite counter electrode. A continuous stream of N_2 gas was bubbled first through a 0.1 M HCl acid trap to remove nitrogenous contaminants and then flowed into both compartments of the H-cell at a flow rate ranging between 20-30 cm^3 min^{-1}. Three separate electrolysis were conducted at four different potentials: -0.4, -0.3, -0.2, -0.1 V vs. RHE. All potentials were converted to RHE by, E (RHE) = E (Ag/AgCl) + 0.059 × pH + 0.197 (V).

NH_3 was detected following a modified indophenol blue method and was analyzed via UV-Vis Spectroscopy. Three separate indicator solutions were freshly prepared: (1) 0.4 g NaOH, 0.5 g salicylic acid, and 0.5 g sodium citrate in 10 mL water; (2) 0.305 mL NaClO in 10 mL water; (3) 0.1 g sodium nitroferricyanide hydrate in 10 mL. Sample detection was performed by adding 1 mL of solution from the cathode side of the cell followed by 1 mL of (1), 0.5 mL of (2), and 100 µL of (3). The UV-Vis spectra were taken following color development for 30 min in the dark and characterized at the peak maxima at 655 nm. Calibration samples were prepared: 0.0, 0.25, 0.5, 1.0, 2.5, 5.0, and 10.0 µg mL^{-1} of NH_4Cl which were then converted to µg mL^{-1} of NH_4^+. The calibration curve was found to exhibit good linearity (R^2 = 0.998, **see Figure C9**).

N_2H_4 was detected with the Watt and Chrisp method. One indicator solution was prepared: (1) 0.599 g of p-Dimethylaminobenzaldehyde and 3 mL concentrated HCl were dissolved in 30 mL ethanol. Sample detection was

performed by adding 2 mL of the electrolyte solution with 2 mL of indicator (1). Absorption was taken following 30 min of development in the dark and characterized by its peak maxima at 460 nm. Calibration samples were prepared: 0.0, 0.5, 1.0, 2.5, and 5.0 μg mL^{-1}. The calibration curve was found to exhibit good linearity (R^2 = 0.999, see **Figure C10**).

Calculation of FE and yield of NH_3:

Faradaic Efficiency (%):

$$FE_{NH_3}: \frac{3F \times C_{NH_3} \times V}{M(NH_4^+) \times Q}$$

Yield (ug h^{-1} mg^{-1}):

$$V_{NH_3}: \frac{C_{NH_3} \times V}{t \times m_{cat}}$$

Where F is the Faraday constant (96,485.3329 s A mol^{-1}), C_{NH_3} is the concentration of NH_3 (μg mL^{-1}), V is the volume of the electrolyte (mL), $M(NH_4^+)$ is the relative atomic mass of ammonia produced, Q is the accumulated charge, t is time in hours, and m_{cat} is the mass of the catalyst (mg).

4.3 MoO_2/C Synthesis and Characterization

Motivated by the rich NRR chemistry on Mo, we present the synthesis and characterization of highly dispersed, defect rich, MoO_2 nanoparticles grafted onto the surface of a conductive carbon nanowire support (MoO_2/C) **(Scheme 4.1)**. Our electrocatalytic system exhibits an average Faradaic efficiency (FE) of 31.3% and NH_3 yield of 21.2 μg h^{-1} mg^{-1} at a low applied potential of –0.1 V vs. RHE, displaying one of the highest activities and

selectivity towards NRR on a Mo-based system reported thus far (**Table C3**). An extensive combination of powder X-ray diffraction (PXRD) and pair distribution function (PDF) analysis along with X-ray absorption (XAS), X-ray photoelectron (XPS), and electron paramagnetic resonance (EPR) spectroscopies show that this material consists of mixed valance Mo(IV) , Mo(V), and Mo(VI) redox centers at the surface. This unique Mo composite catalyst demonstrates the power of rational design for exposing active sites on a conductive matrix of carbon nanowires.

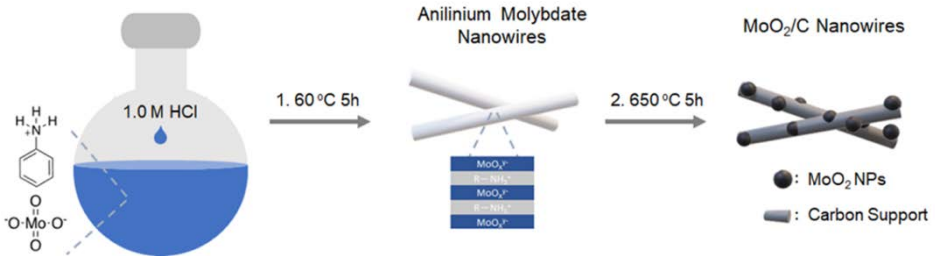

Scheme 4.1. Synthesis of MoO_2/C nanowires.

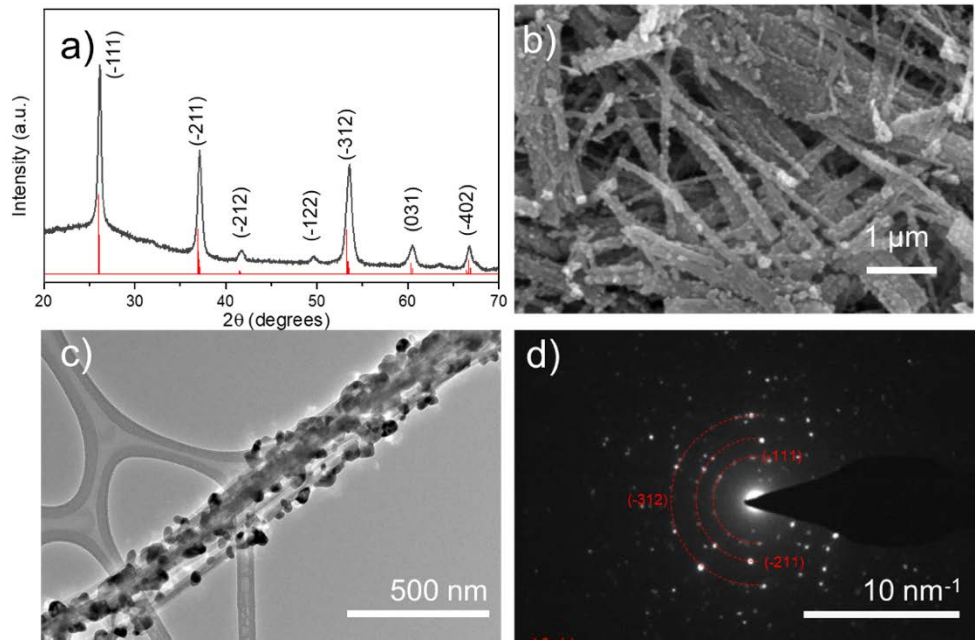

Figure 4.1. a) PXRD (peaks indexed as monoclinic MoO_2, JCPDS no. 32-0671), b) SEM, c) TEM, d) SAED of MoO_2/C nanowires.

The synthesis of MoO_2/C nanowires was adapted from a previously published procedure for Mo_2C/C.[37] Briefly, aniline is added dropwise to a stirring solution of ammonium molybdate. Nanowires are formed upon adjusting the pH of molybdate and aniline solution to 3.0 at 60 °C. XRD of the precursor indicates formation of anilinium molybdate with the formula $Mo_8O_{26}(C_6H_8N_2)_4 \cdot 2H_2O$ (**Figure C1**).[38] Scanning electron microscopy (SEM) confirms the anticipated nanowire morphology **(Figure C2).** Pyrolysis of the resulting anilinium molybdate at 650 °C under a constant stream of Ar results in the formation of MoO_2/C nanowires. PXRD shows a dominant presence of crystalline MoO_2 (**Figure 4.1a**). SEM and transmission electron microscopy (TEM) images illustrate Mo-based nanoparticles with the size range of 20-55 nm are decorated on the surface of the carbon nanowires (**Figures 4.1bc, and C3**). SEM energy-dispersive spectroscopy (EDS) confirms a roughly 1:2 (1:1.88±0.09) atomic ratio of Mo to O **(Figure C3)**. Selected area electron diffraction (SAED) on the MoO_2/C material corroborates the presence of crystalline MoO_2 (**Figure 4.1d**).

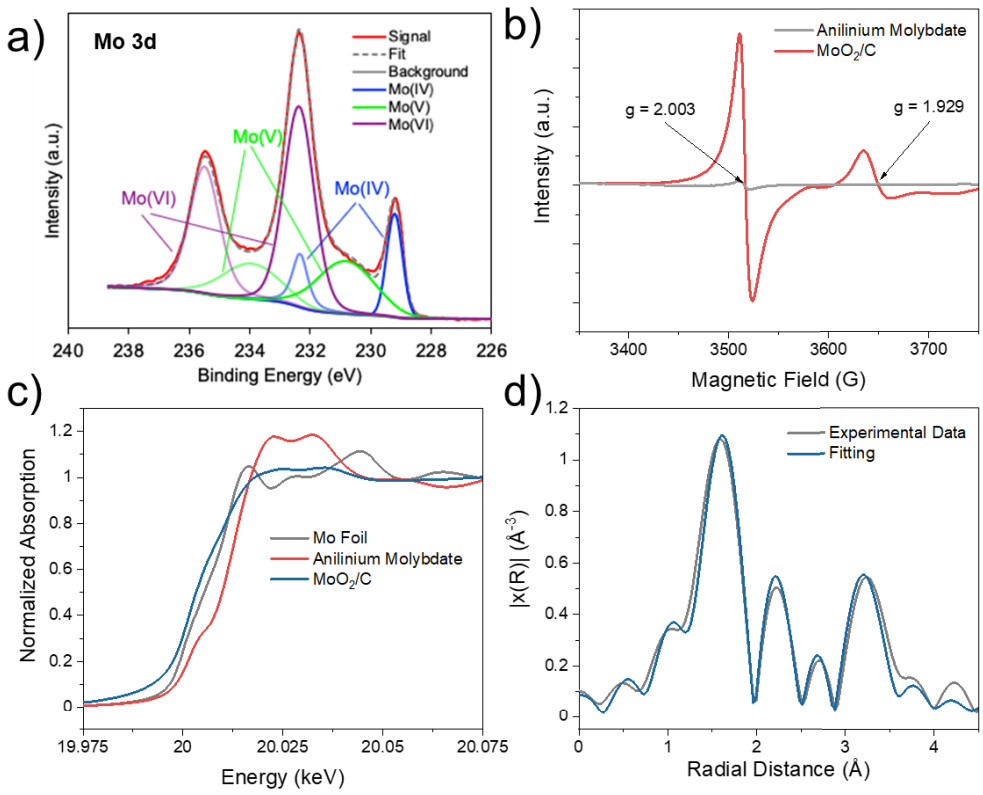

Figure 4.2. a) Fitted XPS data of Mo *3d* for the MoO_2/C composite, showing the presence of Mo(IV), Mo(V), and Mo(VI), b) EPR of anilinium molybdate and MoO_2/C nanowires, c) XANES of MoO_2/C, anilinium molybdate, and Mo foil, and d) Mo K-edge EXAFS for MoO_2/C.

We further conducted XPS to obtain compositional information of the MoO_2/C catalyst surface. **Figure 4.2a** shows the Mo *3d* region, where the surface Mo species (~ top 10 nm) can be fitted into three components, namely, Mo(VI), Mo(V), and Mo(IV). The Mo(VI) at 232.3 eV and 235.4 eV is the most dominant surface species, which comprises more than 60% of the Mo signal and is likely MoO_3. This species, the Mo(V) signal at 230.7 eV and 233.8 eV, and the remaining Mo(IV) signal at 229.2 eV and 232.3 eV illustrate a mixed valent Mo surface likely as a result of partial surface oxidation. The Mo(VI) and Mo(V) crystalline structures

were not detected by XRD measurements but were observed by XPS, which strongly suggests that Mo(VI) and MoO(V) environments are amorphous and not crystalline.To probe the apparent paramagnetic species within our material as well as the presence of possible oxygen vacancies, we performed EPR spectroscopy (**Figure 4.2b**). A strong signal is observed at g = 2.003, indicating the presence of electrons trapped in oxygen vacancies.[28] The g = 1.929 signal can be designated to a paramagnetic Mo(V) center that displays dipolar peak broadening,[39] which corroborates with XPS findings.

X-ray absorption spectroscopy (XAS) was further used to understand local Mo chemistry and structure. The X-ray absorption near edge structure (XANES) for the MoO_2/C nanowires and its anilinium molybdate precursor are shown in **Figure 4.2c** along with a reference Mo foil (first-order derivation in **Figure C4**). The MoO_2/C exhibits a lower E_0 as compared to the precursor material, indicating a reduced oxidation state in the bulk from the Mo(VI) in the precursor. Considering the XPS results (**Figure 4.2a**), this suggests that any Mo(VI) speciation is largely at the surface of the MoO_2 nanoparticles. The overall profile of the MoO_2/C strongly resembles that of previous reported XANES for MoO_2,[40] apart from a small pre-edge feature positioned at 20,004 eV. Note that the pre-edge feature for the Mo(VI) precursor is positioned at 20,006.6 eV, further indicating a lack of Mo(VI) in the bulk of the MoO_2/C. This feature shape and position at 20,004 eV more closely resemble those found in Mo(V) environments,[41] indicating the presence of possible defect sites in a MoO_2-type structure.

The extended X-ray absorption fine structure (EXAFS) for MoO_2/C is shown in **Figure 4.2d** and displays four prominent features, strongly indicating the presence of multiple Mo-containing species with two possible Mo-O and Mo-Mo contributions. With insights from the XANES and XPS observations, we modeled the mixed valency of MoO_2/C with Mo_8O_{23}, which contains both Mo(V) and Mo(VI), in conjunction with MoO_2 (**Figure C5**). The local structural contributions for MoO_2 yield Mo-O and Mo-Mo coordination numbers (CNs) of 4.53 ± 0.38 and 0.49 ± 0.24, respectively, which are significantly lower than 6.0 and 2.0 found in the bulk crystalline structure. Contributions from Mo-O and Mo-Mo from Mo_8O_{23} yielding CNs of 2.76 ± 0.52 and 2.07 ± 0.38 respectively, it is likely that the undercoordinated MoO_2 results are due to the presence of a Mo(V)-like species within the bulk of the material. The expanded Mo-Mo distances observed in EXAFS modeling of 2.93 ± 0.03 Å for MoO_2-like contributions (bulk value of 2.81 Å) and 3.44 ± 0.01 Å for Mo_8O_{23}-type distance (bulk value of 3.28 Å) are a further indication of a distorted and defect structure within the MoO_2/C (**Table C1**).

High energy XRD coupled to atomic PDF analysis was then performed to resolve the atomic scale structure of the material. Using crystallographic modeling techniques, the PDF is fit to a monoclinic MoO_2 lattice with a reasonable goodness of fit value (**Figure C6**, **Table C2**). Interestingly, the anisotropic temperature factors from our modeling in the O atoms are much higher than Mo atoms, indicating that the long-range order and symmetry in the O atoms is comparatively lacking vs Mo. This observation strongly suggests O vacancy formation, as

observed previously in defective metal oxides studied using PDF analysis,[42,43] and further supported by our XPS, EPR, and EXAFS observations.

4.4 Electrocatalytic Nitrogen Reduction

After determining their composition and structure, the MoO_2/C nanowires were evaluated for their performance towards the electrocatalytic NRR. Polarization curves were taken to assess the onset of nitrogen reduction (**Figure C7**). When the system is held under an Ar atmosphere, a gradual increase in current density following 0.0 V vs. RHE is observed, which is attributed to the hydrogen evolution reaction (HER), a parasitic side reaction of NRR. The sample purged with nitrogen gas shows an increase in the catalytic current density beginning at -0.1 V, implying an enhancement in catalytic activity in an N_2-rich system.

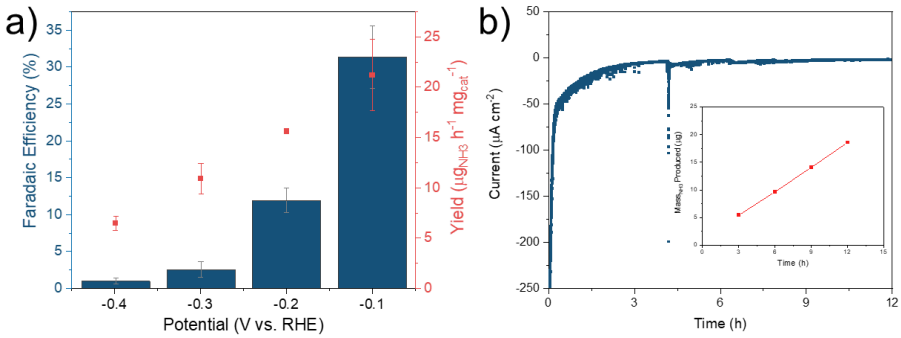

Figure 4.3. (a) Faradaic efficiencies and yields following CPE experiments of MoO_2 catalyst in 0.1 M HCl from -0.1 to -0.4 V vs. RHE. (b) Current-time profile for a long-term electrolysis exhibits steady-state current density over 12 h. (Inset: ammonia yields at each 3-hour time point).

Accordingly, controlled-potential electrolysis (CPE) was carried out between -0.1 to -0.4 V vs. RHE in 0.1 M HCl (pH = 1.0) under a continuous flow of nitrogen, operating at a relatively low overpotential to limit the evolution of hydrogen (**Figure 4.3a**). The chronoamperometric profiles (**Figure C8**) achieve

steady current densities within the first few minutes of electrolysis and remain stable for the full three hours of electrolysis. The only products of this system are NH_3, detected by the Indophenol Blue method,[44] and hydrogen (**Figure C9, C11**). No hydrazine was detected at any potential, characterized by the Watt and Chrisp method[45] (**Figure C10, C12**). The average FE for NH_3 was 31.3% with a yield of 21.2 μg h^{-1} mg^{-1} at a potential of -0.1 V vs. RHE, which is exceptionally high in comparison to other molybdenum oxide catalysts under similar conditions (**Table C3**). Unsurprisingly, the more negative potentials result in a sharp decrease of both FE and yield of NH_3 as HER becomes the dominant reaction pathway (**Figure C13**). To determine the presence of exogenous nitrogenous contaminants, several control experiments were performed on the bare carbon paper electrode under nitrogen and the MoO_2/C nanowire catalyst under Ar both of which generate negligible NH_3 (**Figure C13**). In addition, elemental analysis of the catalyst was conducted using ICP-OES and found MoO_2/C to contain approximately 2% N by mass. Assuming all the nitrogenous species in the catalyst can be converted to NH_3 during electrolysis, 2% N by mass translates to an upper bound of 2.4 µg of NH_3, which can represent a 9% error in our FE calculation. To track the possible leaching of N species from our catalyst, electrolysis under Ar were conducted and an average ammonia production of less than 0.2 μg (**Figure C14**) was determined. This analysis indicates that the majority of NH_3 is produced from the electrochemical reduction of the supplied nitrogen gas.

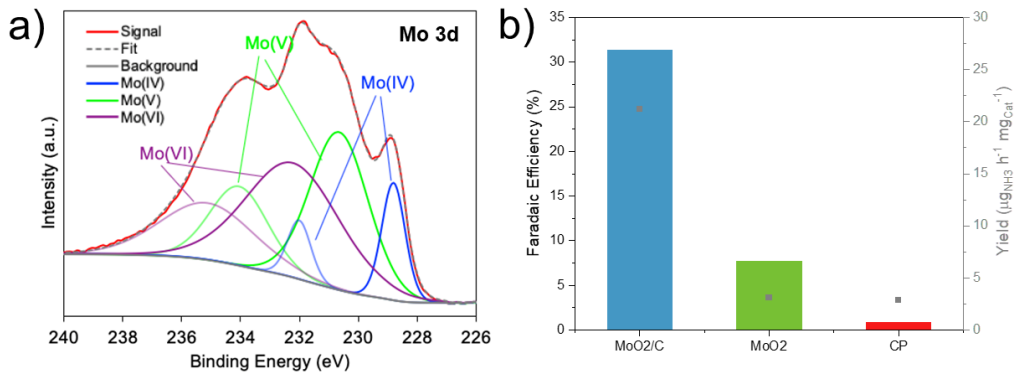

Figure 4.4. a) Post-electrolysis Mo *3d* XPS of MoO_2/C nanowires. b) FE and ammonia yields generated when using MoO_2/C nanowires, unsupported MoO_2 particles, and a control carbon paper electrode. CPE conditions: -0.1 V vs. RHE, 3 h, electrolyte = 0.1 M HCl.

An important property of a catalyst is its stability under reaction conditions. To this end, we evaluated the electrochemical stability of the MoO_2/C catalyst by performing CPE for 12 h (**Figure 4.3b**). Aliquots of electrolyte were removed at each 3-hour time point, and NH_3 in solution was quantified. The current density was stable for the full 12 hours with a linear increase in NH_3 (**Figure 4.3b**, inset). To further determine changes in surface morphology and composition, SEM, XPS, and XRD were conducted following 3 h of electrolysis at -0.1 V vs. RHE. SEM shows that the morphology is largely retained with some bundling of the nanowires (**Figure C15**). In addition, the XRD pattern is unchanged, showing that the major crystalline species remains MoO_2 (**Figure C16**). However, XPS show that the 3-h electrolyzed sample displays significant evolution of the MoO_2/C surface. Mo(V) replaces Mo(VI) to become the dominant Mo species on the surface, while the relative ratio of MoO_2 remains the same (**Figure 4.4a, Table C4)**. These findings are consistent with partial reduction of Mo(VI) under catalytic

conditions to Mo(V) indicating that Mo(VI) species on the electrode surface is unlikely a major catalytic component under these conditions.

We hypothesize that the defect-rich MoO_2/C is a more competent NRR catalyst than other reported Mo-based systems for several reasons: 1) the high particle dispersity results in an increased exposure of active sites, 2) the conductive carbonaceous support, which promotes electronic contact and transport[46], and 3) the Mo catalyst is rich in surface defects suitable for binding reaction intermediates.[47,48] To test these assumptions, we synthesized MoO_2 particles from well-established literature procedures.[49,50] This material exhibits similar chemical composition as shown by XRD (**Figure C17a**), with a spherical particle morphology with larger particle sizes (**Figure C17b)**. We observed a large initial difference when analyzing the cell resistance using EIS (**Figure C18**), where the electrode prepared with the MoO_2 particles showed a much higher intrinsic resistance compared to the MoO_2/C electrode. Comparison of the CPE results of MoO_2 particles to MoO_2/C nanowires (**Figure 4.4b**) shows MoO_2/C nanowires are superior to MoO_2 particles with an enhancement of 23.6% and 18.1 μg h^{-1} mg^{-1} in the FE and yield, respectively, at E = -0.1 vs. RHE. We attribute this performance enhancement to the unique morphology of the MoO_2/C nanowires. The configuration of surface defect rich MoO_2 nanoparticles grafted onto a conductive carbon support manifests a cooperative relationship between the two materials for an enhanced capacity for NRR.

4.5 Conclusions

Simultaneously achieving high catalytic selectivity and activity has been a critical challenge for NRR in aqueous systems. Herein, we reported a unique defect-rich MoO_2 catalyst supported on conductive carbon nanowires that can reach up to 31% selectivity towards NH_3 conversion with a yield of 21.2 μg h^{-1} mg^{-1} at the low potential of -0.1 V vs. RHE. These results illustrate that defect-rich MoO_2/C is a highly competitive catalyst compared to the existing Mo-based ones, which typically do not see significant yields until -0.3 and -0.4 V with lower NRR selectivity (**Table C3**). We assign the exceptional behavior of this catalyst to its unique architecture and defect sites. The highly dispersed MoO_2 nanoparticles on the surface of an amorphous carbon nanowire backbone decreases particle aggregation and increases the exposure of surface-active sites, leading to a higher yield rate. The conductive carbon backbone assists in funneling electrons into the nanoparticles. Moreover, the mixed Mo valency induced by in-situ reduction of the MoO_x surface and presence of oxygen vacancy sites have been shown to enable strong binding of nitrogen and reaction intermediates. Our study illustrates that catalyst morphology and composition play important roles in selective NRR. As the surfaces of low valance Mo compounds (e.g. MoC_2, Mo_2N_3) are easily subject to oxidation, our study reveals the importance of identifying and stabilizing the surface-active sites under reductive electrocatalytic conditions. Our findings add to the burgeoning body of work on developing earth-abundant electrocatalysts for selective conversion of molecular nitrogen to value-added nitrogen products.

4.6 References

(1) Lee, H. K.; Koh, C. S. L.; Lee, Y. H.; Liu, C.; Phang, I. Y.; Han, X.; Tsung, C. K.; Ling, X. Y. Favoring the Unfavored: Selective Electrochemical Nitrogen Fixation Using a Reticular Chemistry Approach. *Sci. Adv.* **2018**, *4* (3), 1–9. https://doi.org/10.1126/sciadv.aar3208.

(2) Erisman, J. W.; Sutton, M. A.; Galloway, J.; Klimont, Z.; Winiwarter, W. How a Century of Ammonia Synthesis Changed the World. *Nat. Geosci.* **2008**, *1* (10), 636–639. https://doi.org/10.1038/ngeo325.

(3) Zhao, Y.; Setzler, B. P.; Wang, J.; Nash, J.; Wang, T.; Xu, B.; Yan, Y. An Efficient Direct Ammonia Fuel Cell for Affordable Carbon-Neutral Transportation. *Joule* **2019**, *3* (10), 2472–2484. https://doi.org/10.1016/j.joule.2019.07.005.

(4) Qiu, W.; Xie, X. Y.; Qiu, J.; Fang, W. H.; Liang, R.; Ren, X.; Ji, X.; Cui, G.; Asiri, A. M.; Cui, G.; Tang, B.; Sun, X. High-Performance Artificial Nitrogen Fixation at Ambient Conditions Using a Metal-Free Electrocatalyst. *Nat. Commun.* **2018**, *9* (1), 1–8. https://doi.org/10.1038/s41467-018-05758-5.

(5) Chen, J. G.; Crooks, R. M.; Seefeldt, L. C.; Bren, K. L.; Morris Bullock, R.; Darensbourg, M. Y.; Holland, P. L.; Hoffman, B.; Janik, M. J.; Jones, A. K.; Kanatzidis, M. G.; King, P.; Lancaster, K. M.; Lymar, S. V.; Pfromm, P.; Schneider, W. F.; Schrock, R. R. Beyond Fossil Fuel–Driven Nitrogen Transformations. *Science* **2018**, *360* (6391). https://doi.org/10.1126/science.aar6611.

(6) Kyriakou, V.; Garagounis, I.; Vourros, A.; Vasileiou, E.; Stoukides, M. An Electrochemical Haber-Bosch Process. *Joule* **2020**, *4* (1), 142–158. https://doi.org/10.1016/j.joule.2019.10.006.

(7) Nazemi, M.; El-Sayed, M. A. The Role of Oxidation of Silver in Bimetallic Gold-Silver Nanocages on Electrocatalytic Activity of Nitrogen Reduction Reaction. *J. Phys. Chem. C* **2019**, *123* (18), 11422–11427. https://doi.org/10.1021/acs.jpcc.9b01107.

(8) Tan, L.; Yang, N.; Huang, X.; Peng, L.; Tong, C.; Deng, M.; Tang, X.; Li, L.; Liao, Q.; Wei, Z. Synthesis of Ammonia: Via Electrochemical Nitrogen Reduction on High-Index Faceted Au Nanoparticles with a High Faradaic Efficiency. *Chem. Commun.* **2019**, *55* (96), 14482–14485. https://doi.org/10.1039/c9cc06132k.

(9) Zhang, L.; Ji, X.; Ren, X.; Ma, Y.; Shi, X.; Tian, Z.; Asiri, A. M.; Chen, L.; Tang, B.; Sun, X. Electrochemical Ammonia Synthesis via Nitrogen Reduction Reaction on a MoS_2 Catalyst: Theoretical and Experimental Studies. *Adv. Mater.* **2018**, *30* (28), 2–7. https://doi.org/10.1002/adma.201800191.

(10) Zhu, X.; Liu, Z.; Liu, Q.; Luo, Y.; Shi, X.; Asiri, A. M.; Wu, Y.; Sun, X. Efficient and Durable N_2 Reduction Electrocatalysis under Ambient Conditions: β-FeOOH Nanorods as a Non-Noble-Metal Catalyst. *Chem. Commun.* **2018**, *54* (80), 11332–11335. https://doi.org/10.1039/c8cc06366d.

(11) Liu, Y.; Su, Y.; Quan, X.; Fan, X.; Chen, S.; Yu, H.; Zhao, H.; Zhang, Y.; Zhao, J. Facile Ammonia Synthesis from Electrocatalytic N_2 Reduction under Ambient Conditions on N-Doped Porous Carbon. *ACS Catal.* **2018**, *8* (2), 1186–1191. https://doi.org/10.1021/acscatal.7b02165.

(12) Liu, S.; Wang, M.; Qian, T.; Ji, H.; Liu, J.; Yan, C. Facilitating Nitrogen Accessibility to Boron-Rich Covalent Organic Frameworks via Electrochemical Excitation for Efficient Nitrogen Fixation. *Nat. Commun.* **2019**, *10* (1), 1–9. https://doi.org/10.1038/s41467-019-11846-x.

(13) Murakami, T.; Nishikiori, T.; Nohira, T.; Ito, Y. Electrolytic Synthesis of Ammonia in Molten Salts under Atmospheric Pressure. *J. Am. Chem. Soc.* **2003**, *125* (2), 334–335. https://doi.org/10.1021/ja028891t.

(14) Hoffman, B. M.; Lukoyanov, D.; Yang, Z. Y.; Dean, D. R.; Seefeldt, L. C. Mechanism of Nitrogen Fixation by Nitrogenase: The next Stage. *Chem. Rev.* **2014**, *114* (8), 4041–4062. https://doi.org/10.1021/cr400641x.

(15) Zhao, J.; Chen, Z. Single Mo Atom Supported on Defective Boron Nitride Monolayer as an Efficient Electrocatalyst for Nitrogen Fixation: A Computational Study. *J. Am. Chem. Soc.* **2017**, *139* (36), 12480–12487. https://doi.org/10.1021/jacs.7b05213.

(16) Liu, Y.; Zhu, X.; Zhang, Q.; Tang, T.; Zhang, Y.; Gu, L.; Li, Y.; Bao, J.; Dai, Z.; Hu, J.-S. Engineering Mo/Mo_2C/MoC Hetero-Interfaces for Enhanced Electrocatalytic Nitrogen Reduction . *J. Mater. Chem. A* **2020**, *8* (18), 8920–8926. https://doi.org/10.1039/d0ta03290e.

(17) Zhang, L.; Ji, X.; Ren, X.; Luo, Y.; Shi, X.; Asiri, A. M.; Zheng, B.; Sun, X. Efficient Electrochemical N_2 Reduction to NH_3 on MoN Nanosheets Array under Ambient Conditions. *ACS Sustain. Chem. Eng.* **2018**, *6* (8), 9550–9554. https://doi.org/10.1021/acssuschemeng.8b01438.

(18) Han, J.; Ji, X.; Ren, X.; Cui, G.; Li, L.; Xie, F.; Wang, H.; Li, B.; Sun, X. MoO_3 Nanosheets for Efficient Electrocatalytic N_2 Fixation to NH_3. *J. Mater. Chem. A* **2018**, *6* (27), 12974–12977. https://doi.org/10.1039/c8ta03974g.

(19) Ren, X.; Cui, G.; Chen, L.; Xie, F.; Wei, Q.; Tian, Z.; Sun, X. Electrochemical N_2 Fixation to NH_3 under Ambient Conditions: Mo2N Nanorod as a Highly Efficient and Selective Catalyst. *Chem. Commun.* **2018**, *54* (61), 8474–8477. https://doi.org/10.1039/c8cc03627f.

(20) Yang, D.; Chen, T.; Wang, Z. Electrochemical Reduction of Aqueous Nitrogen (N_2) at a Low Overpotential on (110)-Oriented Mo Nanofilm. *J. Mater. Chem. A* **2017**, *5* (36), 18967–18971. https://doi.org/10.1039/c7ta06139k.

(21) Ren, X.; Zhao, J.; Wei, Q.; Ma, Y.; Guo, H.; Liu, Q.; Wang, Y.; Cui, G.; Asiri, A. M.; Li, B.; Tang, B.; Sun, X. High-Performance N_2 -to-NH_3 Conversion Electrocatalyzed by Mo_2C Nanorod. *ACS Cent. Sci.* **2019**, *5* (1), 116–121. https://doi.org/10.1021/acscentsci.8b00734.

(22) Han, L.; Liu, X.; Chen, J.; Lin, R.; Liu, H.; Fang, L. U.; Bak, S.; Liang, Z.; Zhao, S.; Stavitski, E.; Luo, J.; Adzic, R. R.; Xin, H. L. Atomically Dispersed Molybdenum Catalysts for Efficient Ambient Nitrogen Fixation. *Angew.*

Chemie - Int. Ed. **2019**, *58* (8), 2321–2325. https://doi.org/10.1002/anie.201811728.

(23) Liang, J.; Ma, S.; Li, J.; Wang, Y.; Wu, J.; Zhang, Q.; Liu, Z.; Yang, Z.; Qu, K.; Cai, W. Boosting the Acidic Electrocatalytic Nitrogen Reduction Performance of MoS_2 by Strain Engineering. *J. Mater. Chem. A* **2020**, *8* (20), 10426–10432. https://doi.org/10.1039/d0ta03622f.

(24) Cao, N.; Chen, Z.; Zang, K.; Xu, J.; Zhong, J.; Luo, J.; Xu, X.; Zheng, G. Doping Strain Induced Bi-Ti^{3+} Pairs for Efficient N_2 Activation and Electrocatalytic Fixation. *Nat. Commun.* **2019**, *10* (1), 1–12. https://doi.org/10.1038/s41467-019-10888-5.

(25) Ling, Y.; Kazim, F. M. D.; Ma, S.; Zhang, Q.; Qu, K.; Wang, Y.; Xiao, S.; Cai, W.; Yang, Z. Strain Induced Rich Planar Defects in Heterogeneous WS_2/WO_2 enable Efficient Nitrogen Fixation at Low Overpotential. *J. Mater. Chem. A* **2020**, *8* (26), 12996–13003. https://doi.org/10.1039/c9ta13812a.

(26) Kong, W.; Zhang, R.; Zhang, X.; Ji, L.; Yu, G.; Wang, T.; Luo, Y.; Shi, X.; Xu, Y.; Sun, X. WO_3 Nanosheets Rich in Oxygen Vacancies for Enhanced Electrocatalytic N_2 Reduction to NH_3. *Nanoscale* **2019**, *11* (41), 19274–19277. https://doi.org/10.1039/c9nr03678d.

(27) Zhang, L.; Xie, X. Y.; Wang, H.; Ji, L.; Zhang, Y.; Chen, H.; Li, T.; Luo, Y.; Cui, G.; Sun, X. Boosting Electrocatalytic N_2 Reduction by MnO_2 with Oxygen Vacancies. *Chem. Commun.* **2019**, *55* (32), 4627–4630. https://doi.org/10.1039/c9cc00936a.

(28) Zhang, G.; Ji, Q.; Zhang, K.; Chen, Y.; Li, Z.; Liu, H.; Li, J.; Qu, J. Triggering Surface Oxygen Vacancies on Atomic Layered Molybdenum Dioxide for a Low Energy Consumption Path toward Nitrogen Fixation. *Nano Energy* **2019**, *59*, 10–16. https://doi.org/10.1016/j.nanoen.2019.02.028.

(29) Wu, T.; Zhao, H.; Zhu, X.; Xing, Z.; Liu, Q.; Liu, T.; Gao, S.; Lu, S.; Chen, G.; Asiri, A. M.; Zhang, Y.; Sun, X. Identifying the Origin of Ti^{3+} Activity toward Enhanced Electrocatalytic N_2 Reduction over TiO_2 Nanoparticles Modulated by Mixed-Valent Copper. *Adv. Mater.* **2020**, *32* (30), 1–8. https://doi.org/10.1002/adma.202000299.

(30) Li, C.; Ma, D.; Mou, S.; Luo, Y.; Ma, B.; Lu, S.; Cui, G.; Li, Q.; Liu, Q.; Sun, X. Porous $LaFeO_3$ Nanofiber with Oxygen Vacancies as an Efficient Electrocatalyst for N_2 Conversion to NH_3 under Ambient Conditions. *J. Energy Chem.* **2020**, *50*, 402–408. https://doi.org/10.1016/j.jechem.2020.03.044.

(31) Chu, K.; Liu, Y. P.; Cheng, Y. H.; Li, Q. Q. Synergistic Boron-Dopants and Boron-Induced Oxygen Vacancies in MnO_2 Nanosheets to Promote Electrocatalytic Nitrogen Reduction. *J. Mater. Chem. A* **2020**, *8* (10), 5200–5208. https://doi.org/10.1039/d0ta00220h.

(32) Chu, K.; Wang, J.; Liu, Y. P.; Li, Q. Q.; Guo, Y. L. Mo-Doped SnS_2 with Enriched S-Vacancies for Highly Efficient Electrocatalytic N_2 Reduction: The Critical Role of the Mo-Sn-Sn Trimer. *J. Mater. Chem. A* **2020**, *8* (15),

7117–7124. https://doi.org/10.1039/d0ta01688h.

(33) Chu, K.; Liu, Y. P.; Li, Y. B.; Wang, J.; Zhang, H. Electronically Coupled SnO_2 Quantum Dots and Graphene for Efficient Nitrogen Reduction Reaction. *ACS Appl. Mater. Interfaces* **2019**, *11* (35), 31806–31815. https://doi.org/10.1021/acsami.9b08055.

(34) Xia, L.; Li, B.; Zhang, Y.; Zhang, R.; Ji, L.; Chen, H.; Cui, G.; Zheng, H.; Sun, X.; Xie, F.; Liu, Q. Cr_2O_3 Nanoparticle-Reduced Graphene Oxide Hybrid: A Highly Active Electrocatalyst for N_2 Reduction at Ambient Conditions. *Inorg. Chem.* **2019**, *58* (4), 2257–2260. https://doi.org/10.1021/acs.inorgchem.8b03143.

(35) Wang, J.; Liu, Y. P.; Zhang, H.; Huang, D. J.; Chu, K. Ambient Electrocatalytic Nitrogen Reduction on a MoO_2/Graphene Hybrid: Experimental and DFT Studies. *Catal. Sci. Technol.* **2019**, *9* (16), 4248–4254. https://doi.org/10.1039/c9cy00907h.

(36) Jixin Zhu, Ting Zhu, Xiaozhu Zhou, Yanyan Zhang, Xiong Wen Lou, Xiaodong Chen, Hua Zhang, Huey Hoon Hnga, Q. Y. Facile Synthesis of Metal Oxide/Reduced Graphene Oxide Hybrids with High Lithium Storage Capacity and Stable Cyclability. *Nanoscale* **2011**, 1084–1089. https://doi.org/10.1039/c0nr00744g.

(37) Gao, Q.; Zhang, C.; Xie, S.; Hua, W.; Zhang, Y.; Ren, N.; Xu, H.; Tang, Y. Synthesis of Nanoporous Molybdenum Carbide Nanowires Based on Organic - Inorganic Hybrid Nanocomposites with Sub-Nanometer Periodic

Structures. *Chem. Mater.* **2009**, *21* (23), 5560–5562. https://doi.org/10.1021/cm9014578.

(38) Gao, Q.; Wang, S.; Fang, H.; Weng, J.; Zhang, Y.; Mao, J.; Tang, Y. One-Dimensional Growth of MoO_x-Based Organic-Inorganic Hybrid Nanowires with Tunable Photochromic Properties. *J. Mater. Chem.* **2012**, *22* (11), 4709–4715. https://doi.org/10.1039/c2jm15443a.

(39) H.J. Wagner, P. Driessen, C. F. S. EPR of Mo^{5+} in Amorphous MoO_3 Thin Films. *J. Non. Cryst. Solids* **1979**, *34* (3), 1–4. https://doi.org/10.1016/0022-3093(79)90020-6.

(40) Wen, B.; Wang, Q.; Lin, Y.; Chernova, N. A.; Karki, K.; Chung, Y.; Omenya, F.; Sallis, S.; Piper, L. F. J.; Ong, S. P.; Whittingham, M. S. Molybdenum Substituted Vanadyl Phosphate ε-$VOPO_4$ with Enhanced Two-Electron Transfer Reversibility and Kinetics for Lithium-Ion Batteries. *Chem. Mater.* **2016**, *28* (9), 3159–3170. https://doi.org/10.1021/acs.chemmater.6b00891.

(41) Jalilehvand, F.; Mah, V.; Leung, B. O.; Ross, D.; Parvez, M.; Aroca, R. F. Structural Characterization of Molybdenum(V) Species in Aqueous HCl Solutions. *Inorg. Chem.* **2007**, *46* (11), 4430–4445. https://doi.org/10.1021/ic062047c.

(42) Daiyan, R.; Lovell, E. C.; Bedford, N. M.; Saputera, W. H.; Wu, K. H.; Lim, S.; Horlyck, J.; Ng, Y. H.; Lu, X.; Amal, R. Modulating Activity through Defect Engineering of Tin Oxides for Electrochemical CO_2 Reduction. *Adv.*

Sci. **2019**, *6* (18), 1–9. https://doi.org/10.1002/advs.201900678.

(43) Daiyan, R.; Lovell, E. C.; Huang, B.; Zubair, M.; Leverett, J.; Zhang, Q.; Lim, S.; Horlyck, J.; Tang, J.; Lu, X.; Kalantar-Zadeh, K.; Hart, J. N.; Bedford, N. M.; Amal, R. Uncovering Atomic-Scale Stability and Reactivity in Engineered Zinc Oxide Electrocatalysts for Controllable Syngas Production. *Adv. Energy Mater.* **2020**, *2001381*, 1–9. https://doi.org/10.1002/aenm.202001381.

(44) Watt, G. W.; Chrisp, J. D. A Spectrophotometric Method for the Determination of Hydrazine. *Anal. Chem.* **1952**, *24* (12), 2006–2008. https://doi.org/10.1021/ac60072a044.

(45) Qu, X.; Shen, L.; Mao, Y.; Lin, J.; Li, Y.; Li, G.; Zhang, Y.; Jiang, Y.; Sun, S. Facile Preparation of Carbon Shells-Coated O-Doped Molybdenum Carbide Nanoparticles as High Selective Electrocatalysts for Nitrogen Reduction Reaction under Ambient Conditions. *ACS Appl. Mater. Interfaces* **2019**, *11* (35), 31869–31877. https://doi.org/10.1021/acsami.9b09007.

(46) Li, Y.; Kong, Y.; Hou, Y.; Yang, B.; Li, Z.; Lei, L.; Wen, Z. In Situ Growth of Nitrogen-Doped Carbon-Coated γ-Fe_2O_3 Nanoparticles on Carbon Fabric for Electrochemical N_2 Fixation. *ACS Sustain. Chem. Eng.* **2019**, *7* (9), 8853–8859. https://doi.org/10.1021/acssuschemeng.9b00852.

(47) Li, Y.; Chen, X.; Zhang, M.; Zhu, Y.; Ren, W.; Mei, Z.; Gu, M.; Pan, F. Oxygen Vacancy-Rich MoO_{3-x} Nanobelts for Photocatalytic N_2 Reduction

to NH_3 in Pure Water. *Catal. Sci. Technol.* **2019**, *9* (3), 803–810. https://doi.org/10.1039/c8cy02357c.

(48) Zhao, S.; Liu, H. X.; Qiu, Y.; Liu, S. Q.; Diao, J. X.; Chang, C. R.; Si, R.; Guo, X. H. An Oxygen Vacancy-Rich Two-Dimensional Au/TiO_2 Hybrid for Synergistically Enhanced Electrochemical N_2 Activation and Reduction. *J. Mater. Chem. A* **2020**, *8* (14), 6586–6596. https://doi.org/10.1039/d0ta00658k.

(49) Zhou, E.; Wang, C.; Zhao, Q.; Li, Z.; Shao, M.; Deng, X.; Liu, X.; Xu, X. Facile Synthesis of MoO_2 Nanoparticles as High Performance Supercapacitor Electrodes and Photocatalysts. *Ceram. Int.* **2016**, *42* (2), 2198–2203. https://doi.org/10.1016/j.ceramint.2015.10.008.

(50) Ou, P.; Zhou, Q.; Li, J.; Chen, W.; Huang, J.; Yang, L.; Liao, J.; Sheng, M. Facile Ethylene Glycol-Assisted Hydrothermal Synthesis of MoO_2 Nanospheres for High-Performance Supercapacitors. *Mater. Res. Express* **2019**, *6* (9). https://doi.org/10.1088/2053-1591/ab2e49.

Appendix A

Supporting Information for Chapter 2: Effects of Substrate Porosity in Carbon Aerogel Supported Copper for Electrocatalytic Carbon Dioxide Reduction

Table of Contents

A3 Tables

A1 Supplemental Experimental Conditions

A1.1 Materials

Resorcinol (99%), formaldehyde (37% w/w aqueous solution stabilized with 7-8% methanol), sodium carbonate (≥ 99.95%), copper(II) nitrate hemi(pentahydrate) (≥ 99.99%, trace metal basis), Nafion solution (5% w/w in water and 1-propanol), graphite rod counter electrode and glassy carbon plates (2.5 x 2.5 cm^2, Type 1) were purchased from Alfa Aesar. Reagent alcohol (94%-96% v/v), ethanol (200 proof, ≥99.9%), sodium bicarbonate (≥ 99.998%, metals basis), dimethyl sulfoxide (≥ 99.9%), nitric acid (67%-70% trace metal grade) were purchased from Fisher Scientific. Gaseous hydrogen, methane (≥ 99.99%), ethylene (≥ 99.9%), carbon monoxide (≥ 99.9%) and carbon dioxide (≥ 99.9%) were from Airgas. Glassy carbon electrode (3 mm dia) and Ag/Ag/Cl reference electrode were from CH Instruments and BASi, respectively. The Pt counter electrode (≥99.9%) was purchased from uGems.

A1.2 General Instrumentation

The morphology and composition of Cu/CA was characterized by a JEOL 6700F Scanning Electron Microscope equipped with a TEAM EDS system. Scanning TEM (STEM) of Cu/CA samples was performed on a JEOL JEM 2100 Field Emission Gun (FEG) TEM and HRTEM was performed on a JEOL JEM 2100 LaB_6 TEM. High Resolution TEM (HRTEM) images were acquired on the JEOL JEM 2100 LaB_6 TEM. Images were analyzed and processed using Gatan Digital Micrograph and ImageJ software. Local structure and chemistry of Cu was

examined using XAS performed at the 10-BM beamline of the Advanced Photon Source. Powder X-ray diffraction was done on a Bruker D8 Focus diffractometer, with Cu Kα source and LynxEye detector. The Brunauer–Emmett–Teller (BET) surface area and pore-size distribution were characterized by Micromeritics ASAP 2020 Plus instrument. The BET surface area analysis used the $P/P_0 < 0.08$ region, where the C-constant is positive. Average pore size is calculated based on the BJH pore-size distribution curve. Hg porosimetry experiments were conducted on a MicroActive AutoPore V 9600. Raman spectroscopy measurements were performed using a Horiba Jobin-Yvon T64000 spectrometer equipped with an Olympus microscope, using the 514.5 nm line of the Spectra-Physics Ar^+ – Kr^+ laser for excitation. The surface of Cu/CA was characterized by a PHI 5600 X-ray Photoelectron Microscopy (XPS) using Mg Kα X-ray (1253.6 eV) radiation. All electrochemistry measurements were conducted on an Ivium-n-STAT Multichannel Electrochemical Analyzer.

A1.3 Characterization

Elemental analysis: The copper content was quantified by atomic adsorption spectroscopy (AAS) using a Perkin Elmer AAnalyst 100 system and Perkin Elmer Intesitron hollow cathode lamps. To prepare the sample, 1 mg of Cu/CA was stirred in 16% nitric acid aqueous solution and the mixture was heated at 60 °C overnight. A syringe filter was used to remove the remaining solids and the solution was diluted with a 2% nitric acid aqueous solution in a 50 mL

volumetric flask. A standard curve was used by conducting AAS measurements with Cu standard solutions in 2% nitric acid.

Transmission Electron Microscopy (TEM): Cu/CA samples for TEM were dispersed in ethanol solution at 0.5 g L^{-1} followed by sonication treatment for 30 s to form homogenous particle suspensions. 2 μL of the suspension was drop-cast onto a carbon TEM grid (Ted Pella Inc., 01824) and then air-dried. TEM grids were treated by UV-Ozone plasma cleaner (MTI Corp) for 30 minutes to remove contamination before characterization. Scanning TEM (STEM) of Cu/CA samples was performed on a JEOL JEM 2100 Field Emission Gun (FEG) TEM and HRTEM was performed on a JEOL JEM 2100 LaB_6 TEM. Both TEMs were operated with an accelerating voltage of 200 kV. STEM mode was used to obtain the annular dark field (ADF) images of Cu/CA sample with a beam spot size of 1.5 nm and camera length of 12 cm. ADF STEM images were captured with Digital Micrograph using 1024 pixels × 1024 pixel image size and 25 μs dwell time. Images were analyzed and processed using Gatan Digital Micrograph and ImageJ software. Energy-dispersive X-Ray Spectroscopy (EDS) line scans were performed in STEM mode with a spot size of 1.5 nm.

X-ray Absorption Spectroscopy (XAS): Samples were prepared by placing as-synthesized aerogels between Kapton tape. Experiments were performed in fluorescence mode using a four-channel Si drift detector wherein the samples were rotated ~45° normal to the direction of the X-ray beam to maximize signal. Data was collected from ~150 eV below the Cu K-edge (8797 eV) up to ~800 eV past

the edge. The extended X-ray absorption fine structure (EXAFS) data are obtained by first converting the XAS data to *k*-space (k^2-weighted), followed by a Fourier transform to r-space. Data processing and linear combination fitting was performed in the program Athena, while EXAFS modeling was performed using the Artemis software package.[32] Linear combination fitting was performed by modeling each sample from -15 eV below to 50 eV above the Cu K-edge. For EXAFS modeling, scattering paths were taken from fcc Cu, along with Cu-O and Cu-Cu nearest neighbors from known crystal structure of Cu_2O. The value for S_0^2 for Cu was determined to be 0.8833 from modeling the EXAFS from a Cu foil in transmission mode and used for all subsequent EXAFS modeling.

Electroactive surface area (EASA) measurement: An ink slurry composed of Cu/CA and a Nafion binder (see above) was casted onto a polished 3 mm glassy carbon electrode. The EASA of the Cu/CA composite electrode was calculated by taking cyclic voltammograms of a 5 mM $K_3[Fe(CN)_6]$ in a 0.5 M Na_2SO_4 aqueous solution at various scan rates according to the Randles-Sevcik equation:

$$I_p = (2.69 \times 10^5) n^{3/2} A D^{1/2} C \nu^{1/2}$$

where I_p is the peak current, n equals 1, D is the diffusion coefficient, ν is the scan rate, C is the concentration of $K_3[Fe(CN)_6]$, and A is the calculated electrochemically active surface area (EASA) of Cu/CA samples. In all cases, a redox feature centered at 0.23 V vs. Ag/AgCl is observed with a peak-to-peak separation of 0.083 V (Figure A11). The calculated EASA among samples are comparable (Table A2). Current densities are normalized to EASA.

Control electrolysis experiments: As a control to ensure the Pt counter electrode does not affect the overall catalysis, linear sweep voltammographs (LSV) of Cu/CA were taken before and after a 2.5-h bulk electrolysis at -1.16 V vs RHE in 0.1 M $NaHCO_3$ under CO_2 and N_2 with Pt as the counter electrode and the same H-cell configuration as described above (Figure A16). An increase in current density (from HER) is expected if Pt ions had migrated across to the working compartment and deposited onto the Cu/CA electrode. As shown in Figure A19, the LSVs are unchanged before and after electrolysis, demonstrating that the Pt counter electrode does not interfere with the catalysis. As a control to confirm the Cu particle is the active catalytic site, metal-free CA-400 is tested for CO_2RR under the same catalytic conditions. Negligible CO_2RR products are observed at all potentials, with hydrogen being the predominant gas product (Figure A20). In addition, a representative long-term electrolysis using Cu/CA-400 at –0.81 V is shown in Figure A21. The small decrease in current density over 8 h is attributed to the mechanical instability of the Nafion film from rapid bubble generation. In addition, isotopically labeled $^{13}CO_2$ and $NaH^{13}CO_3$ were used to demonstrate that the reduced carbon products are derived from CO_2/CO_3^{2-} and not from the degradation of the carbon aerogel (Table A5).

Product quantification: Each gas product was quantified based on a standard curve, which was made by plotting the integrated peak area from GC against the injection volume of the pure gas. The volume of product was calculated by fitting the integrated peak area to the standard curve. Standard curve was

determined for each gas product, i.e. hydrogen, carbon monoxide, methane and ethylene respectively. Specific current density for each gas product was calculated by the following equation:

$$j_{gas} = \frac{F\ P\ V\ m}{R\ T\ t\ A}$$

where *j* is the specific current density, *F* is the Faradaic constant (96,485 C mol^{-1}), *P* is the pressure (1 atm), *V* is the volume of product gas calculated by the standard curve (mL), *m* is the number of electrons needed to produce one product gas molecule (2 for H_2, 2 for CO, 2 for HCO_2H, 8 for CH_4, 12 for C_2H_4), *R* is the gas constant (82.057 mL atm K^{-1} mol^{-1}), *T* is 298 °K, *t* is the electrolysis time (s), *A* is the electroactive surface area of each material. Similarly, formation rate was obtained by:

$$r_{gas} = \frac{P\ V}{R\ T\ t\ A}$$

The liquid product was quantified by a Bruker Advance 400 MHz FT-NMR spectrometer with dimethylsulfoxide (DMSO) as internal standard.[21] To prepare the sample, 0.5 mL of the electrolyte from the working compartment after electrolysis was added to 0.1 mL of D_2O in a NMR tube. DMSO was added to form a concentration of 4.70 x 10^{-5} M. The amount of product was determined by integrating the peak area of product and DMSO. Specific current density of liquid product was calculated by the following equation:

$$j_{liquid} = \frac{6\ m\ F\ S_{liquid}\ C_{DMSO}}{n\ S_{DMSO}\ t\ A} \times V_{NMR\ tube} \times \frac{V_{chamber}}{V_{electrolyte}}$$

where S_{liquid} and S_{DMSO} are the integration peak area from NMR spectrum, C_{DMSO} is the concentration of DMSO in NMR tube (4.70×10^{-5} M), n is the number of protons contribute to the peak area of liquid product (1 for formate acid), and $V_{chamber}$, $V_{electrolyte}$, *and* $V_{NMR\ tube}$ are the total solution volume in the working electrode chamber, the total sample volume removed from the electrolysis, and the total liquid volume in the NMR tube after adding DMSO, respectively. A typical NMR spectrum is shown in Figure A22. Comparison with other carbon supported Cu catalysts is shown (**Table A7**)

A2 Figures

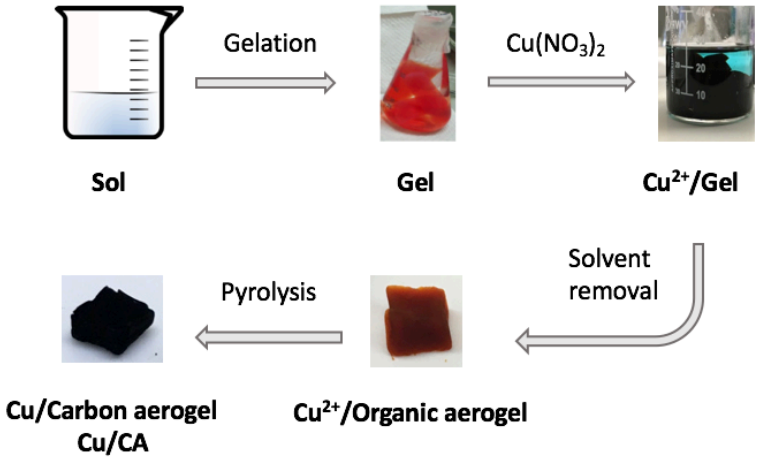

Figure A1. Sol-gel Synthesis for Cu/CA catalysts.

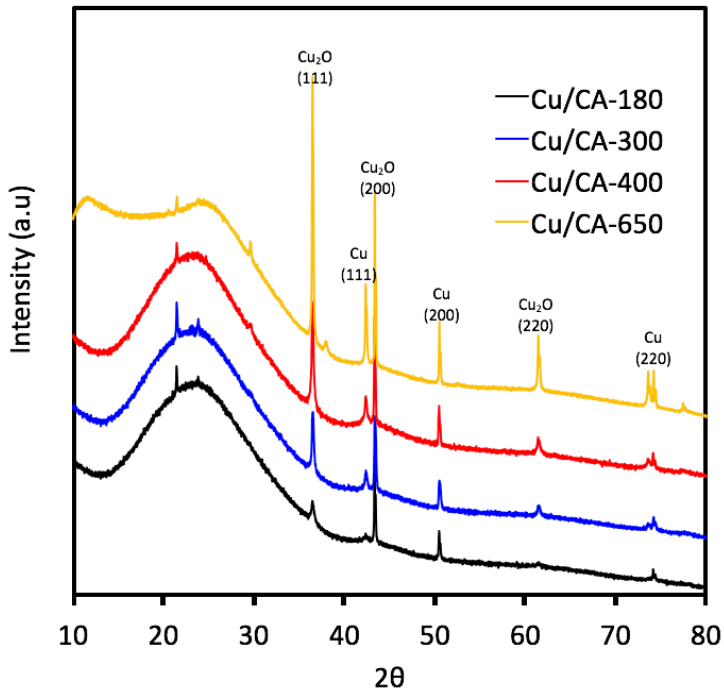

Figure A2. Powder XRD of Cu/CA-180, Cu/CA-300, Cu/CA-400 and Cu/CA-650. The XRD clearly shows the presence of Cu_2O and metallic Cu in all samples and a similar intensity ratio in each sample.

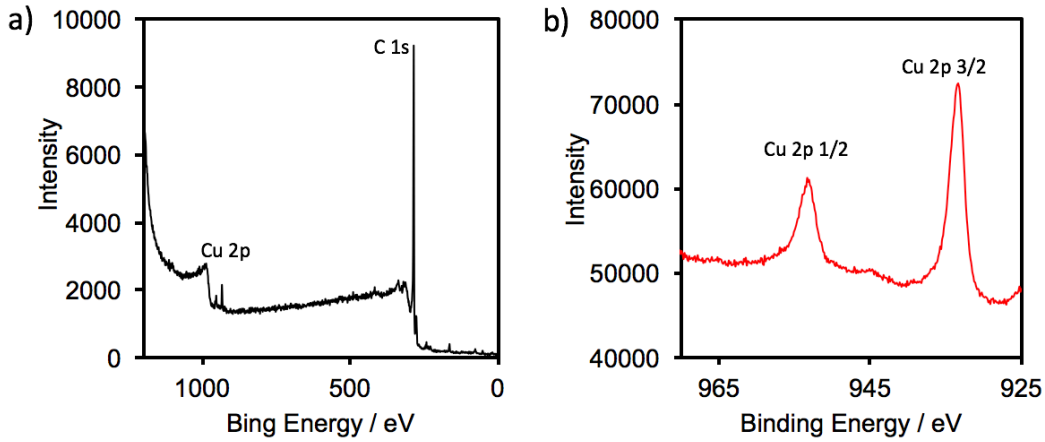

Figure A3. (a) Survey scan of XPS, and (b) scan of Cu region at a depth of 300 nm of Cu/CA-180.

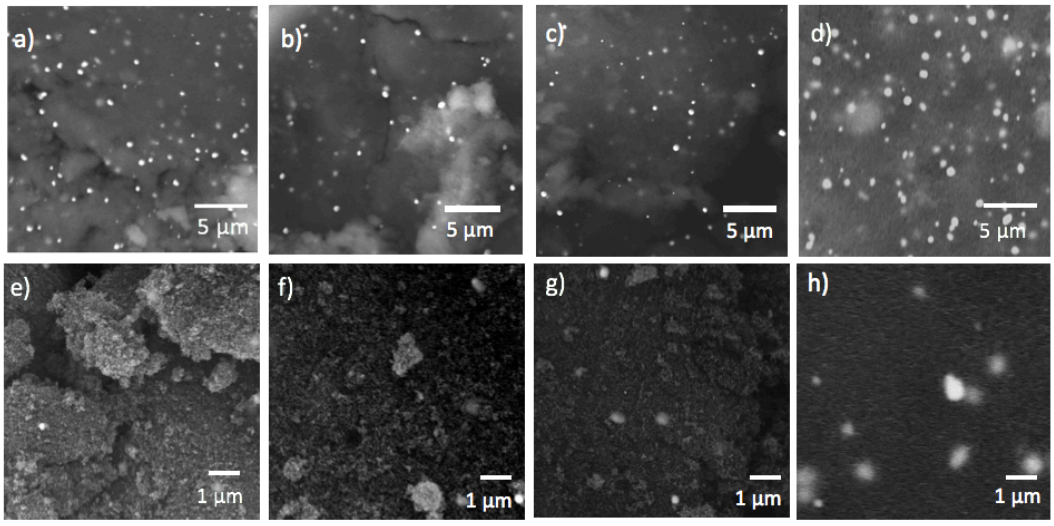

Figure A4. SEM image of (a, e) Cu/CA-180, (b, f) Cu/CA-300, (c, g) Cu/CA-400, and (d, h) Cu/CA-650.

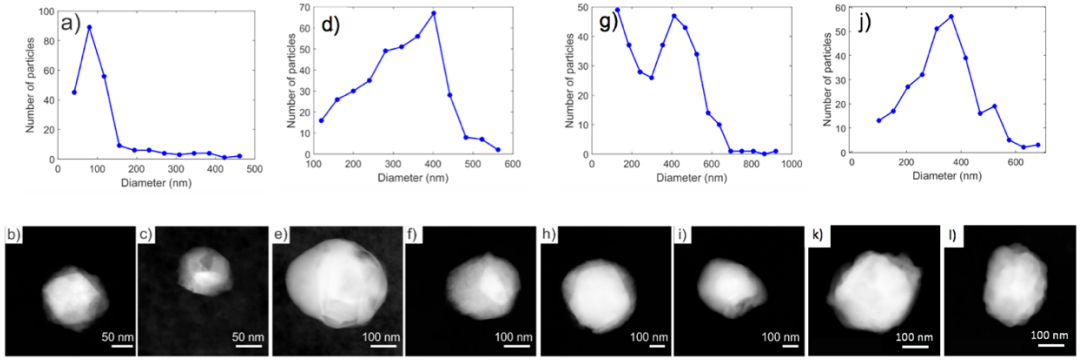

Figure A5. Cu particle size distributions (PSD) and STEM images for Cu/CA-180 (a-c), Cu/CA-300 (d-f), Cu/CA-400 (g-i), Cu/CA-650 (j-l). Each PSD was determined from measurements of at least 200 particle sizes.

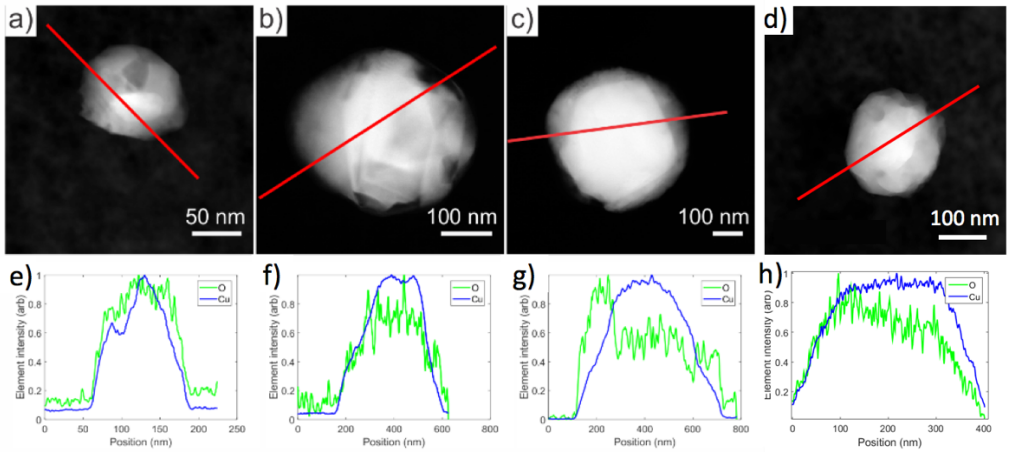

Figure A6. STEM-EDS elemental line scans images of Cu particles from (a,d) Cu/CA-180, (b,e) Cu/CA-300, (c,f) Cu/CA-400 and (d,h) Cu/CA-650. Solid red lines indicate the position and length of the line scan. The data in the plots are normalized to the maximum element intensity.

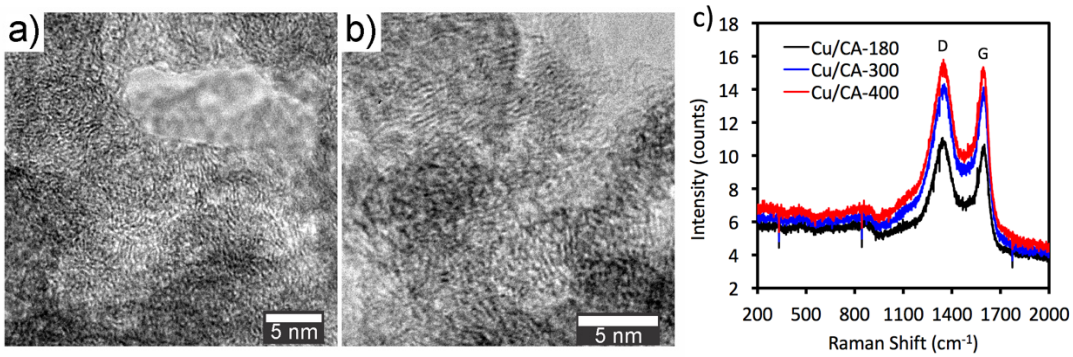

Figure A7. Representative HRTEM images of carbon aerogel from (a) Cu/CA-400 and (b) Cu/CA-180, showing the presence of both amorphous and graphitic carbon, and (c) Raman spectrum of Cu/CA-180, Cu/CA-300 and Cu/CA-400.

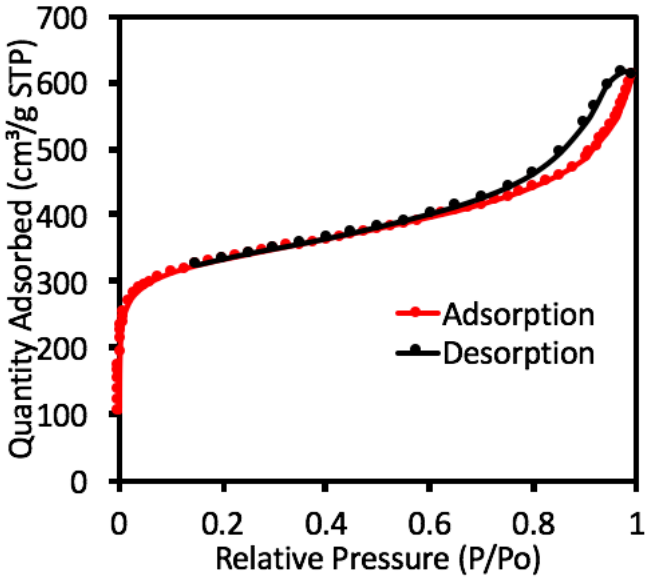

Figure A8. Representative nitrogen adsorption/desorption isotherms of Cu/CA-180.

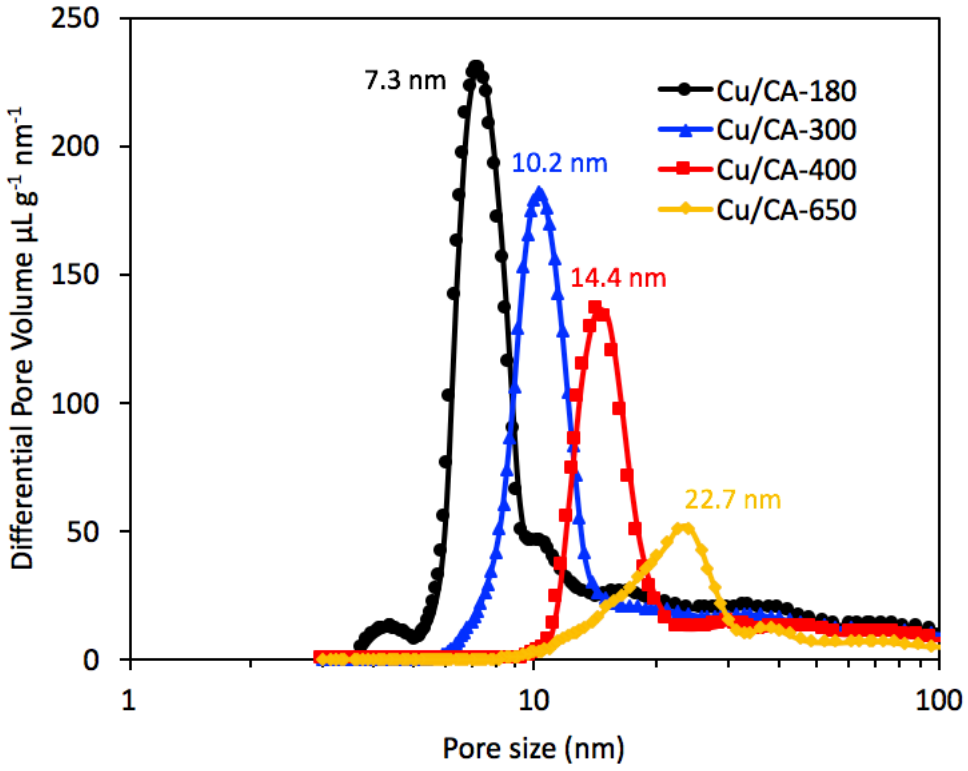

Figure A9. Hg Porosimetry Pore Size Distribution. The data corroborate the trends observed in BJH analysis (Cu/CA-180 < Cu/CA-300 < Cu/CA-400 < Cu/CA-650). Previous reports have shown that Hg intrusion can compress the pores of carbon aerogels and xerogels (Journal of Non-Crystalline Solids 186 (1995) 309-315; Journal of Non-Crystalline Solids 292 (2001) 138-149)). Thus, BJH analysis was primarily used in the main text.

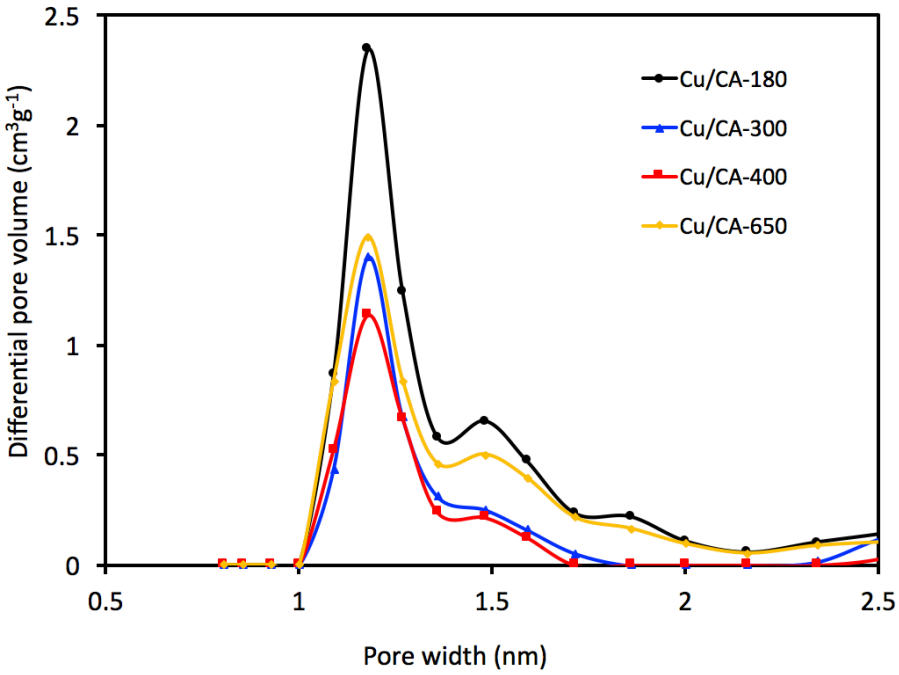

Figure A10. DFT Pore Size Distribution of Micropores.

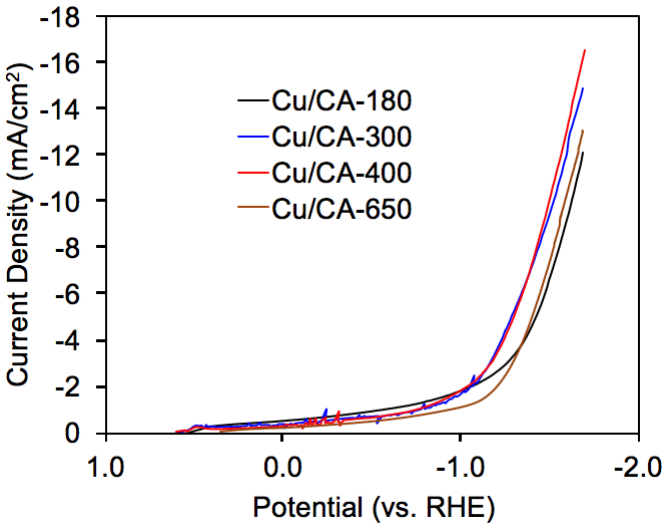

Figure A11. Linear sweep voltammetry experiment of Cu/CA-180, Cu/CA-300, Cu/CA-400, and Cu/CA-650 in CO_2 saturated 0.1 M $NaHCO_3$ solution, demonstrating high electrocatalytic activity from Cu/CA-300 and Cu/CA-400.

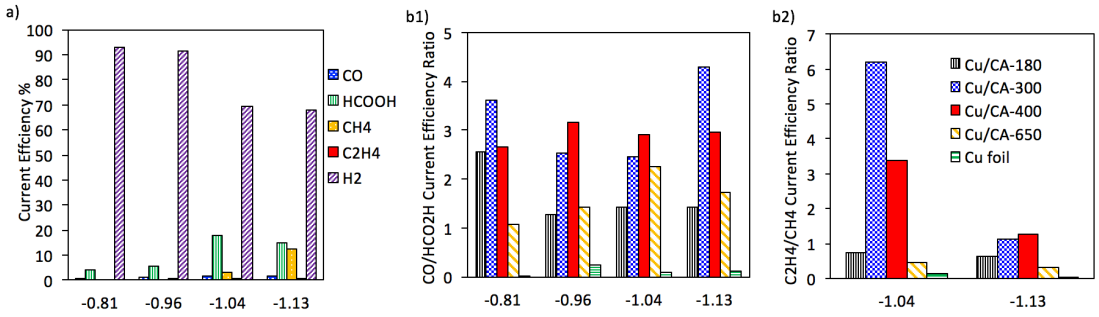

Figure A12. CO_2RR selectivity on Cu foil (a), comparison of CO/HCO_2H ratio (b1) and C_2H_4/CH_4 ratio (b2) of Cu foil to Cu/CAs.

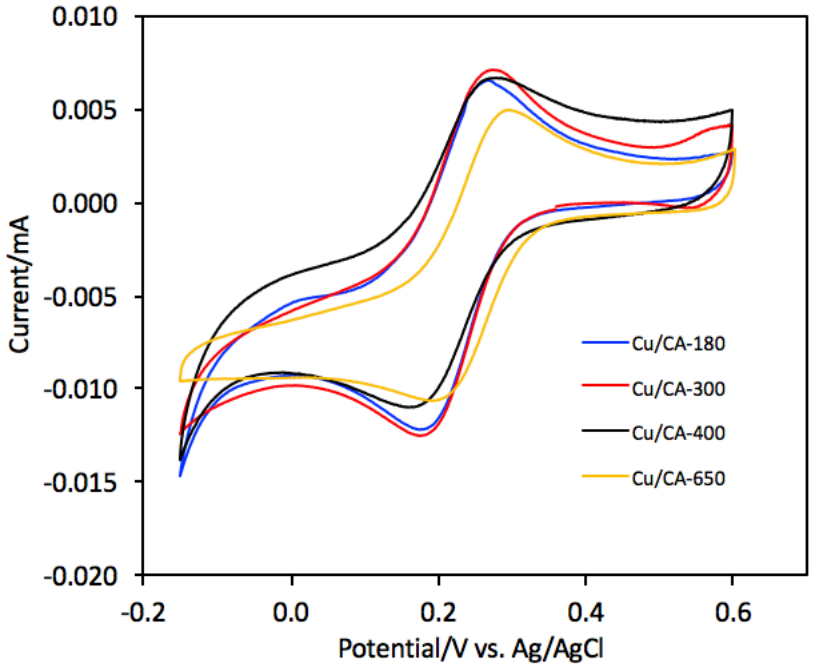

Figure A13. Cyclic Voltammograms in 0.5 M $K_3Fe(CN)_6$ at a scan rate of 5 mV/s.

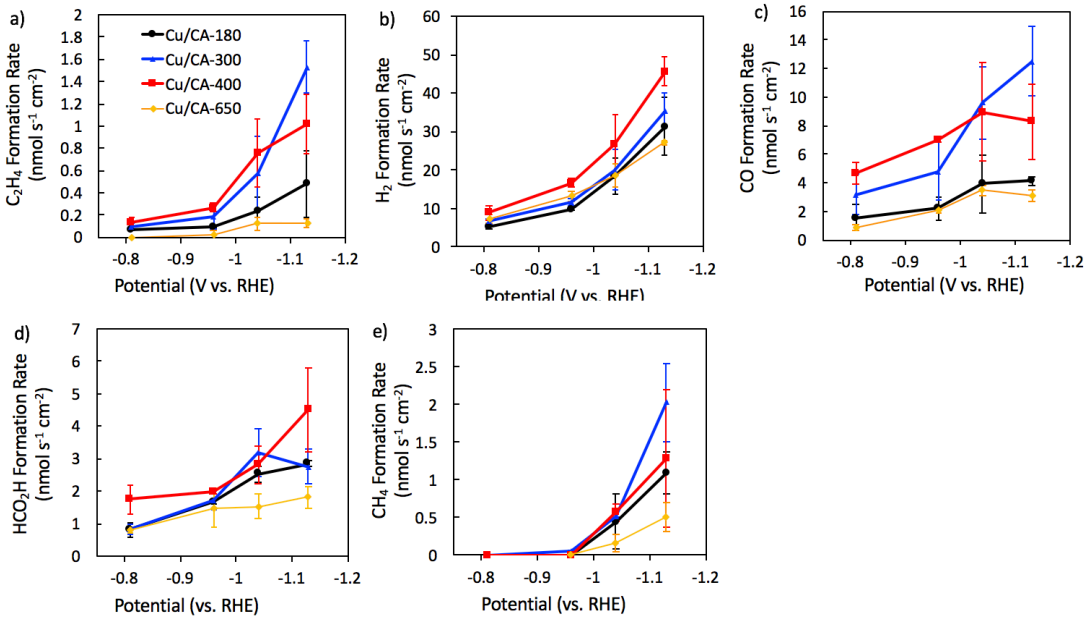

Figure A14. Formation rate of different products on all samples

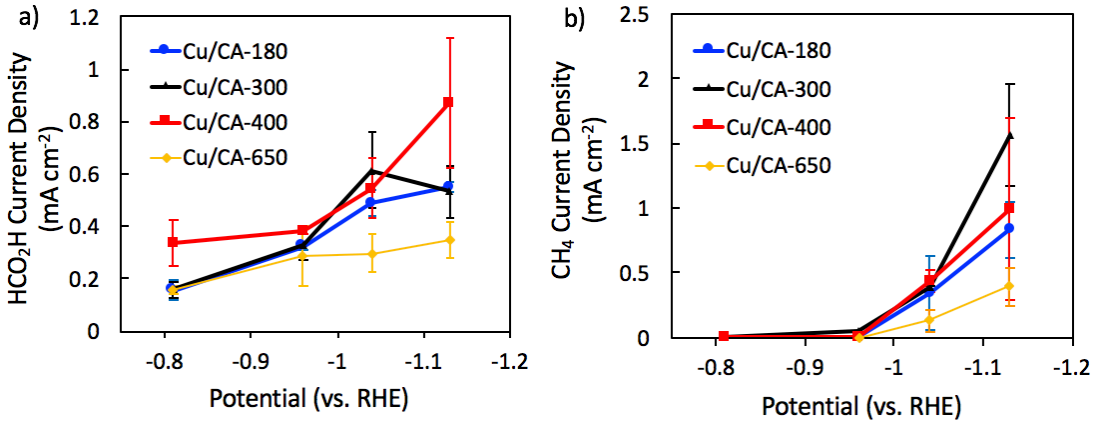

Figure A15. Specific current densities of (a) formate and (b) methane on Cu/CA-180, Cu/CA-300, Cu/CA-400, and Cu/CA-650 are invariant with respect to potentials. Current density normalized to EASA.

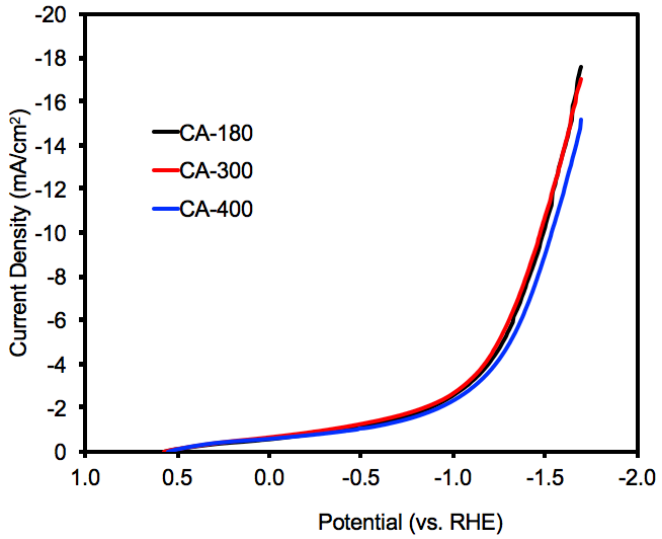

Figure A16. Linear sweep voltammetry experiment of metal free CA-180, CA-300, and CA-400 in CO_2-saturated 0.1 M $NaHCO_3$ solution. The three samples show no major differences, demonstrating the carbon aerogel electrodes do not alter HER and CO_2RR activities.

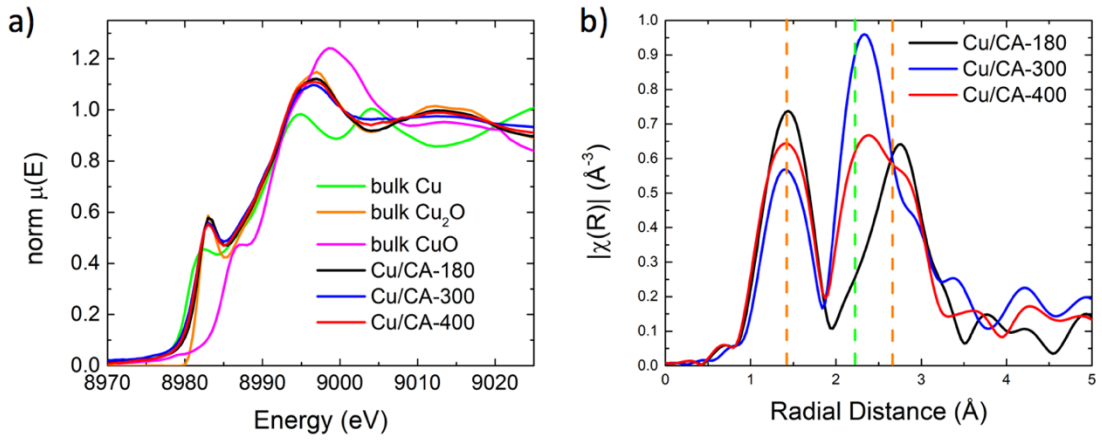

Figure A17. Cu K-edge XAS data showing a) extensive Cu oxidation in XANES and b) EXAFS modeling. The orange dashed line represent the Cu-O (left) and Cu-Cu (right), while the green dashed line represents Cu-Cu interactions in metallic Cu.

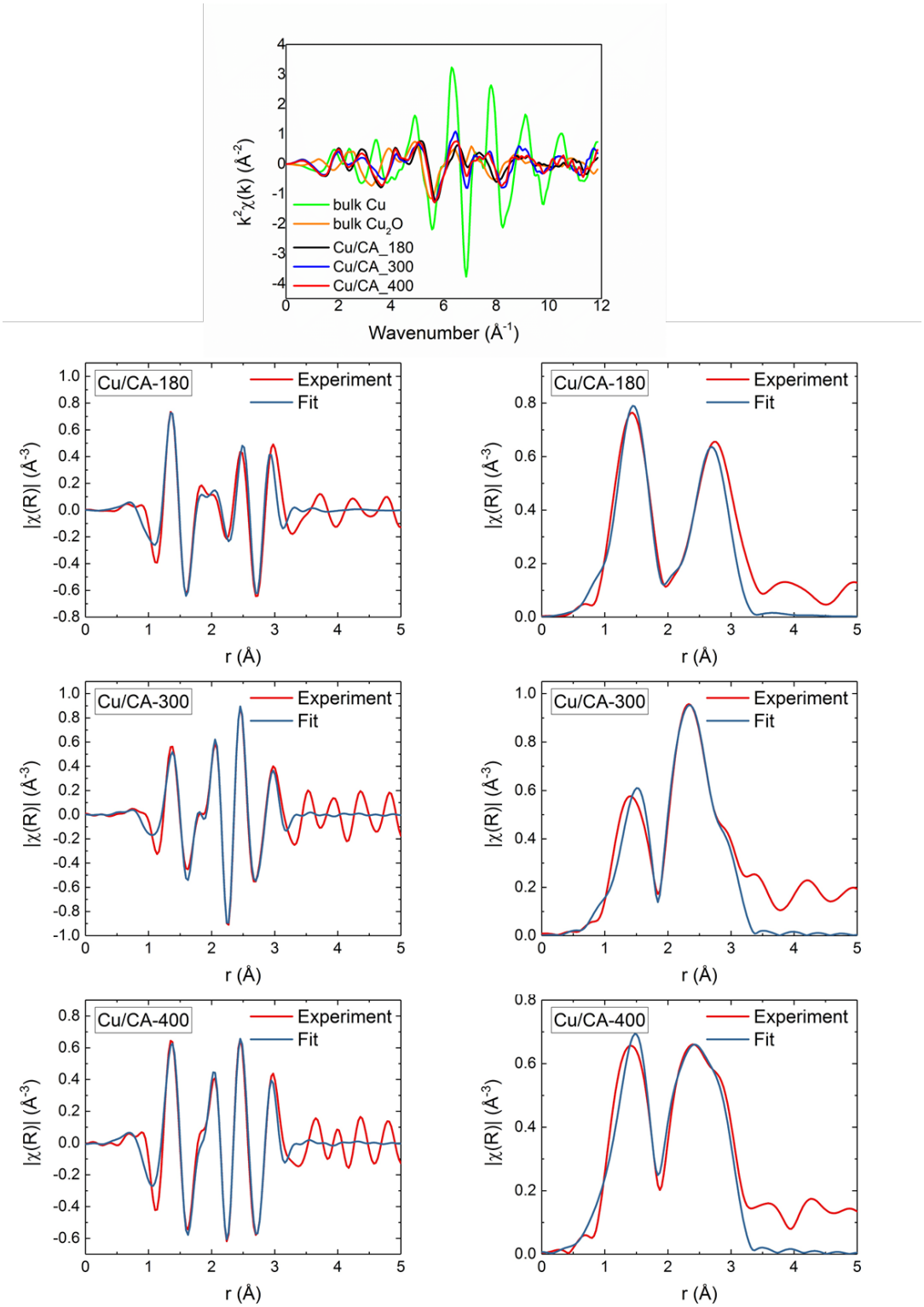

Figure A18. XAS *k*-space and EXAFS Fits

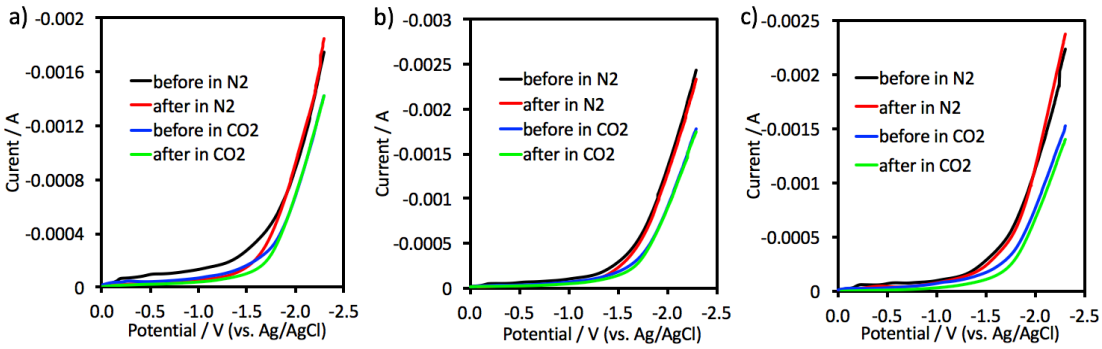

Figure A19. Comparison of CVs in 0.1 M $NaHCO_3$ solution before and after 2-h bulk electrolysis at -1.13 V in CO_2 and N_2 atmospheres of (a) Cu/CA-180, (b) Cu/CA-300 and (c) Cu/CA-400. The unchanged CVs after 2-h bulk electrolysis at the highest tested potential demonstrate that there is negligible Pt deposition on Cu/CA and the use of a Pt counter electrode does not impact CO_2RR and HER. No control for Cu/CA-650 is needs as its electrolysis were done with a graphite rod counter electrode.

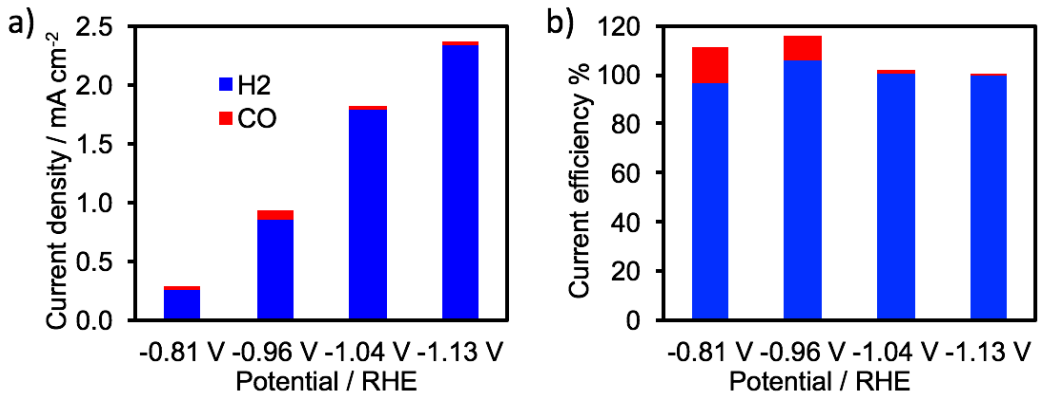

Figure A20. (a) Current density, and (b) current efficiency of CO_2RR products on metal-free CA-400 at different potentials, demonstrating negligible CO_2RR activity from the carbon aerogel electrodes.

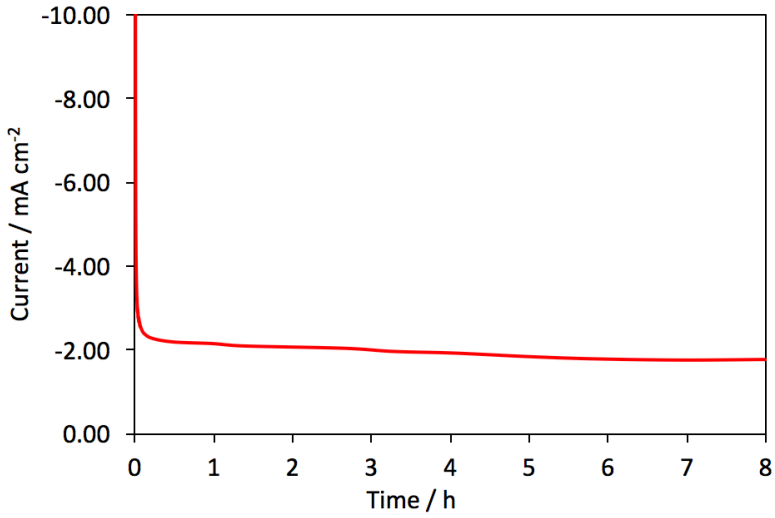

Figure A21. Current to time plot of bulk electrolysis of Cu/CA-400 at -0.81 V for 8 hours. We attribute the slight decline in current density to the mechanical instability of the catalyst film from gas bubble formation.

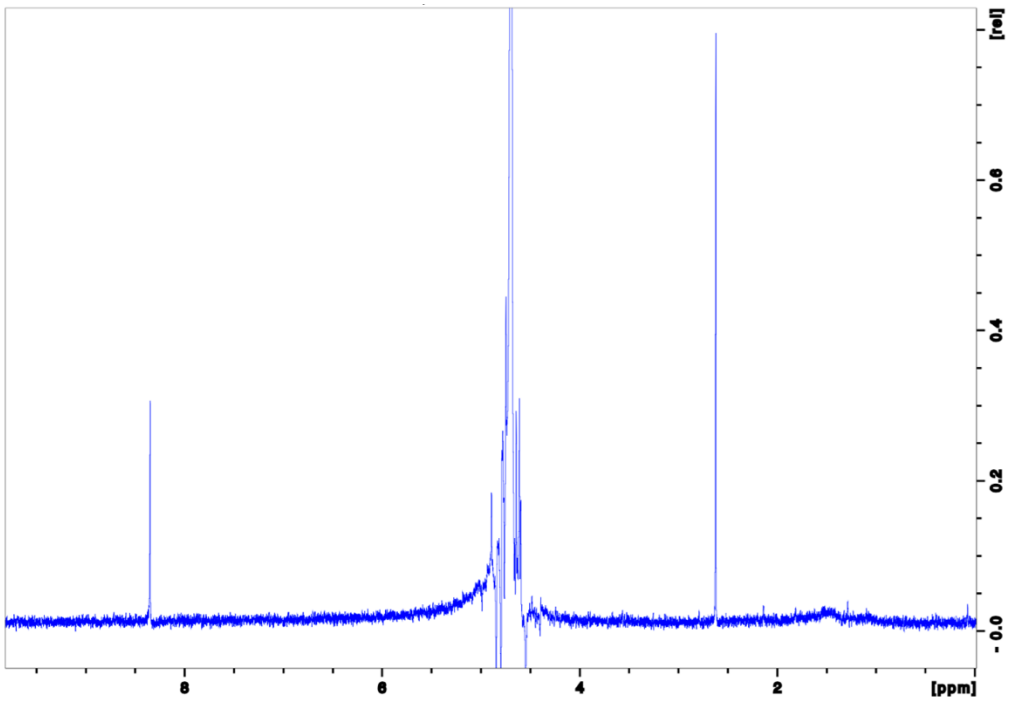

Figure A22. NMR trace of Cu/CA-400 obtained after electrolysis at -1.13 V for 2.5 hours. The peaks from left to right correspond to ^{1}H in $HCOO^{-}$, suppressed ^{1}H of water, and ^{1}H of DMSO.

A3 Tables

Table A1. Cu weight percent characterized by EDS and AA

	Cu/CA-180	Cu/CA-300	Cu/CA-400	Cu/CA-650
EDS	8.5 ± 0.5 wt %	7.7 ± 0.4 wt %	6.9 ± 0.6 wt %	7.7 ± 0.9 wt %
AA	9.7 ± 0.6 wt %	11 ± 0.6 wt %	7.8 ± 0.5 wt %	12 ± 0.7 wt %

Table A2. Calculated Electroactive Surface Area of Cu/CA Samples

	Cu/CA-180	Cu/CA-300	Cu/CA-400	Cu/CA-650
cm^2/mg_{Cu} by AA	15.5	12.5	15.2	12.8
$cm^2/mg_{Cu/CA}$	1.50	1.33	1.18	1.60

Table A3. Coordination Number (CN) of Cu_2O surface modeled from Cu K-edge EXAFS

	Cu/CA-180	Cu/CA-300	Cu/CA-400
Cu-O CN	1.62 ± 0.33	1.28 ± 0.28	2.28 ± 0.37
Cu-Cu CN	5.79 ± 0.69	6.16 ± 0.75	7.33 ± 0.72

Table A4. Nearest Neighbor Distances (NND, Å) model of Cu_2O surface from Cu K-edge EXAFS, showing a similar surface among samples.

	Cu/CA-180	Cu/CA-300	Cu/CA-400
Cu-O NND	1.85 ± 0.03	1.87 ± 0.03	1.87 ± 0.02
Cu-Cu NND	3.02 ± 0.03	3.06 ± 0.04	3.04 ± 0.03

Table A5. Percentage of ^{13}C gas product at potential -1.04 V on Cu/CA-400 via using $^{13}CO_2$ and $NaH^{13}CO_3$.

	CO	CH_4	C_2H_4	C_2H_6
^{13}C product percentage	94 %	100 %	96 %	100 %

Table A6. Errors in CO_2RR Current Efficiency

		Cu/CA-180	Cu/CA-300	Cu/CA-400	Cu/CA-650
-0.81 V	CO	0.055	0.095	0.069	0.020
	C_2H_4	0.008	0.008	0.011	n/a
	HCOOH	0.019	0.014	0.042	0.015
	H_2	0.083	0.051	0.130	0.032
-0.96 V	CO	0.063	0.097	0.005	0.024
	C_2H_4	0.022	0.028	0.008	0.015
	HCOOH	0.012	0.017	0.011	0.044
	H_2	0.092	0.125	0.047	0.065
-1.04 V	CO	0.046	0.094	0.061	0.016
	C_2H_4	0.024	0.023	0.029	0.012
	CH_4	0.068	0.018	0.021	0.027
	HCOOH	0.026	0.025	0.027	0.012
	H_2	0.096	0.099	0.089	0.077
-1.13 V	CO	0.007	0.034	0.054	0.016
	C_2H_4	0.038	0.015	0.025	0.007
	CH_4	0.036	0.025	0.045	0.024
	HCOOH	0.011	0.011	0.028	0.009
	H_2	0.114	0.035	0.090	0.036

Table A7. Comparison of this work to Cu supported on carbon on literature

Material	Size	Cu loading	Potential	CO_2RR efficiency	Reference
Cu/CA-400	330 nm	7.8 wt% (16.9 μg/cm^2)	-0.81 V vs. RHE	54 %	**This work**
20 wt% Cu/SWNT	19 nm	20 wt%	-1.4 V vs. Ag/AgCl*	<20 %**	ACS Catal. 2014, 4, 3682−3695
20 wt% Cu/VC	27 nm	20 wt%	-1.4 V vs. Ag/AgCl*	<5 %**	ACS Catal. 2014, 4, 3682−3695
40 wt% Cu/VC	12 nm	40 wt%	-1.4 V vs. Ag/AgCl*	<20%**	ACS Catal. 2014, 4, 3682−3695
Cu NP/GC	12 nm	9.69 μg/cm^2	-1.3 V vs. RHE	50 %	ACS Catal. 2016, 6, 202−209
Cu/N-doped graphene	39 nm	14.2 ca%	-0.8 V vs. RHE	47 %	ChemistrySelect 2016, 1,1–8

* held at pH 6.8, -1.4 V vs Ag/AgCl is roughly equal to -0.80 V vs. RHE
**determined for CO, C_2H_4, and CH_4. No liquid products were reported
***SWNT = single-walled carbon nanotube; VC = Vulcan; GC = glassy carbon

Appendix B

Supporting Information for Chapter 3: Non-Innocent Role of Porous Carbon Toward Enhancing C_{2-3} Products in Electroreduction of Carbon Dioxide

Table of Contents

B3 Tables

B1 Supplemental Experimental Conditions

B1.1 Materials

Resorcinol (99%), formaldehyde (37% w/w aqueous solution stabilized with 7-8% methanol), sodium carbonate (≥ 99.95%), Nafion solution (5% w/w in water and 1-propanol), and graphite rod counter electrode were purchased from Alfa Aesar. Reagent alcohol (94%-96% v/v), ethanol (200 proof, ≥99.9%), potassium bicarbonate (≥ 99.995%, metals basis), Cu foil (99.999%, metals basis), and dimethyl sulfoxide (≥ 99.9%) were purchased from Fisher Scientific. Gaseous hydrogen, methane (≥ 99.99%), ethylene (≥ 99.9%), carbon monoxide (≥ 99.9%), ethane (balanced in 95% carbon dioxide), and carbon dioxide (≥ 99.9%) were from Airgas. Vulcan XC 72R was from Cabot Corporation. Glassy carbon electrode (3 mm dia) and Ag/Ag/Cl reference electrode were from CH Instruments and BASi, respectively. The Pt counter electrode (≥99.9%) was purchased from uGems.

B1.2 General Instrumentation

The morphology and composition of CA was characterized by a JSM-IT200 InTouchScope SEM and FEI Tecnai TF-30 300kV TEM. The Brunauer–Emmett–Teller (BET) surface area and pore-size distribution were characterized by Micromeritics ASAP 2020 Plus instrument. The surface of Cu/CA was characterized by a PHI 5600 X-ray Photoelectron Microscopy (XPS) using Mg Kα X-ray (1253.6 eV) radiation. All electrochemistry measurements were conducted on an Ivium-n-STAT Multichannel Electrochemical Analyzer.

B2 Figures

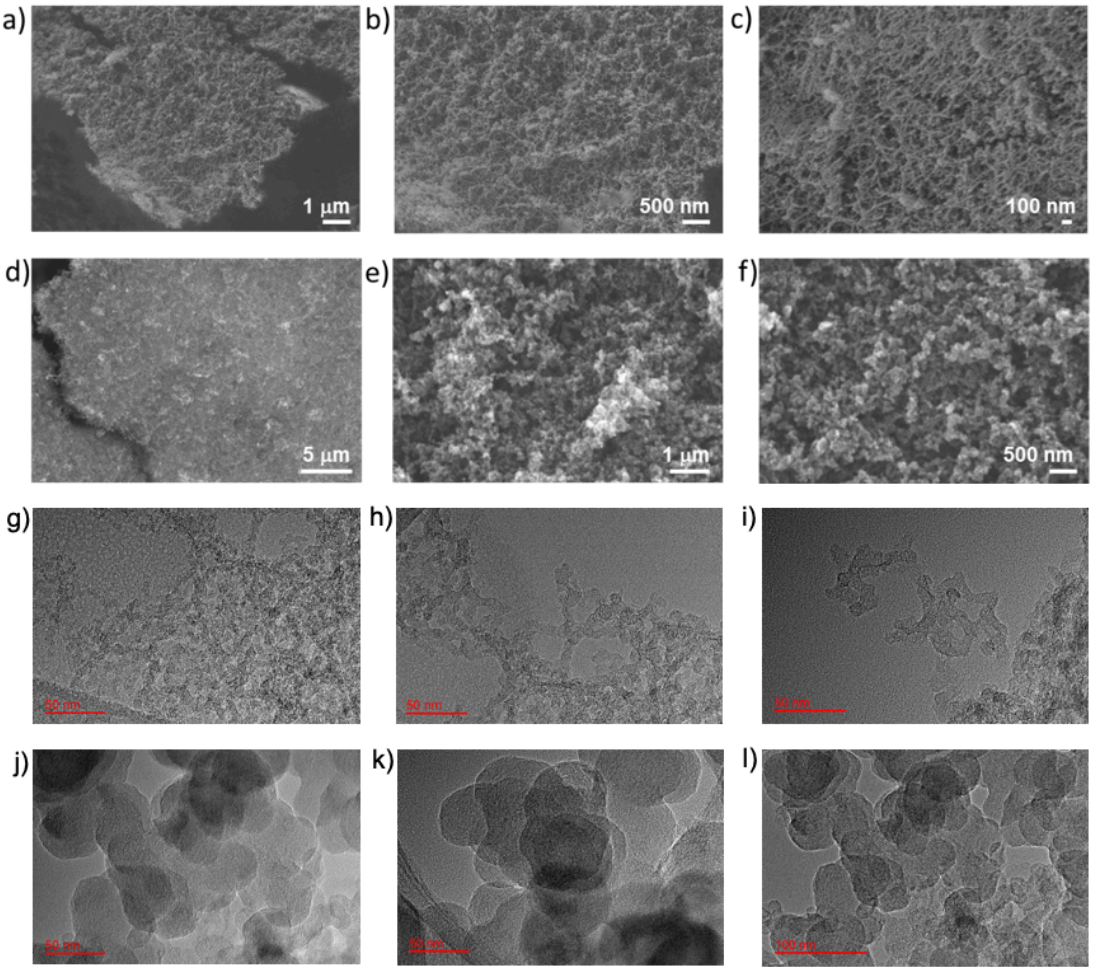

Figure B1. Additional SEM images and TEM of (a-c, g-i) CA and (d-f, j-l) VXC.

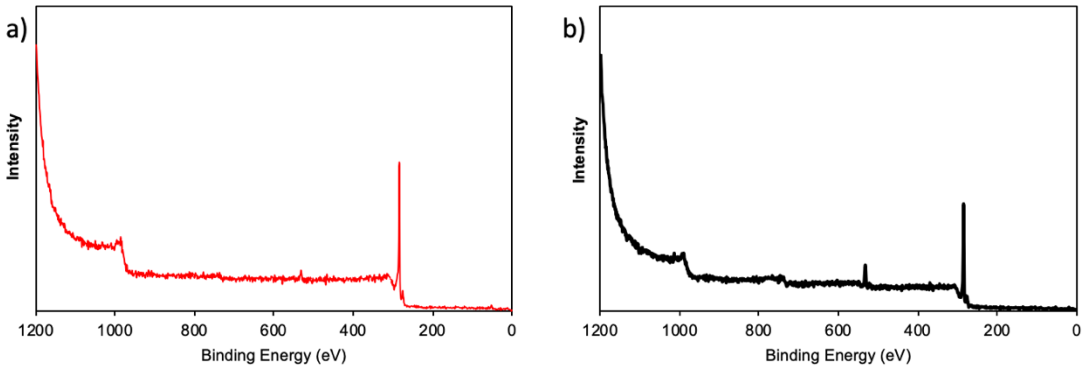

Figure B2. XPS survey scan of a) CA, and b) VXC.

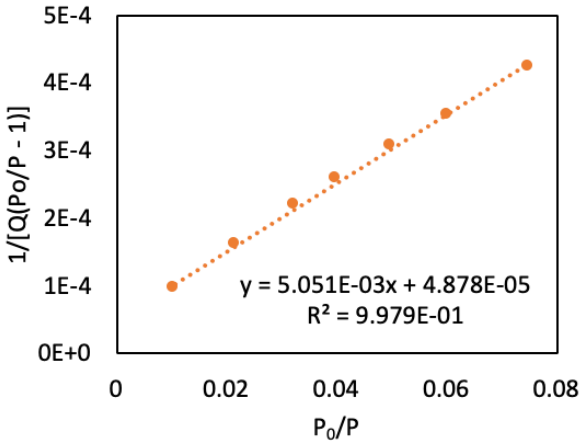

Figure B3. BET on CA layer with Nafion.

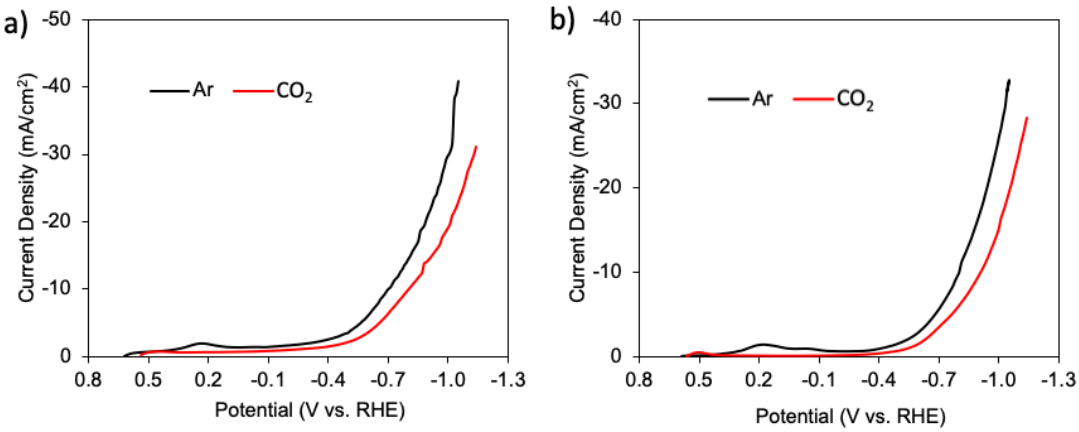

Figure B4. LSV of a) CA-Cu and b) VXC-Cu under Ar and CO_2.

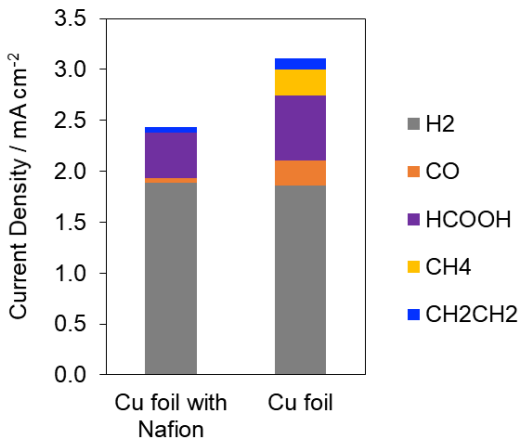

Figure B5. Comparison of specific current density for Cu foil and Cu foil covered with a Nafion membrane (without carbon) at 0.92 V vs. RHE in 0.1 M $KHCO_3$ under a CO_2 atmosphere.

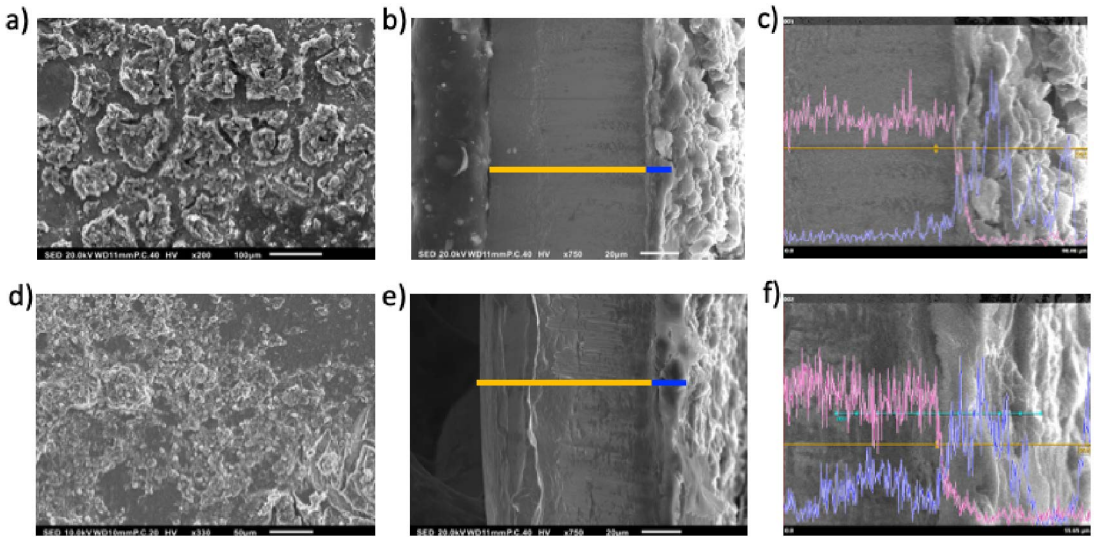

Figure B6. SEM images of (a-c) CA-Cu and (d-f) VXC-Cu after electrolysis. (a,d) Top-down view. (b,e) Cross-sectional view, showing a thickness of roughly 10 μm. (c,f) EDS line scan of Cu (pink) and C (blue) signals.

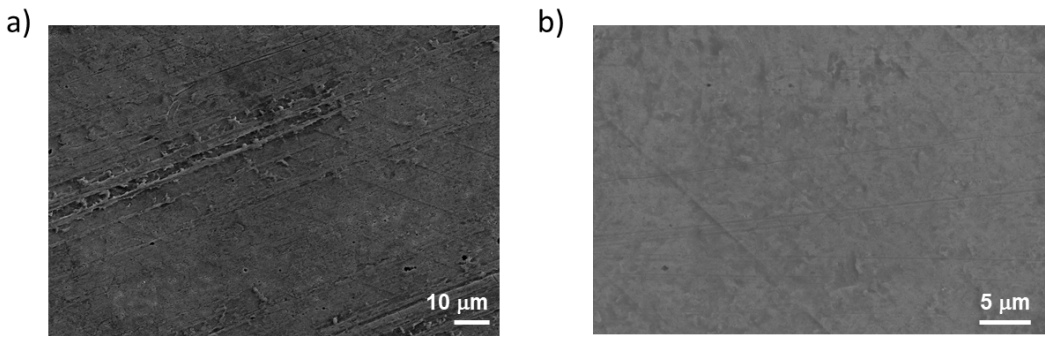

Figure B7. Comparison of SEM images of unmodified Cu foil (a) before and (b) after a 2-h electrolysis at -0.92 V vs RHE.

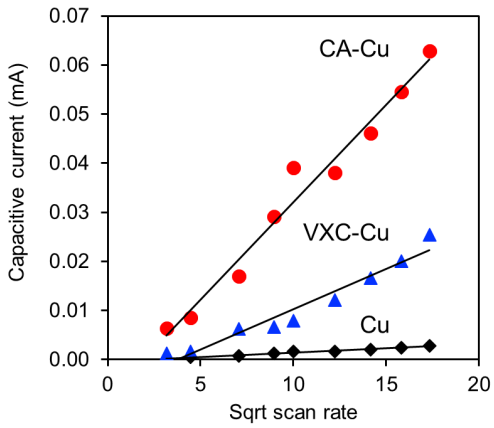

Figures S8. Surface roughness measurements of CA-Cu (red circles), VXC-Cu (blue triangle), and Cu foil (black diamonds) after electrolysis at -0.98 V for 2 hours. A surface roughness ratio of 22:9:1 was obtained for CA-Cu : VXC-Cu : Cu foil.

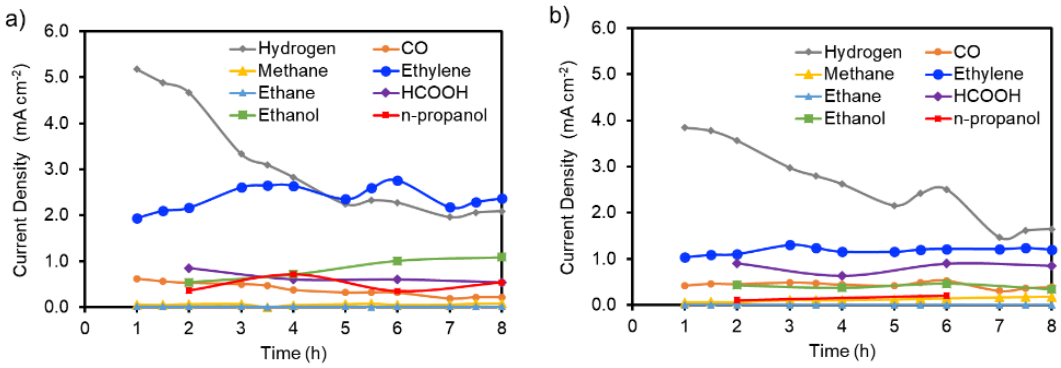

Figure B9. Partial current densities for (a) CA-Cu and (b) VXC-Cu during extended controlled potential electrolysis at -0.98 V vs RHE. Conditions: 0.1 M $KHCO_3$, pH 6.8, CO_2

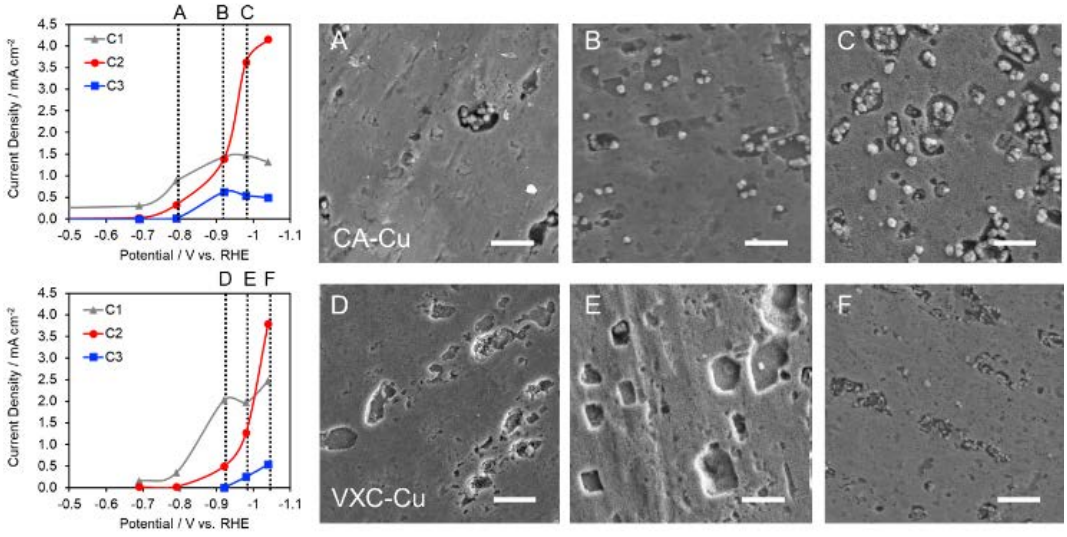

Figure B10. Specific current densities for C1, C2, and C3 products and the corresponding SEM images of the Cu morphology for CA-Cu (top row) and VXC-Cu (bottom row) after a 2-h electrolysis at various potentials. The letter designation of each micrograph corresponds with to a point in the current density versus potential graph shown on the left column. Scale bar = 5 μm.

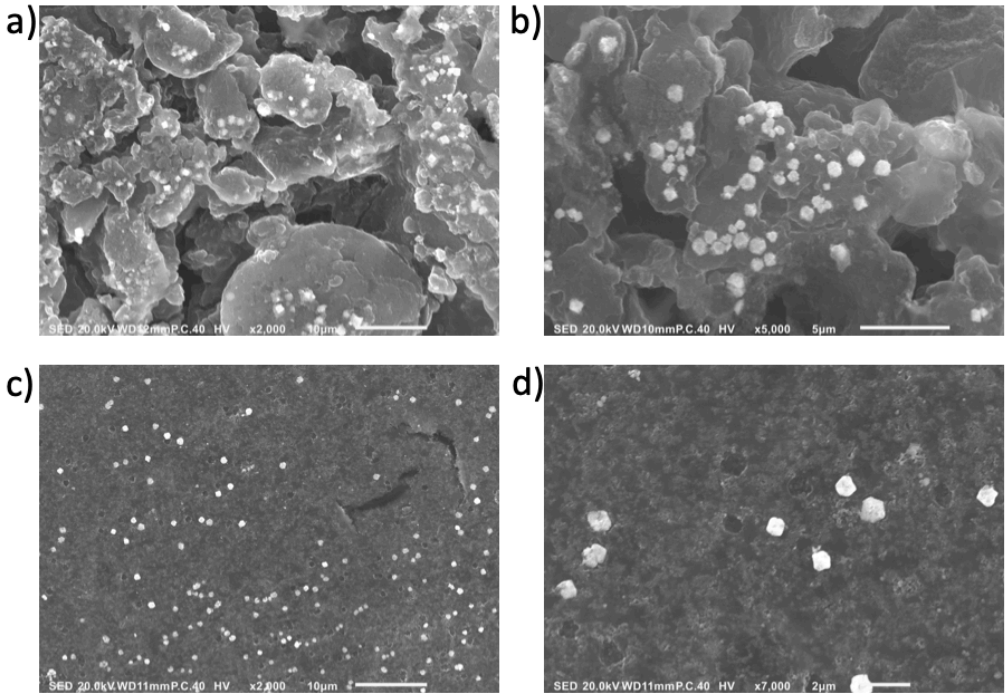

Figure B11. SEM images of CA (a, b), and VXC (c, d) lifted off the Cu foil. The surfaces in contact with Cu are facing up.

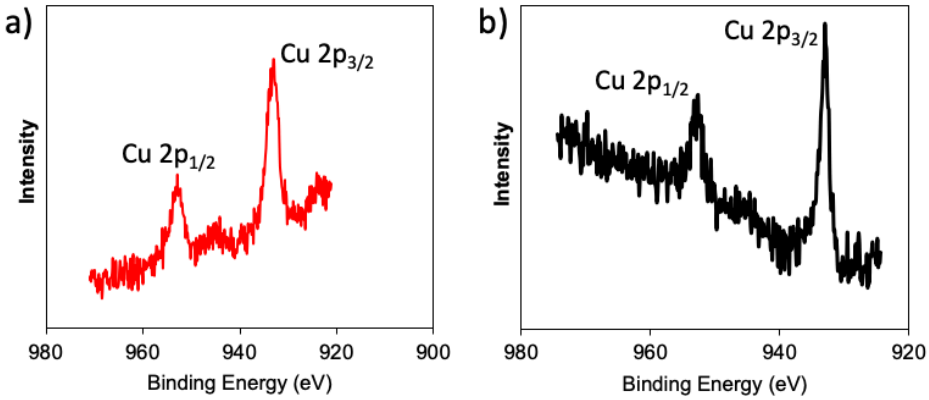

Figure B12. XPS on carbon modifier lifted off the Cu foil of a) CA-Cu, and b) VXC-Cu.

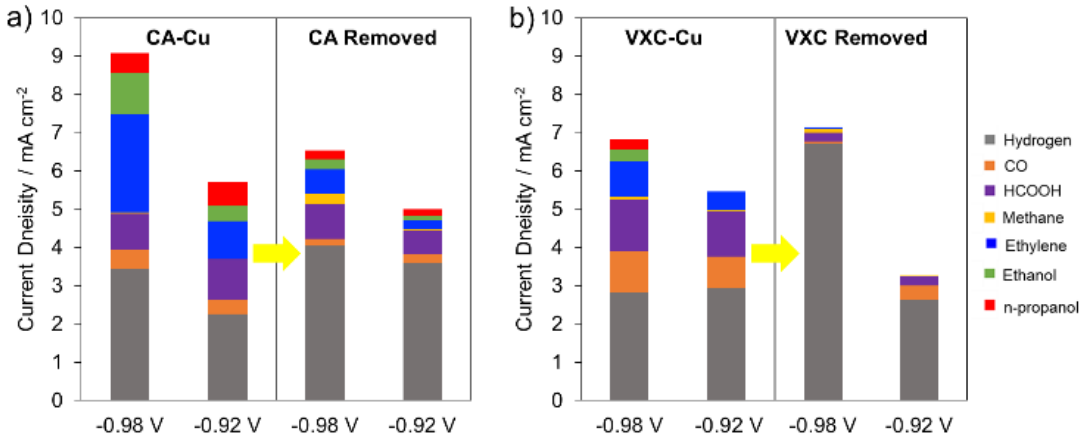

Figure B13. Specific current densities for (a) CA-Cu and (b) VXC-Cu before and after removal of the carbon modifier. Selectivity for C2 and C3 product decreases significantly after removing the carbon layer for both CA-Cu and VXC-Cu. Conditions: 0.1 M $KHCO_3$, pH 6.8, CO_2

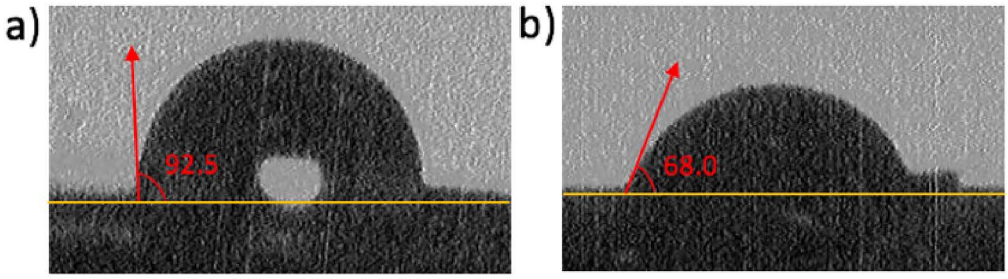

Figure B14. Contact angle measurement of a water droplet on top of (a) CA-Cu, and (b) VXC-Cu.

B3 Tables

Table B1. Elemental Fraction Obtained from XPS.

	C	O
CA	97.3 %	2.7 %
VXC	90.2 %	9.8 %

Table B2. Percent incorporation of ^{13}C in gaseous carbon products using isotopically labeled $^{13}CO_2$ and $KH^{13}CO_3$ by GC-MS at -0.96 V vs. RHE after CPE for 2000 s.

	CO	CH_4	C_2H_4	C_2H_6
^{13}C product percentage	92 %	94 %	100 %	100 %

Table B3. C_{2-3} Product Selectivity on different surface modified Cu catalysts for CO_2RR.

Catalyst	Electrolyte	Potential (vs. RHE)	FE (C_{2-3})	Reference
CA-Cu	**0.1 M $KHCO_3$**	**-0.98 V**	**45%**	**This work**
O_2 plasma modified dendrite Cu/Ag	0.1 M $KHCO_3$	-0.9 V	~44%	10.1021/acscatal.9b00483
Glycine modified Cu foil	0.1 M $KHCO_3$	-1.3 V	~34%	10.1039/C5EE03694A
N-tolylpyridinium chloride modified Cu foil	0.1 M $KHCO_3$	-1.09 V	~75%	10.1021/acscentsci.7b00180
$PdCl_2$ modified Cu_2O-derived Cu	0.1 M $KHCO_3$	-1.0 V	~40%	10.1021/acs.jpcc.5b09144
Pd-decorated Cu	0.5 M $KHCO_3$	-0.96 V	7%-11% (C_2H_4)	10.1002/anie.201707478
Benzimidazole-functionalized Cu foil	0.1 M $KHCO_3$	-1.01 V	30%	10.1039/C8CC04735A
Poly(acrylamide) modified Cu foam	0.1 M $NaHCO_3$	-0.96 V	~31%	10.1021/acscatal.7b04347

Appendix C

Supporting Information for Chapter 4: Strategic design of MoO_2 nanoparticles supported by carbon nanowires for enhanced electrocatalytic nitrogen reduction

Table of Contents

Figure C11. Indophenol blue assay of NH_3 concentration following bulk electrolysis with MoO_2/C nanowires.

Figure C12. N_2H_4 detection following bulk electrolysis with MoO_2/C NWs showing negligible N_2H_4 production.

Figure C13. Current density and yield rate as a function of potential.

Figure C14. Control experiments for electrolysis of bare carbon paper under continuous flow N_2 (CP (N_2)), MoO_2/C on carbon paper under continuous flow Ar (MoO_2/CP (Ar)) and MoO_2/C on carbon paper with continuous flow N_2.

Figure C15. PXRD spectra of MoO_2/C nanowires after 3 h of electrolysis at -0.1 V vs. RHE, showing negligible change.

Figure C16. SEM of MoO_2/C post-electrolysis for 3 h in 0.1 M HCl at a constant potential of -0.1 V vs. RHE.

Figure C17. Characterization of the unsupported MoO_2 particles, (a) X-ray Diffraction and (b) SEM.

Figure C18. Electrochemical impedance spectroscopy (EIS) of the MoO_2/C and unsupported MoO_2 materials in 0.1 M HCl.

C3 Tables

Table C1. EXAFS fitting results.

Table C2. Structural parameters from PDF refinement of the HE-XRD data for MoO_2 at Room Temperature.

C4 References

C1 Supplemental Experimental Conditions

C1.1 Materials

[$(NH_4)_6Mo_7O_{24}\cdot 4H_2O$] was purchased from Strem chemicals. Trace metal grade HCl was purchased from Fisher Scientific. Carbon paper electrodes (5% hydrophobic coating) were purchased from Fuel Cell Earth. Aniline ($C_6H_5NH_2$), sodium hydroxide (NaOH), hydrazine dihydrochloride ($N_2H_4\cdot 2HCl$), and p-dimethylaminobenzaldehyde ($C_9H_{11}NO$) were purchased from Sigma Aldrich. Salicylic Acid ($C_7H_6O_{3)}$, sodium nitroferricyanide·dihydrate ($C_5FeN_6Na_2O\cdot 2H_2O$), sodium hypochlorite (NaClO), and trisodium citrate ($C_6H_5Na_3O_7\cdot 2H2O$) were purchased from Alfa Aesar. Ultra-High Purity gases (Ar and N_2) were purchased from Airgas. Ag/AgCl reference electrode was purchased from BASi.

C1.2 General Instrumentation

The morphology and composition of materials were characterized by a JSM-IT200 InTouchScope SEM and FEI Tecnai TF-30 300 kV TEM. Powder XRD was done on a Bruker D8 Focus diffractometer, with Cu Kα source and LynxEye detector. All electrochemistry measurements were conducted on an Ivium-n-STAT Multichannel Electrochemical Analyzer. XPS data were measured on a PHI 5600 instrument using monochromatic Al Kα radiation. Post-electrolysis XPS was done on the same type of instrument but using Mg Kα (1253.6 eV) radiation. Electron Paramagnetic Resonance (EPR) spectroscopy on a Bruker EMX-plus X-Band EPR spectrometer.

C1.3 Materials Characterization

X-ray absorption spectroscopy (XAS) measurements were performed at the 10-ID-B beamline of the Advanced Photon Source (APS), Argonne National Laboratory (ANL). Precursor materials and MoO_2 nanoparticles were loaded into 1 mm outer diameter Kapton capillaries probed from -200 eV below the Mo K-edge (20.0 keV) to ~800 eV above the edge in a transmission geometry. All data reduction, averaging and subsequent EXAFS modeling was done using the Demeter software package.[1] EXAFS modeling of MoO_2 nanoparticles used Mo-O and Mo-Mo scattering paths from a known monoclinic MoO_2 model crystal structure[2] while also including similar scattering paths to account for Mo^{5+} contributions using a monoclinic Mo_8O_{23} structure from the Materials Project.[3] A value of 0.843 was used for S_0^2 in the EXAFS modeling, which was obtained by modeling the EXAFS of a reference Mo foil.

High-energy X-ray diffraction (HE-XRD) was performed at the 11-ID-B beamline of the APS. MoO_2 nanoparticles were loaded into a 1 mm outer diameter Kapton capillaries and examined using 86.58 keV x-rays. A sample to detector distance of ~220 mm was used to obtain a Q_{max} of ~32 $Å^{-1}$. HE-XRD to pair distribution function analysis (PDF) conversion was performed using the program RAD[4] while crystallographic fitting was performed using PDFgui[5] and a monoclinic MoO_2 model crystal structure.[2]

X-ray photoelectron spectroscopy (XPS) setup was calibrated with Au metal, which was cleaned via Ar-ion sputtering. The raw atomic concentration has a 5%

error due to surface inhomogeneities, surface roughness, literature sensitivity values for peak integration, *etc*. The powders were pressed onto carbon tape that was used to make electrical contact to the spectrometer. Post-electrolysis XPS sample was prepared by scratching off the materials from electrode after 3 h of electrolysis at -0.1 V vs. RHE. Adequate amount of sample ensured a full coverage of the carbon tape substrate.

Electron pair resonance (EPR) measurements were conducted at 9.42 GHz (X-band) on a Bruker EMXplus X-Band EPR spectrometer. The microwave power was set to 2 mW, the modulation amplitude was set to 5G and the temperature was 120 K.

C2 Figures

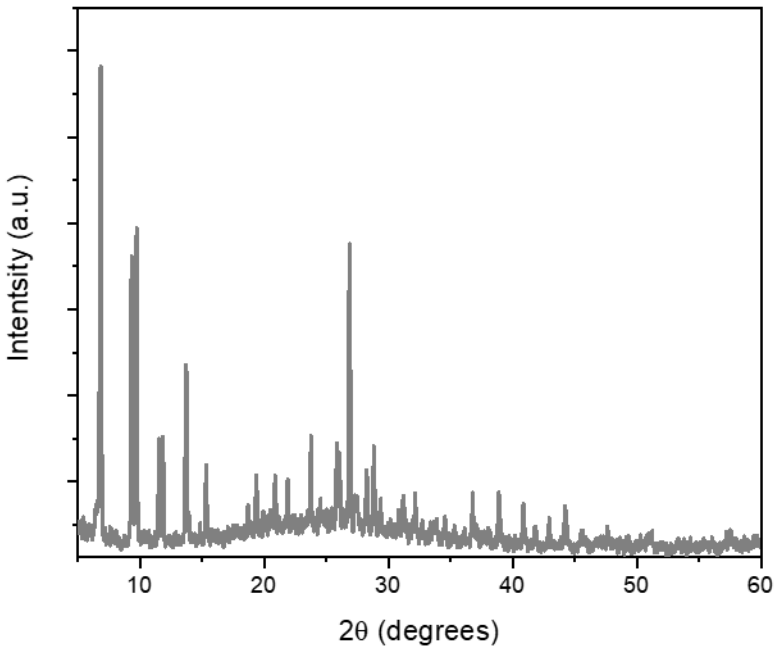

Figure C1. PXRD of anilinium molybdate nanowire precursor.

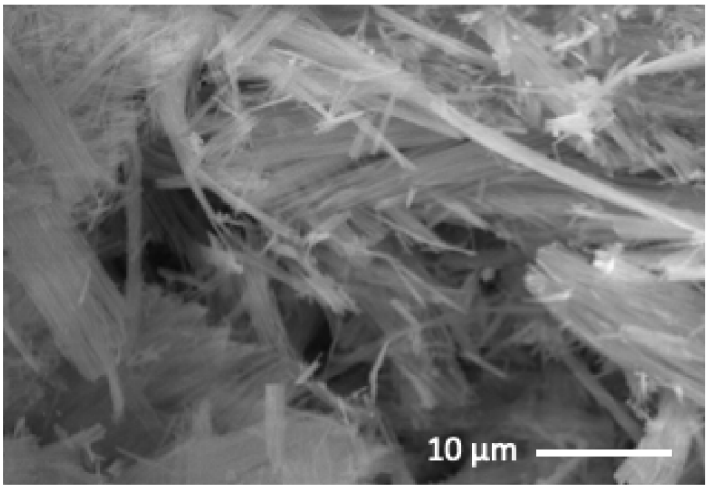

Figure C2. SEM of anilinium molybdate nanowire precursor.

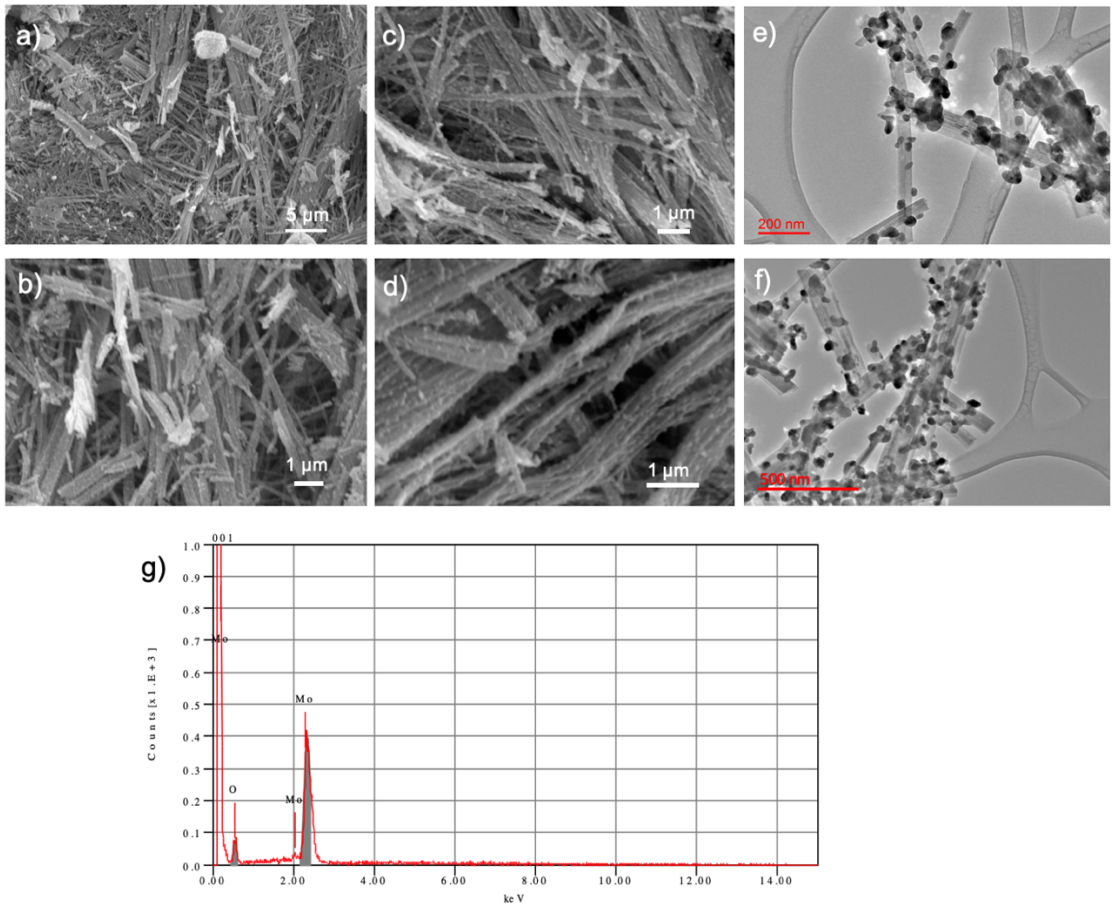

Figure C3. Additional SEM (a-d), TEM (e,f) images at different magnifications and EDS (g) of MoO_2/C nanowires. Atomic ratio was determined by EDS peak areas and was reported in the main text based on the average of three separate measurements.

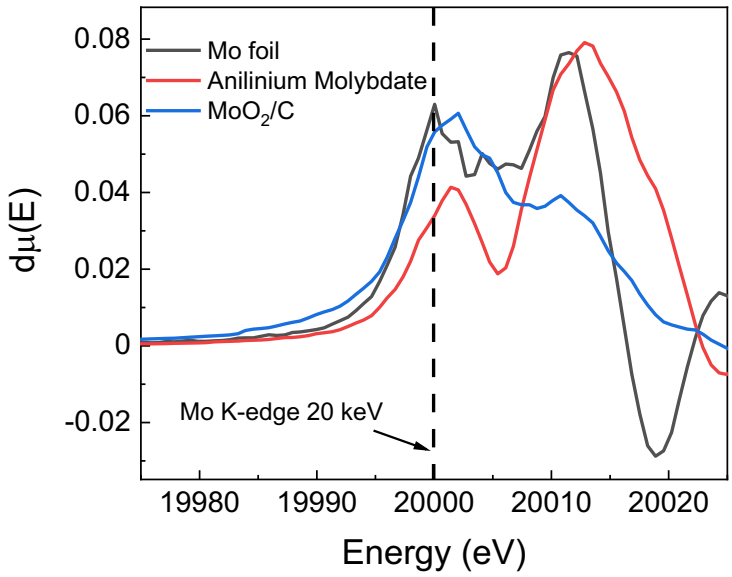

Figure C4. Experimental first-order derivation XANES.

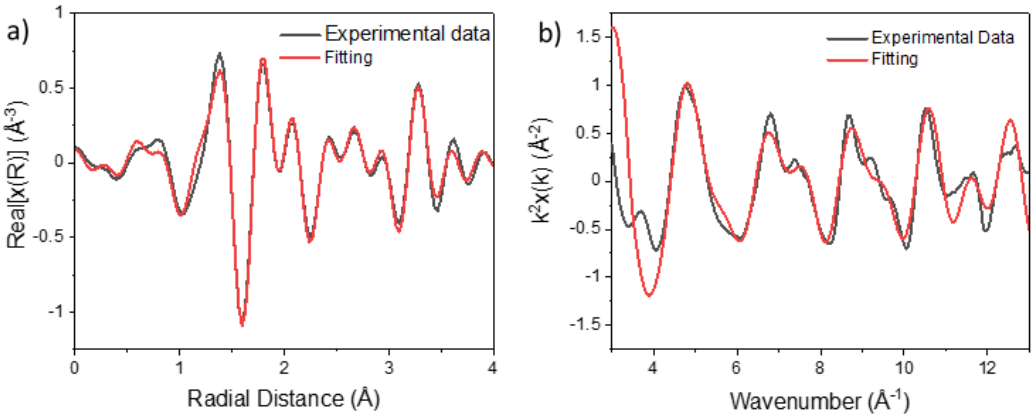

Figure C5. Mo *K*-edge EXAFS fitting results for (a) real r-space and (b) k^2-space.

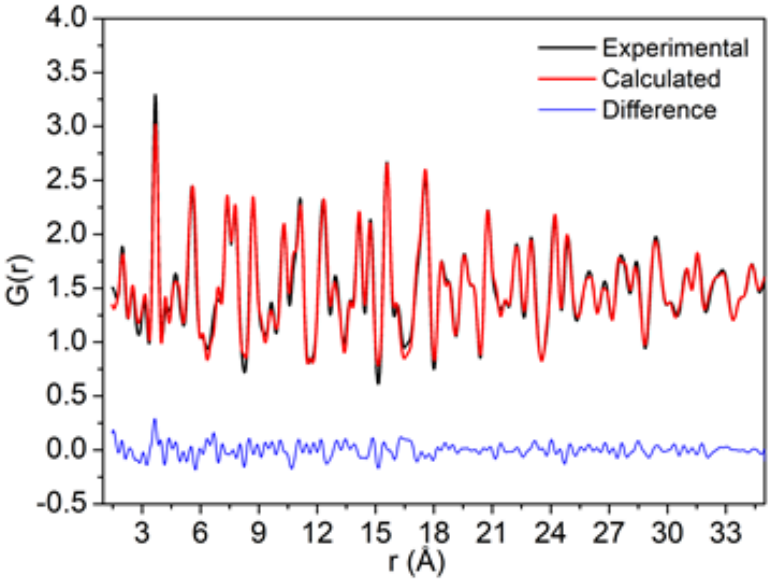

Figure C6. Crystallographic fitting of the atomic PDF data for MoO_2/C.

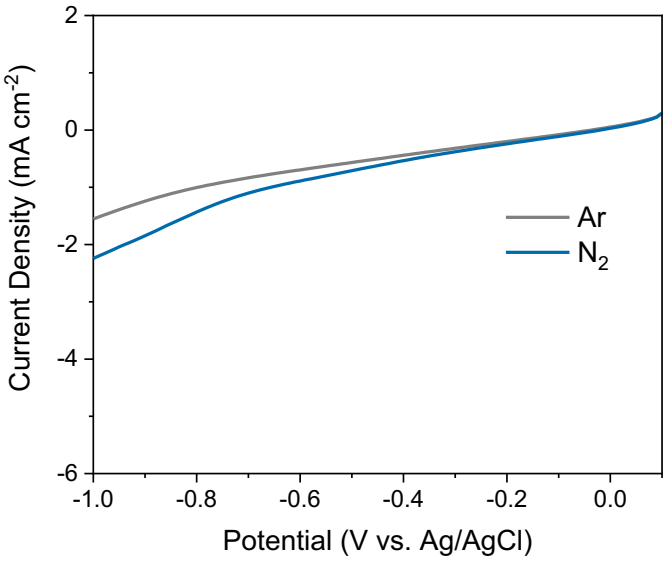

Figure C7. Polarization curves of MoO_2/C on carbon paper under N_2 and Ar. Scanned from 0.1 to -1.1 at a scan rate of 50 mV/s in 0.1 M HCl.

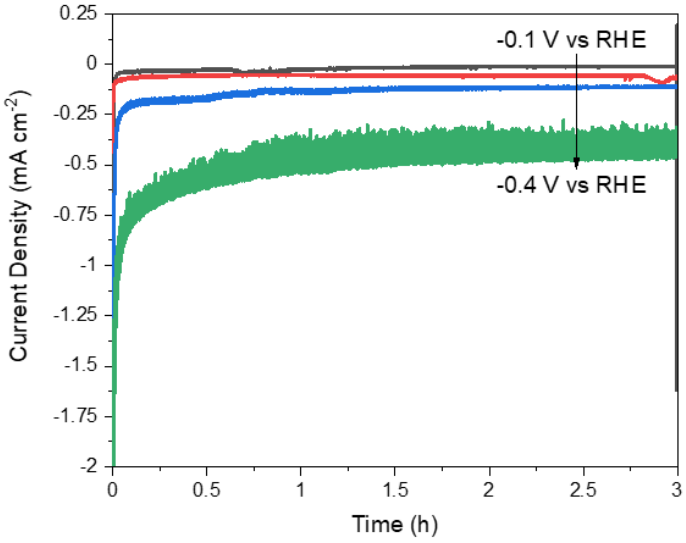

Figure C8. Chronoamperometry curves during bulk electrolysis with MoO_2/C NWs (E = -0.1, -0.2, -0.3, -0.4 vs. RHE). CPE conditions: 0.1 M HCl (pH = 1.0), 3 h.

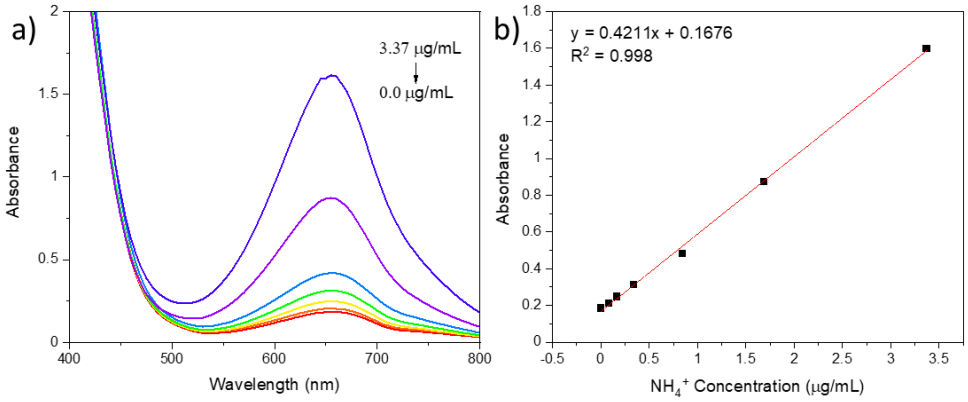

Figure C9. (a) UV-Vis spectra of indophenol blue assays for NH_3 calibration and (b) linear fit of the absorbance maximum at 655 nm as a function of NH_3 concentration.

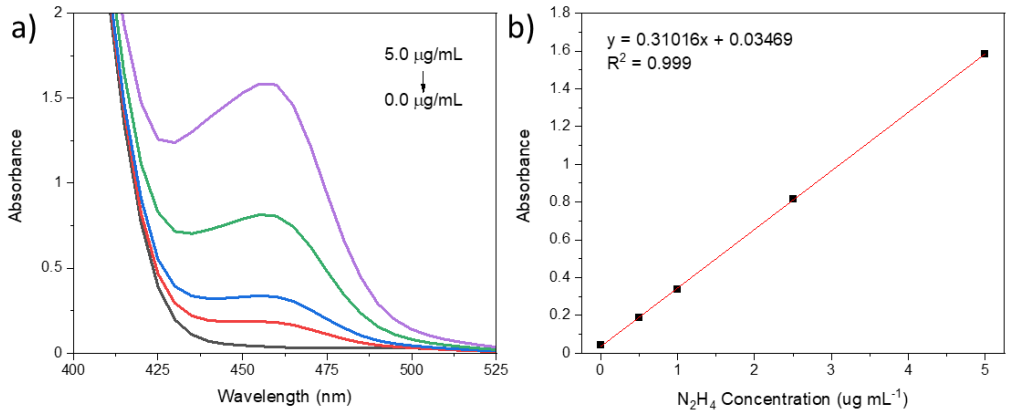

Figure C10. (a) UV-Vis spectra for N_2H_4 calibration using the Watt and Chrisp method. (b) Linear fit of the absorbance maximum at 460 nm as a function of N_2H_4 concentration.

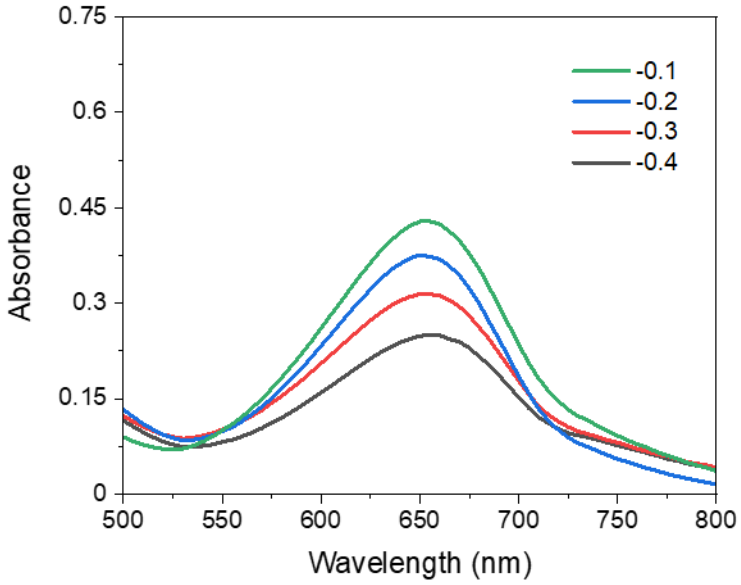

Figure C11. Indophenol blue assay of NH_3 concentration following bulk electrolysis with MoO_2/C nanowires at -0.1, -0.2, -0.3, and -0.4 V vs. RHE for 3 hours.

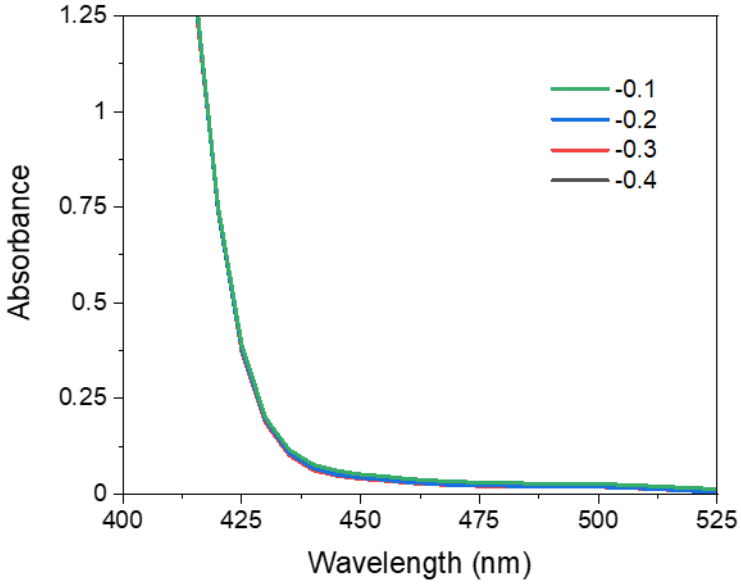

Figure C12. N_2H_4 detection following bulk electrolysis with MoO_2/C NWs at -0.1, -0.2, -0.3, and -0.4 V vs. RHE, 3 h, showing negligible N_2H_4 production.

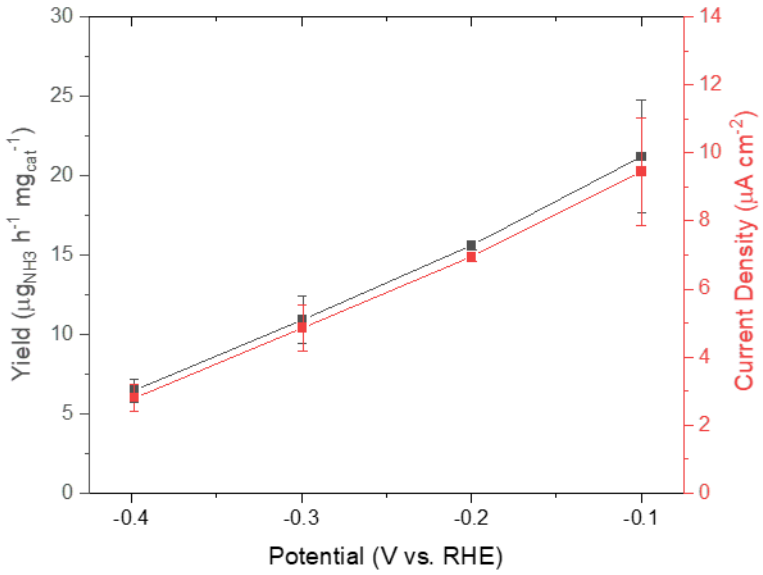

Figure C13. Current density and yield rate as a function of potential. CPE Conditions: -0.1 to -0.4 E vs. RHE, in 0.1 M HCl for 3 hours.

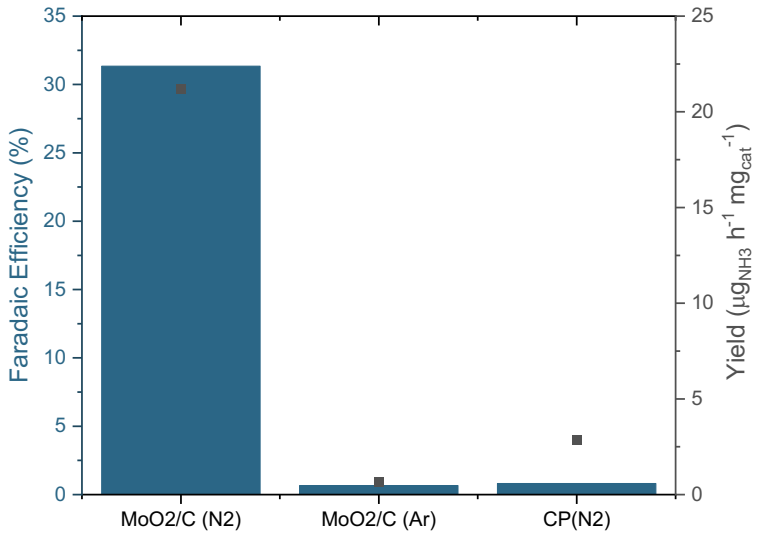

Figure C14: Control experiments for electrolysis of bare carbon paper under continuous flow N_2 MoO_2/C on carbon paper (MoO_2/C (N2)), under continuous flow Ar (MoO_2/CP (Ar)) and carbon paper with continuous flow N_2. (All controls were performed at -0.1 V vs RHE for 3 h).

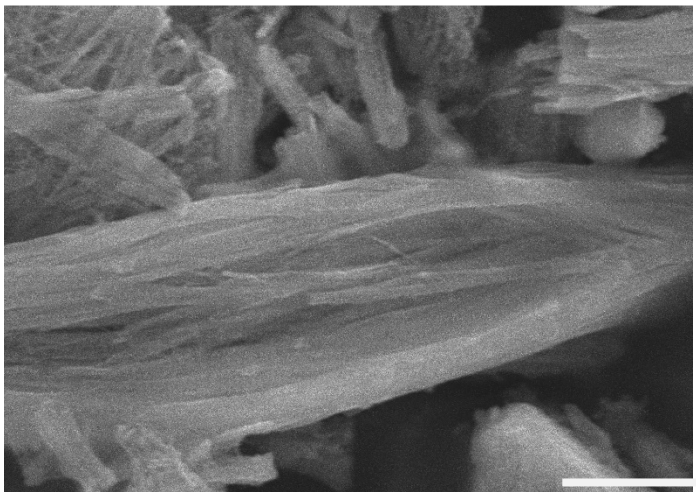

Figure C15. SEM of MoO_2/C post-electrolysis for 3 h in 0.1 M HCl at a constant pote

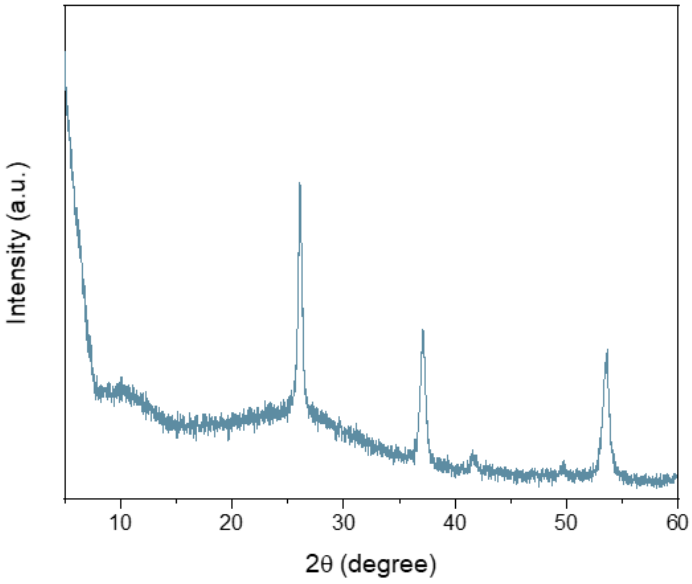

Figu).1 V vs. RHE, showing negligible change.

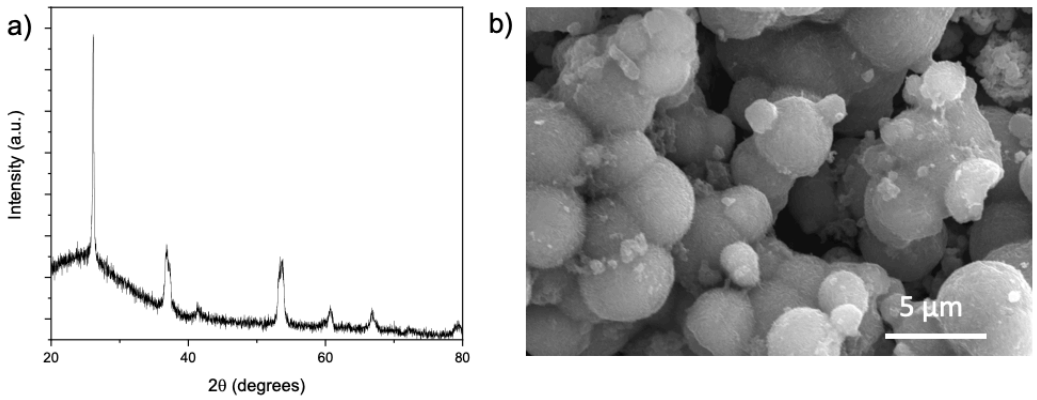

Figure C17. Characterization of the unsupported MoO_2 particles, (a) X-ray Diffraction and (b) SEM.

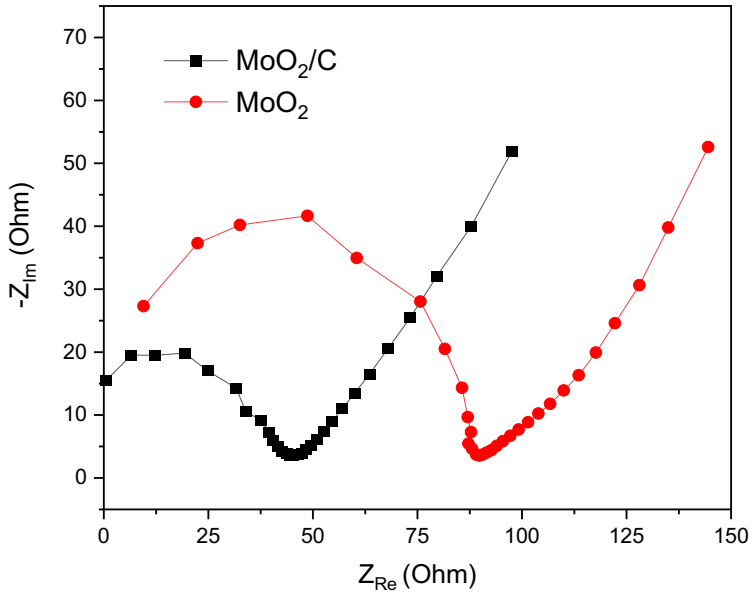

Figure C18. Electrochemical impedance spectroscopy (EIS) of the MoO_2/C and unsupported MoO_2 particles in 0.1 M HCl.

C3 Tables

Table C1. EXAFS fitting results

Contribution	Mo-O CN	Mo-O NND (Å)	Mo-O σ^2	Mo-Mo CN	Mo-Mo NND (Å)	Mo-Mo σ^2
MoO_2	4.53 ± 0.38	2.072 ± 0.006	0.002 ± 0.001	2.76 ± 0.52	2.92 ± 0.03	0.002 ± 0.001
Mo_8O_{23}	3.77 ± 0.33	2.32 ± 0.01	0.002 ± 0.001	2.07 ± 0.38	3.44 ± 0.01	0.002 ± 0.001

Table C2. Structural parameters from PDF refinement of the HE-XRD data for MoO_2 at Room Temperature

MoO_2 (Monoclinic $P2_1/c$)
a (Å) = 5.6097 (7)
b (Å) = 4.8422 (6)
c (Å) = 5.6098 (3)
β (degrees) = 120.72 (8)
R_w= 0.163

	U_{11} (Å^2)	U_{22} (Å^2)	U_{33} (Å^2)	U_{12} (Å^2)	U_{13} (Å^2)	U_{23} (Å^2)
Mo	0.008 (1)	0.0094 (1)	0.0082 (6)	0.0009 (6)	0.0033 (6)	-0.0004 (5)
O(1)	0.029 (11)	0.029 (12)	0.0086 (12)	-0.0019 (8)	-0.0048 (9)	-0.0025 (10)
O(2)	0.028 (14)	0.0023 (13)	0.031 (15)	0.003 (11)	0.084 (12)	0.0028 (13)

Table C3. Electrochemical NRR performance of different Mo catalysts

Catalyst	Electrolyte	Potential (vs. RHE)	Yield	FE (%)	Reference
MoO_2/C	0.1 M HCl	-0.1 V	21.2 μg h^{-1} mg^{-1} 3.26 ×10^{-11} mol·s^{-1} ·cm^{-2} 2.13 μg h^{-1} cm^{-2}	31.3	This Work
MoC@NC-800	1.0 mM HCl + 0.5 M Li_2SO_4	-0.35 V	22.5 μg h^{-1} mg^{-1}	25.1	6
Mo/Mo_xC	0.1 M Na_2SO_4	-0.2, -0.3 V	20.4 μg h^{-1} mg^{-1} (-0.3 V)	18.9 (-0.2 V)	7
MoN	0.1 M HCl	-0.3 V	3.01×10^{-10} mol·s^{-1} ·cm^{-2}	1.15	8
MoS_2	0.1 M Na_2SO_4	-0.5 V	4.94 μg h^{-1} cm^{-2}	1.17	9
MoO_3	0.1 M HCl	-0.4 V	29.43 μg h^{-1} mg^{-1}	1.9	10
Mo_2N	0.1 M HCl	-0.3 V	78.4 μg h^{-1} mg^{-1}	4.5	11
Mo Film	0.5 H_2SO_4	-0.49 V	3.09×10^{-10} mol·s^{-1} ·cm^{-2}	0.72	12
Mo_2C/GCE	0.1 M HCl	-0.3 V	95.1 μg h^{-1} mg^{-1}	8.13	13
Atomically dispersed Mo	0.1 M KOH	-0.3 V	34.6 μg h^{-1} mg^{-1}	14.6	14

Table C4. XPS surface Mo atomic ratio comparison before and after electrolysis

Surface Mo atomic ratio	Mo(IV)	Mo(V)	Mo(VI)
Pre-electrolysis	0.17	0.20	0.63
Post-electrolysis	0.12	0.41	0.47

C4 References

(1) Ravel, B.; Newville, M. ATHENA, ARTEMIS, HEPHAESTUS: Data Analysis for X-Ray Absorption Spectroscopy Using IFEFFIT. *J. Synchrotron Radiat.* **2005**, *12* (4), 537–541. https://doi.org/10.1107/S0909049505012719.

(2) Bolzan, A. A.; Kennedy, B. J.; Howard, C. J. Neutron Powder Diffraction Study of Molybdenum and Tungsten Dioxides. *Aust. J. Chem.* **1995**, *48* (8), 1473–1477. https://doi.org/10.1071/CH9951473.

(3) Jain, A.; Ong, S. P.; Hautier, G.; Chen, W.; Richards, W. D.; Dacek, S.; Cholia, S.; Gunter, D.; Skinner, D.; Ceder, G.; Persson, K. A. Commentary: The Materials Project: A Materials Genome Approach to Accelerating Materials Innovation. *APL Mater.* **2013**, *1* (1). https://doi.org/10.1063/1.4812323.

(4) Petkov, V. RAD, a Program for Analysis of X-Ray Diffraction Data from Amorphous Materials for Personal Computers . *J. Appl. Crystallogr.* **1989**, *22* (4), 387–389. https://doi.org/10.1107/s0021889889002104.

(5) Farrow, C. L.; Juhas, P.; Liu, J. W.; Bryndin, D.; Boin, E. S.; Bloch, J.; Proffen, T.; Billinge, S. J. L. PDFfit2 and PDFgui: Computer Programs for Studying Nanostructure in Crystals. *J. Phys. Condens. Matter* **2007**, *19* (33). https://doi.org/10.1088/0953-8984/19/33/335219.

(6) Qu, X.; Shen, L.; Mao, Y.; Lin, J.; Li, Y.; Li, G.; Zhang, Y.; Jiang, Y.; Sun, S. Facile Preparation of Carbon Shells-Coated O-Doped Molybdenum

Carbide Nanoparticles as High Selective Electrocatalysts for Nitrogen Reduction Reaction under Ambient Conditions. *ACS Appl. Mater. Interfaces* **2019**, *11* (35), 31869–31877. https://doi.org/10.1021/acsami.9b09007.

(7) Liu, Y.; Zhu, X.; Zhang, Q.; Tang, T.; Zhang, Y.; Gu, L.; Li, Y.; Bao, J.; Dai, Z.; Hu, J.-S. Engineering Mo/Mo_2C/MoC Hetero-Interfaces for Enhanced Electrocatalytic Nitrogen Reduction. *J. Mater. Chem. A* **2020**, *8* (18), 8920–8926. https://doi.org/10.1039/d0ta03290e.

(8) Zhang, L.; Ji, X.; Ren, X.; Luo, Y.; Shi, X.; Asiri, A. M.; Zheng, B.; Sun, X. Efficient Electrochemical N_2 Reduction to NH_3 on MoN Nanosheets Array under Ambient Conditions. *ACS Sustain. Chem. Eng.* **2018**, *6* (8), 9550–9554. https://doi.org/10.1021/acssuschemeng.8b01438.

(9) Zhang, L.; Ji, X.; Ren, X.; Ma, Y.; Shi, X.; Tian, Z.; Asiri, A. M.; Chen, L.; Tang, B.; Sun, X. Electrochemical Ammonia Synthesis via Nitrogen Reduction Reaction on a MoS_2 Catalyst: Theoretical and Experimental Studies. *Adv. Mater.* **2018**, *30* (28), 2–7. https://doi.org/10.1002/adma.201800191.

(10) Han, J.; Ji, X.; Ren, X.; Cui, G.; Li, L.; Xie, F.; Wang, H.; Li, B.; Sun, X. MoO_3 Nanosheets for Efficient Electrocatalytic N_2 Fixation to NH_3. *J. Mater. Chem. A* **2018**, *6* (27), 12974–12977. https://doi.org/10.1039/c8ta03974g.

(11) Ren, X.; Cui, G.; Chen, L.; Xie, F.; Wei, Q.; Tian, Z.; Sun, X. Electrochemical N_2 Fixation to NH_3 under Ambient Conditions: Mo_2N

Nanorod as a Highly Efficient and Selective Catalyst. *Chem. Commun.* **2018**, *54* (61), 8474–8477. https://doi.org/10.1039/c8cc03627f.

(12) Yang, D.; Chen, T.; Wang, Z. Electrochemical Reduction of Aqueous Nitrogen (N_2) at a Low Overpotential on (110)-Oriented Mo Nanofilm. *J. Mater. Chem. A* **2017**, *5* (36), 18967–18971. https://doi.org/10.1039/c7ta06139k.

(13) Ren, X.; Zhao, J.; Wei, Q.; Ma, Y.; Guo, H.; Liu, Q.; Wang, Y.; Cui, G.; Asiri, A. M.; Li, B.; Tang, B.; Sun, X. High-Performance N_2-to-NH_3 Conversion Electrocatalyzed by Mo_2C Nanorod. *ACS Cent. Sci.* **2019**, *5* (1), 116–121. https://doi.org/10.1021/acscentsci.8b00734.

(14) Han, L.; Liu, X.; Chen, J.; Lin, R.; Liu, H.; Fang, L. U.; Bak, S.; Liang, Z.; Zhao, S.; Stavitski, E.; Luo, J.; Adzic, R. R.; Xin, H. L. Atomically Dispersed Molybdenum Catalysts for Efficient Ambient Nitrogen Fixation. *Angew. Chemie - Int. Ed.* **2019**, *58* (8), 2321–2325. https://doi.org/10.1002/anie.201811728

Curriculum Vitae

Xu Han

Johns Hopkins University
mailforxhan@gmail.com

EDUCATION

Johns Hopkins University Aug. 2015–present

Ph.D. Candidate in Chemistry, M.A. 2017

Fudan University Sep. 2011–June 2015

B.S. in Chemistry with Honors

PUBLICATION

- **Han, X.***; Gerke, C*; Banerjee, S; Zubair, M; Jiang, J; Bedford, N; Miller, E; Thoi, V. S. Strategic design of MoO_2 nanoparticles supported by carbon nanowires for enhanced electrocatalytic nitrogen reduction. *ACS Energy Lett.* **2020**, *5*, 3237-3243. (*co-first authors)
- **Han, X.**; Thoi, V. S. Non-Innocent Role of Porous Carbon Towards Enhancing C_{2-3} Products in Electroreduction of Carbon Dioxide. *ACS Appl. Mater. Interfaces* **2020**, *12*, 45929-45935.
- Baumann, A. E.; **Han, X.**; Butala, M. M.; Thoi, V. S. Thiophosphate Functionalized Zirconium MOFs for Li-S Batteries with Enhanced Rate Capabilities. *J. Am. Chem. Soc.* **2019**, *141* (44), 17891–17899.
- Banerjee, S.; **Han, X.**; Thoi, V. S. Modulating Electrode-Electrolyte Interface with Cationic Surfactants in Carbon Dioxide Reduction. *ACS Catal*. **2019**, *9* (6), 5631–5637.
- **Han, X.**; Wang, M.; Le, M. L.; Bedford, N. M.; Woehl, T. J.; Thoi, V. S. Effects of Substrate Porosity in Copper-loaded Carbon Aerogels for Selective Electrocatalytic Carbon Dioxide Reduction. *Electrochim. Acta* **2019**, *297*, 545–552.
- Hwang, J. Y.; El-Kady, M. F.; Li, M.; Lin, C.-W.; Kowal, M.; **Han, X.**; Kaner, R. B. Boosting the Capacitance and Voltage of Aqueous Supercapacitors via Redox Charge Contribution from Both the Electrode and Electrolyte. *Nano Today* **2017**, *15*, 15–25.
- Zhao, T.-T.; Wang, H.; **Han, X.**; Jiang, K.; Lin, H.; Xie, Z.; Cai, W.-B. A Comparative Investigation of Electrocatalysis at Pt Monolayers on Shape-controlled Au Nanocrystals: Facet Effect versus Strain Effect. *J. Mater. Chem. A* **2016**, *4* (41), 15845–15850.

SELECTED HONORS & AWARDS

- ACS Travel Award, 2020
- Ada Sinz Hill Fellowship, 2018
- Outstanding College Graduate of Shanghai, 2015
- Outstanding Senior Design of Shanghai, 2015
- Honor Student of Fudan University, 2015
- "Education Cup" Shanghai College Student Innovation Competition Award, 2014
- State-Level Best Team Leader for Social Development Project, 2013

TEACHING

Teaching Assistant, **Johns Hopkins University** Aug. 2015–May 2017

- Assisted teaching of 4 core classes with 100+ student, led weekly labs and office hours, organized discussion session, graded homework and exams. Received consistently excellent student rating
  - 030.302 Physical Chemistry II
  - 030.305 Physical Chemistry Instrumentation Laboratory
  - 030.204 Chemical Structure and Bonding w/ Lab
  - 030.101 Introductory Chemistry Lab

INTERNSHIPS

Biomedical Science Advisory Intern, **Milken Institute** Aug.–Nov. 2019

- Advised a client on $12 million philanthropic investment for facilitating R&D of a rare disease: NF1
- Managed 9 portfolio projects by providing scientific and financial advice to ensure successful operations
- Contributed to programming of a national conference with 1000+ attendees of business executives, etc.

Polymer Product Commercialization Intern, **Bayer MaterialScience**

Dec. 2014–Jan. 2015

- Worked on commercialization of patented polymers into cosmetic product ingredients by designing and performing experiments to elucidate the benefits of using target polymers in skin care and hair products
- Formulated strategy for a client to double the efficacy of facial masks through the addition of our materials

LEADERSHIP & VOLUNTEER

- Director of Education, JHU Graduate Consulting Club, 2019–present
- Board Member, JHU Chemistry Student Diversity Committee, 2017–2020

- Vice President, JHU International Student Ambassadors, 2017–2018
- Board Member, JHU Chemistry Student Safety Committee, 2016–2018
- STEM Mentor, STEM Achievement in Baltimore Elementary Schools, 2016–2017
- Founder & Team Leader, Traditional Chinese Culture Conservation Initiative, 2013–2014

SKILLS

Languages: fluent in English, native in Chinese
Instrumentation: GC-MS, LC-MS, HPLC, NMR, FTIR, Raman, UV-Vis, SEM, TEM, EDS, TGA, XRD, BET, XPS, Potentiostat
Techniques: chromatography, electroanalysis, chemical synthesis, single crystal X-ray diffraction
Computer: Microsoft Office, AutoCAD, MATLAB, Adobe Photoshop, C. Basic skills in R, Python

RESEARCH EXPERIENCE

Ph.D. Researcher, **Johns Hopkins University** Jan. 2016–present

- Electrochemical catalysis: set up electrocatalytic systems from scratch for CO_2 reduction and N_2 fixation, conducted catalytic performance test and high-accuracy gas/liquid product detections
- Material synthesis and fabrication: developed carbon coated metal system for highly efficient CO_2 reduction with enhanced C-C coupling product selectivity. Synthesized carbon nanowires supported metal compound for N_2 reduction, which keeps the record to date for selectivity of producing ammonia
- Leadership and management: initiated research direction as the first PhD student, mentored 3 graduate students and 3 undergraduates and helped them receive 2 competitive research awards and publish first author papers

Undergraduate Researcher, **Fudan University** Sep. 2013–June 2015

- Metal nanocrystal synthesis and monolayer deposition: synthesized shape-controlled metal nanocrystals (cubes, octahedra, dodecahedra) supported monolayer materials for catalyzing alcohol oxidation in fuel cell

Summer Research Scholar, **University of California, LA** Summer 2014

- Supercapacitor fabrication and test: fabricated high-performance supercapacitors with graphene-metal oxide hybrid electrode and graphene screen printed finger electrode with aqueous electrolyte